UNIVERSITA' DEGLI STUDI MILANO-BICOCCA
Dipartimento di Scienza dei Materiali

Structural and Morphological Tuning of Inorganic Luminescent Nanophosphors

Towards Applications in Sensing and Lighting

Ph. D. Materials Science 7th September 2015

PHYSICS AND CHEMISTRY OF ADVANCED MATERIALS
EUROPEAN DOCTORATE

Irene Villa
Matr. 760820

SUPERVISOR
Professor Anna Vedda

ABSTRACT

Luminescent materials have found a wide variety of applications as phosphors for fluorescent lighting, display devices, X-ray monitoring and imaging, scintillators, and in biomedical imaging. The research on nanostructured materials resulted in the development of novel synthetic methods to control their structure, morphology, and doping. When the size of crystalline powders is tailored down to the nanoscale, several advantages are achieved, like the reduction of the emitted light scattering when fabricating optical nanocomposites. Nanoscale dimensions are also necessary in biotech applications where the material is required to travel in blood vessels and penetrate into cells. Finally, the realization of high density optical ceramics by nanoparticles (NPs) compaction can be pursued, especially with materials that possess cubic crystalline structure, leading to the bottom-up fabrication of a new class of luminescent materials.

Hafnium oxide (HfO_2) has gained interest in the last years as an attractive nanophosphor because of its excellent physical and chemical properties. In this work, the luminescence and scintillation properties of pure and rare-earth (RE) doped HfO_2 NPs with a diameter < 5 nm have been investigated, obtained through a purposely designed synthetic strategy. This work was aimed at controlling the structural properties of NPs while optimizing their optical features.

A particular attention has been paid to the role of doping with europium and lutetium ions through the non-aqueous sol-gel method. Structure and morphology characterization by XRD, TEM/SEM, elemental analyses, and Raman/IR vibrational spectroscopies have confirmed the occurrence of the HfO_2 cubic polymorph for dopant concentrations larger than 5% mol for trivalent Lu^{3+} and Eu^{3+} ions. Optical properties have been investigated by radio- and photo-luminescence spectroscopy. Besides the relevance in application related issues, the results here reported represent an

important dataset for a better comprehension of the structure-property relationship in materials confined into nanoscale dimensions. We also demonstrated the possibility of tuning the emission spectrum by multiple RE doping, while deputing the NP cubic structural stabilization to optically inert Lu^{3+} ions.

Given the importance of HfO_2 as host material for RE, its intrinsic optical response is also worth of investigation. Undoped HfO_2 NPs were studied considering the effect of the size and of the crystal phase. A broad composite emission was observed in the visible range, potentially correlated both to intrinsic surface defects and to impurities. Its intensity can be varied by thermal treatments leading to surface modifications as well as to variations of particle dimensions. Its efficiency has been found to be comparable to that of standard commercial materials, evidencing the potential of pure HfO_2 NPs as efficient phosphors.

In parallel, we also investigated the use of emitting NPs for biological applications. Novel approaches for high contrast, deep tissue, in vivo fluorescence biomedical imaging are based on infrared-emitting NPs working in the so-called second biological window (1000 -1400 nm), where the partial transparency of tissues allows for the acquisition of high resolution, deep tissue images. In addition, the infrared excitation also leads to a reduction of auto-fluorescence generated by tissues, intra-body components, and specimen's diet. In my work, I exploited how the 1.3□m emission band of Nd^{3+} ions embedded in SrF_2 nanoparticles can be used to produce auto-fluorescence free, high contrast fluorescence images and bio-distribution studies. The strong brightness, the chemical and physical stability as well as high biocompatibility make Nd:SrF_2 nanocrystals very promising infrared nanoprobes for *in vivo* imaging experiments in the second biological window.

INDEX

Appendix A.

Appendix B.

Appendix C.

1. NANOSTRUCTURES AND NANOMATERIALS

Nanotechnology deals with small structures and small – size materials. Researches in this field aim to the investigation of both the fundamental properties and the technological challenges related to the size of the nanostructures. This chapter is a general introduction to the applications that inorganic nanomaterials and nanotechnologies offer, from electronics and optics to nanomedicine.

1.1 WHAT IS "NANOTECHNOLOGY"?

According to National Science Foundation, nanotechnology is the ability to *understand, control, and manipulate* matter at the level of individual atoms and molecules, as well as at the "supramolecular" level involving clusters of molecules (in the range of about 1 to 100 nm), in order to create materials, devices, and systems with fundamentally new properties and functions because of their small structure (W.A. Goddard III, 2007). Currently, there are many diverse definitions about what exactly nanotechnology is, but each one reflects the fact that it covers a broad spectrum of research fields and requires interdisciplinary efforts. The areas of nanoresearch involve engineering, physics, chemistry, materials science, and molecular biology.

Nowadays, nanotechnology is a complex interdisciplinary science including the chemical bottom-up approach in materials synthesis and fabrication, such as self-assembly or bio-mineralization to form hierarchical structures (nanochemistry, nanocolloid, sol-gel and quantum chemistry).

Nanophysics uses theoretical and experimental methods to determine the physical properties of materials at the nanoscale size range, including the structural, electronic, optical, and thermal behaviour of nanomaterials, electrical and thermal conductivity, the forces between nanoscale objects, and the transition between classical and quantum behaviour. Nanomaterials science is destined for research, development and production of novel nanostructured architectures, functional nanomaterials and smart nanocomponents with unique properties. Nanoelectronics, focused on electron beam lithography and imprint lithography; optoelectronics, and nanoengineering are destined to the development in computer science of novel technological processes, nanodevices, and micro-electromechanical-systems (MEMS). Lastly, nanotechnology is even applied in medicine and biology. Nanobionics aims to the development of novel biomachine complexes, such as diagnostic small devices or miniaturized surgical instruments, as well as biomaterials, implants and drug delivery with selective reactive molecular coatings, which can act in specific places inside the human body. Research in this direction has been triggered by the recent availability of revolutionary instruments and approaches that allow the investigation of material properties with a resolution close to the atomic level, as well as the characterization and manipulation artificial structures, whose features are controlled at the nanometer level (nanometrology) (A.G. Mamalis, 2007). Thus, combining knowledge from the fields of physics, chemistry, biology, medicine, informatics, and engineering, nanotechnology and nanoscience are rapidly evolving, showing a great potential to lead in great breakthroughs that can be applied in real life.

Although the exploitation and the understanding of atomic scale interactions in nanostructured materials is relatively recent, nanomaterials have

been produced and used by humans for hundreds of years. The synthesis of small clusters was utilized since antiquity in the art of making jewels, ornamental glassware, or stained glass in the Middle Ages. For instance, during the XVII century the ruby red colour of some ancient glass paintings was discovered by glassworkers to be obtained from gold and silver nanoparticles trapped in the glass matrix. Even the decorative glaze or metallic film known as “luster”, found on some medieval pottery, contains metallic spherical nanoparticles dispersed in a complex way in the glaze, which give rise to special optical properties. However, it was only in the nineteenth century that their optical properties started to become more systematically studied by Faraday who succeeded in producing gold colloids by reducing gold salts and showed that colour effects are correlated to their size and their morphology. In 1908, Mie showed that the original properties of metallic nanoparticles are a consequence of the limited volume of the material (“dielectric confinement”) of particles whose sizes are smaller or of the same order as the wavelength of the excitation field. At the same time, Maxwell-Garnett developed an effective field model in order to describe the optical properties of a medium containing “minute metal spheres.” Lately, the unique properties of materials in the size range up to a few hundreds of nanometers were recognized by Richard P. Feynman who, in 1959, gave a lecture at the California Institute of Technology describing the possibility of manipulating things atom by atom and using small machines down to the atomic level.

Norio Taniguchi of the Tokyo University of Science was the first to use the term "nanotechnology" in a 1974 conference to describe a thin film

deposition and ion beam milling exhibiting characteristic control on the order of a nanometer. His definition was:

”Nanotechnology' mainly consists of the processing of separation, consolidation, and deformation of materials by one atom or one molecule".

With inspiration from Richard Feynman, Eric Drexler in the 1980s conceptualized the possibility of manufacturing occurring atom by atom, and he warned that there were substantial risks as well as huge benefits potentially associated with these techniques. He even spoke about the power of an interdisciplinary approach to make commendable progress in nanoscience and nanotechnology, regarding technology in general, the field of chemistry, and in particular the computation, characterization, manipulation, and repair of biological materials.

Nanotechnology main step was the development, in the 1980’s, of the scanning tunneling microscopy and the atomic force microscopy. Through them, carbon nanotubes and fullerenes were developed in 1985. The discovery of fullerenes was at the origin of unceasing investigations on small clusters and nanoparticles and it contributed to the emergence of nanosciences, at the crossing point of several branches such as physics, chemistry, or even biology. Then came developments in synthesis and properties of semiconductor nanocrystals. Semiconductor nanoparticles, mostly sulphides and selenides Zn, Cd, Pb, etc. (H. Chander, 2005), have been synthesised long back as colloidal suspensions and studied for their electronic and optical properties since early 1980s. Besides pure semiconductor nanocrystalline phosphors, other nanoscale luminescent materials include transition metal ions or rare earth ions doped nanoscale oxides, chalcogenides, complex oxides and various inorganic

phosphors materials (He Hu, 2006). After these pioneering works and the development of powerful chemical synthesis routes at the end of the 1990s, a strongly increasing number of articles have been devoted to core/shell nanocrystals, where the colloidal semiconductor nanocrystals is composed of an inorganic core and is covered with a shell of a second semiconductor (P. Reiss, 2009).

The continuous revolution in nanotechnology results in the fabrication of nanomaterials with optimized and enhanced properties and functionalities with enormous potential in a wide range of applications. In addition to various industrial uses, great innovations are foreseen in information and communication technology, in biology and biotechnology, in medicine and medical technology, in metrology, etc. Significant applications of nanoscience and nanoengineering lie in the fields of pharmaceutics, cosmetics, processed food, chemical engineering, high-performance materials, electronics, precision mechanics, optics, energy production, and environmental sciences. For instance, in the energy generation challenge, innovative solar cell technologies that utilize nanostructured materials and composite systems such as organic photovoltaics offer great technological potential due to their attractive properties such as large scale and low cost roll to roll manufacturing processes. Nowadays, researchers expect to develop new commercial applications for nanotechnology. Huge aspirations are coupled to nanotechnological developments in modern medicine. The potential medical applications are predominantly in diagnostics (disease diagnosis and imaging) and advanced drug – delivering systems, including implantable devices that automatically administer drugs and sense drug levels; medical diagnostic tools, such as cancer – tagger mechanisms and “lab-on-a-chip” diagnostics.

For the above mentioned, nanotechnology demand is increasing every day. Therefore, many efforts are still needed in the development of the nanoscience, in order to create novel tiny materials through a better understanding and exploration of their optical, chemical, and mechanical properties.

1.2 NANOMATERIALS

1.2.1 HISTORY AND APPLICATIONS

Nanoworld is restricted by size of nanoparticles, 1 nm <d < 100nm. Actually, the dimensional limits 1 nm and 100 nm is indicative, whereas this definition must take into account the specificities of nanomaterials, for instance the variation of physico-chemical properties or the importance of specific surface area, in order to define precise dimensional bounds for the field "nano".

Nanocrystals are tiny crystals of metals, semiconductors, insulators, and magnetic material, whose properties and band structure can be described as the quantum mechanical coupling of over hundreds to thousands atoms. In 1982, A. Henglein (A. Henglein, 1982) reported the first absorption spectrum of a colloidal solution of size-quantized CdS nanocrystals, which was shifted considerably to higher energies with respect to the bulk band-gap of CdS. Nevertheless, the first correct interpretation of the observed blue shift of the absorption as a quantum mechanical effect is due to L. Brus (L. E. Brus, 1983). As the size of the material decreases to the nanometer scale, it will show a lot of new features that the bulk counterpart does not possess, such as the surface effect, quantum confinement effect, and macroscopic quantum tunnelling effect (A.D. Yoffe, 2002). Researches highlighted both the possibility to tune the

electronic structure, optical, and magnetic properties of the nanomaterials by varying the physical size of the crystal, and the occurrence of new phenomena, such as super-paramagnetism of magnetic nanocrystals, surface plasmon resonance in metals, and the size dependent band-gap of semiconductor nanoparticles (D.V Talapin, 2010). For example, in 1993 Murray, Norris and Bawendi (C. B. Murray, 1993) managed to synthetize the pyrolysis of organometallic reagents in order to create nanocrystals through a controlled growth route. Still, their work revealed how CdSe crystallites ranging in size from about 1.2 to 11.5 nm show different and remarkable qualities with respect to the bulk counterparts.

The research on nanomaterials is still active in developing new products with a wide applicability in several fields. Nanosized materials currently are used in numerous industries, e.g., carbon black particles make rubber tires wear resistant; nanofibres are used for insulation and reinforcement of composites; iron oxide creates the magnetic material used in disk drives and audio-video tapes; nano-zinc oxides and titania are used as sunblock for UV rays.

Nanoscale particles and nanolayers of materials are being used, among other things, to make products lighter, stronger or more conductive. Some of the products on the market using nanotechnology are computer hard drivers; bumpers on cars; solid – state compasses; protective and glare – reducing coatings for eyeglasses and windows; automobile catalytic converters; metal – cutting tools; dental bonding agents; longer – lasting tennis ball; burn and wound dressing; ink; etc.

Promising applications of nanotechnology in medicine and/or biology have attracted a lot of attention and have become a fast growing field. One of the attractive applications in nanomedicine is the creation of nanoscale devices

for improved therapy and diagnostics (M. Ferrari, 2005). Such nanoscale devices or nanorobots serve as vehicles for delivery of therapeutic agents, detectors or guardians against early disease and perhaps repair of metabolic or genetic defects. For applications in medicine, the major challenge is “miniaturization”: new instruments to analyse tissues down to the molecular level, sensors smaller than a cell allowing for looking at on-going functions, and small machines that literally circulate within a human body pursuing pathogens and neutralizing chemical toxins (D.A. LaVan, 2003).

Nowadays, many new and exciting metals, ceramics, polymers or composite nanomaterials have been discovered. The semiconductor quantum dots are used, for example, in biolabeling applications, as well as for light emitting devices with outstanding properties (I.L. Medintz, 2005 and Q. Sun, 2007). In chemiresistors, or so-called resistive gas-sensing elements, metal oxides nanoparticles are most commonly applied since they change their electrical resistance when oxidizing or reducing gases. For industrial application catalyst is required to feature high activity, stability in prolonged use at elevated temperatures, and mechanical physical and chemical stability in various conditions. Metal catalysts imply the use of metal oxide surface (TiO_2, Al_2O_3, ZrO_2 and CeO_2) or of activated carbon. Supporting noble metal catalyst on metal oxide surface has been reported to improve activity and stability of the catalysis. (K. Pirkanniemia, 2002). Cerium oxide (CeO_2) can be even used as a diesel fuel combustion catalyst, which reduces fuel consumption and carbon monoxide emissions. Titanium dioxide (TiO_2) nanoparticles have a large band-gap and are used for ultraviolet (UV) protection, photovoltaics, sensing, and self-cleaning functions (G. Oskam, 2006). Carbon -based nanomaterials (CBNs), including single or multiwalled nanotubes, fullerenes, nanodiamonds, and graphene,

possess excellent mechanical strength, electrical and thermal conductivity, and optical properties; much of the research efforts have been focused on utilizing these advantageous properties for various applications, such as high-strength composite materials and electronics. Moreover, CBNs have found their way into many areas of biomedical research, including drug delivery systems, tissue scaffold reinforcements, and cellular sensors, and have been widely regarded as highly attractive biomaterials due to their multifunctional nature employ (C. Cha, 2013). For instance, functionalized nanotubes have been proposed as synthetic trans-membrane pores. At the same time, the category of carbon-based nanomaterials has application for the manufacture of low cost solar cells, electronics, and anti-static composite materials, thanks to their electrical conductivity.

1.2.2 CLASSIFICATION OF NANOSTRUCTURES

Nanostructured materials as a subject of nanotechnology are low dimensional materials comprising of building units of submicron or nanoscale size at least in one direction and exhibiting size effects. The first classification scheme of nanomaterials was proposed by H. Gleiter in 1995 (H. Gleiter, 1995) and further extended to take into account 0D, 1D, 2D, and 3D structures such as fullerenes and nanotubes (V.V. Pokropivny, 2007).

According to the Gleiter's classification (Fig. 1.1), nanostructured materials can be divided into different classes according to their composition, morphology, and distribution of the nanocrystalline component. There are layer-shaped crystallites, rod-shaped crystallites and nanostructures composed of equiaxed nanometer-sized crystallites. Depending on the chemical composition of the crystallites, the three categories of nanomaterials may be

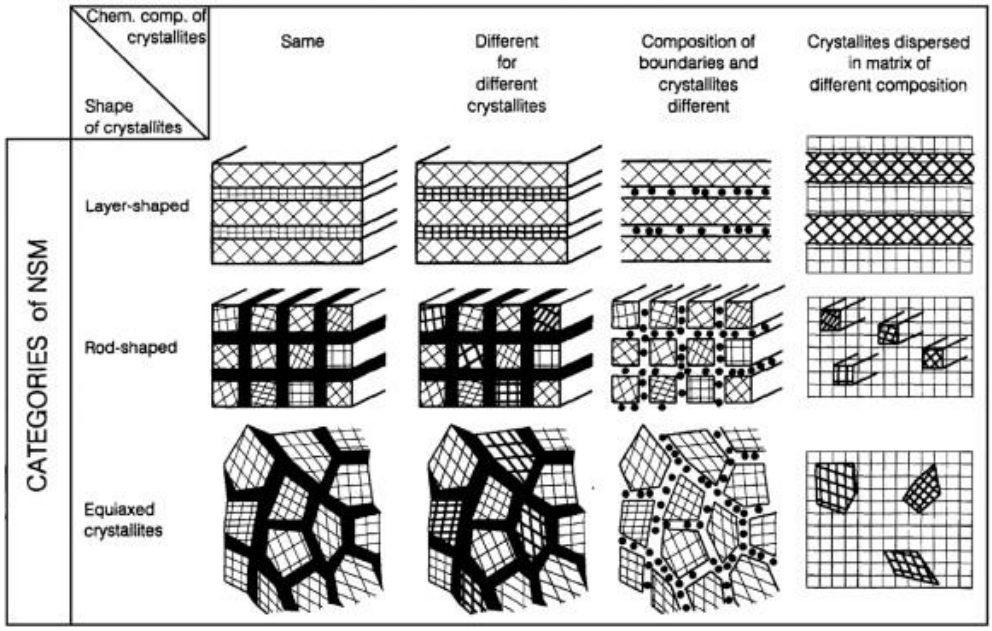

Figure 1.1 | Gleiter's classification scheme for nanomaterials according to their chemical composition and the dimensionality (shape) of the crystallites (structural elements) forming the nanostructures. (Printed from H. Gleiter, 1995)

grouped into four families. In the simplest case, all crystallites and interfacial regions have the same chemical composition. Examples of this family are semicrystalline polymers or nanomaterials made up of equiaxed nanometer-sized crystals, e.g., of Cu or CaF_2 crystals (belonging also to the third category).

Nanomaterials belonging to the second family consist of crystallites with different chemical compositions, as quantum well structures. If the compositional variation occurs primarily between the crystallites and the interfacial regions, the third family of nanomaterial is obtained. In this case, one type of atom segregates preferentially to the interfacial regions so that the structural modulation is coupled to the local chemical modulation. An interesting new example of such materials was recently produced by co-milling Al_2O_3 and Ga. (H. Gleiter, 2000) The fourth family of nanomaterials is formed by

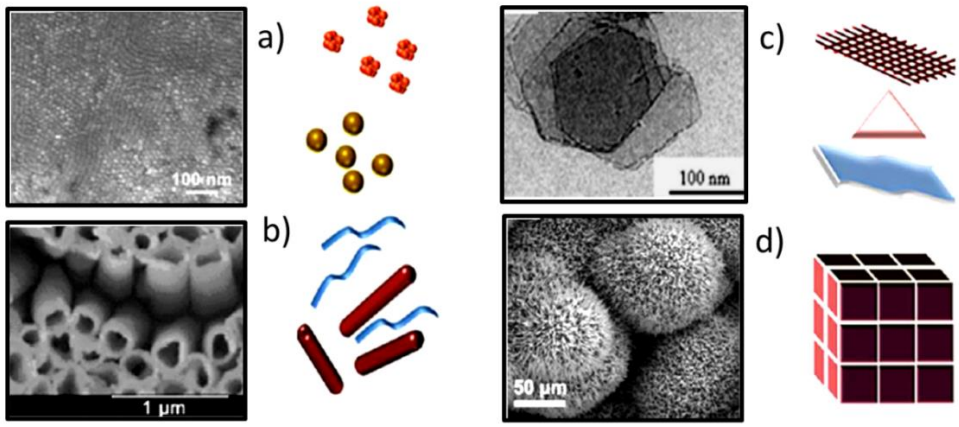

Figure 1.2 | Classification of nanomaterials (a) 0D spheres and clusters, (b) 1D nanofibres, wires, and rods, (c) 2D films, plates, and networks, (d) 3D nanomaterials. Typical SEM images of a CdSe quantum-dot array grown on a graphene sheet by using a mesoporous silica film template (a), MnO_2 nanotubes (c) and aluminum nitride nanoflowers (d); TEM images of palladium nanosheets (b) is reported. (Printed from N. Tiwari, 2012)

nanometer-sized crystallites layers, rods, equiaxed crystallites dispersed in a matrix of different chemical composition.

One of the basic results of the materials science is the insight that most properties of solids depend on the microstructure, i.e. the chemical composition, the arrangement of the atoms (the atomic structure) and the size of a solid in one, two or three dimensions. A reduction in the spatial dimension, or confinement of particles or quasi-particles in a particular crystallographic direction within a structure generally leads to changes in physical properties of the system in that direction. Hence the other main classification of nanostructured materials and systems essentially depends on modulation dimensionalities: 0D—nanoclusters; 1D—multilayers; 2D—nanograined layers; 3D—equiaxed bulk solids (Fig. 1.2).

A rich variety of physical and chemical methods have been developed for fabricating 0D nanostructures with well-controlled dimensions. Quantum dots

(QDs) are the most important example of 0D nanomaterials. Beyond the recent development in synthetizing quantum dots, even in a core/shell structures, they have been extensively studied in light emitting diodes (LEDs), solar cells, and single-electron transistors. In the last decade, 1D nanomaterials (nanowires, nanorods, nanotubes, nanobelts, and nanoribbons) have stimulated an increasing interest due to their wide range of potential applications in nanoelectronics, nanodevices and systems, nanocomposite materials, and alternative energy resources. The 2D nanostructures, such as nanoprisms, nanoplates, nanosheets, nanowalls, and nanodisks, have become a focal topic in materials research, owing to their many low dimensional characteristics different from the bulk properties. They exhibit unique shape-dependent characteristics and subsequent they are used as building blocks for the key components of nanodevices, but also for the investigation and the development of novel applications in sensors, photocatalysts, nanocontainers, nanoreactors, and templates for 2D structures of other materials. Lastly, owing to the large specific surface area and other superior properties over their bulk counterparts arising from quantum size effect, 3D nanostructures have attracted considerable research interest, in order to synthesize materials with a controlled structure and morphology. In addition, nanoballs (dendritic structures), nanocoils, nanocones, nanopillers and nanoflowers are important materials due to its wide range of applications in the area of catalysis, energy storage (J. N. Tiwari, 2012*).*

1.2.3 INORGANIC NANOSTRUCTURES

Inorganic nanostructures have gained importance because of their outstanding luminescence properties and their potential applications as new

building block materials for the next generation electronics. The information technology revolution in the previous decades has been firmly based on the development and application of inorganic nanomaterials. Silicon forms the basis of the vast majority of electronic devices, whilst semiconductor compounds, such as gallium arsenide (GaAs), are used for many optoelectronic applications. The formation of a nanostructure, in which the dimensions along one or more directions are reduced below 10 nm, dramatically modifies the carriers properties, which become governed by the laws of quantum mechanics. For instance, inorganic semiconductors offer superior carrier mobilities, strong light absorption, photo and thermal stabilities, and therefore they are mostly used in electronics and optoelectronics. However, they are still difficult to be synthesised by means of low cost processes, as the crystallization of inorganic semiconductors requires high temperature treatments, which leads to the increase of the fabrication costs for new devices, and compatibility with flexible plastic substrates (D.V Talapin, 2010). Nevertheless, the progresses in nanocrystals synthesis during the past decade have been permitting to generate nanostructured materials with a great deal of control over size, shape, and composition, as well as physical properties (G. Garnweitner, 2008).

Luminescent and non-luminescent nanomaterials are also used today in a variety of lighting applications. Non-luminescent nanomaterials, such as nano-silica and nano-alumina, may be used to form a thin conformal coating around phosphor particles that prevents the oxidation induced degradation of the emitting unit, for instance a rare earth ion, and improves the efficiency and maintenance of fluorescent lamps. (M. Zachau, 2004). Luminescent nanoparticles show a large potential for solid state lighting with LEDs. Generally, there are three different approaches which can be used for generating white

light based on LEDs: (1) by mixing reds, greens, and blues LEDs (RGB LEDs), (2) by using an ultraviolet (UV) LED to stimulate RGB phosphors, and (3) by using a blue-emitting diode that excites a yellow-emitting phosphor; the combination of blue and yellow light makes a white-emitting LED. Today' s commercial white LEDs normally use a 450‑470 nm blue GaN LED chip covered by a yellowish phosphor coating, which is usually made of $Y_3Al_5O_{12}$:Ce (YAG:Ce). However, this phosphor suffers some weaknesses, such as poor colour rendering index and low stability of colour temperature. Alternatively, due to their size tunable emission wavelength, semiconducting nanophosphors, such as CdSe or CdS, are already available and applied in lighting (C. B. Murray, 1995). There are, however, severe challenges to overcome, like the Cd based chemical hazardous. Even if a shell is applied enclosing the Cd based nanoparticle, there are still remaining problems to handle Cd compounds. Semiconducting nanophosphors based on alternative to Cd materials have been synthesized; e.g. InP and ZnS or ZnS:Mn (D.V Talapin, 2010). They are, however, either not excitable by wavelengths longer than 370 nm, not stable or not efficient enough. Lastly, insulating materials activated by rare earths ions, for example $LaPO_4$ and YVO_4 activated by europium and other rare earth ions, have been synthesized (S .Ye, 2010). Their efficiencies are high and, at the same time, they are stable and therefore they have been proposed in several applications as medical tracers.

1.3 NANOMEDICINE

Nanoparticles have recently emerged as an important group of materials used in numerous disciplines within life sciences, ranging from basic biophysical

research to clinical therapeutics. For example, luminescent nanoparticles are excellent optical bioprobes and they have significantly extended the capabilities of other fluorophores, such as organic dyes and genetically engineered fluorescent proteins. Their advantages include excellent photostability, size tunable spectra, controllable size, resistance to environmental conditions, such as pH and temperature (L. Wang, 2005). Some types of nanoparticles provide enhanced detection contrast due to their long emission lifetime and/or luminescence wavelength blue-shift (anti-Stokes) by photon upconversion. By using fluorescent labels it is possible to visualize cellular components, such as organelles and specific molecules, and observe protein–protein interactions. Such challenging bioimaging and biosensing experiments place high demand on fluorophore performance, which may be compromised by undesirable photophysical properties of conventional organic fluorophores. For instance, photostability is critical in many applications, including stimulated emission depletion microscopy (STED), and most inorganic nanoparticles exhibit stable continuous emission (D. T. Burnette, 2011). Beyond the improved stability and signal to noise radio, many luminescent inorganic nanomaterials have been shown to be non-toxic or have limited cytotoxicity (J. Vuojola, 2014). This is the case of some several upconverting systems, including $NaYF_4$:Yb, codoped with Er^{3+} or Tm^{3+} ions. This makes the luminescent nanoparticles well suited for biological applications, especially in the case of in vivo scenarios. (V K A Sreenivasan, 2013)

About non-luminescent nanomaterials, the most promising application is their use for targeted, site-specific drug delivery. The potential of eliminating a tumorous outgrowth without any collateral damage through nanomaterial-based drug delivery has created significant interest for bio-nanomaterials (L.

Wang, 2008). Modifying or functionalizing nanoparticles to deliver drugs through the blood brain barrier for targeting brain tumours can be regarded as the most brilliant outcome of the *in vivo* drugs delivery technology (G. V. Nazarov, 2009). On the other side, nano-sized colloidal carriers of drugs can be regarded as an important advance in the development of modern pharmacotherapy. They act as potential carriers for several classes of drugs, like anti-cancer, anti-hypertensive and hormones, etc. (I. Bala, 2004). Here, submicron colloidal particles have been used as nanocarriers for the purpose of drug delivery and also used for the diagnosis of diseases, thus significantly broadening the scope of pharmacokinetics for insoluble drugs. Although many problems related to selective binding, targeted delivery and toxicity need to be overcome, designed nanoparticles to tackle problems related to diagnosis, target and route of administration may lead to a new more successful paradigm in the world of theranostics and research.

1.4 LUMINESCENCE IN NANOSTRUCTURES

1.4.1 NANOSIZE AND PROPERTIES

The reason of the great interest for luminescent nanomaterials lies in their specific size dependent and tunable properties that may be significantly different from the physical properties of their solid state bulk counterparts, as listed below:

(1) Nanomaterials may have a significantly lower melting point or phase transition temperature and appreciably reduced lattice constants.

(2) The enhancement in mechanical strength due to the reduced probability of defects.

(3) The optical absorption peak of a nanoparticle may shifts to shorter wavelengths, due to the band-gap increasing. This interesting feature is mostly observed in semiconductors.

(4) Electrical conductivity decreases with a reduced dimension due to increased surface scattering.

(5) Magnetic properties of nanostructured materials change from the ferromagnetism of bulk materials to super-paramagnetism.

These variations in nanocrystals properties can be ascribed to many factors, for example (i) large fraction of surface atoms, (ii) large surface energy, and (iii) spatial confinement. In the following we introduce briefly how the physical properties typical of nanostructures can affect their luminescence.

1.4.2 STRUCTURAL PROPERTIES

The stability of a crystal and the equilibrium lattice parameters are controlled by a local balance between short-range repulsive forces and long-range Coulomb forces. By decreasing the particle size, changes in the cell parameters and lattice symmetry occur. (P. Ayyub, 1995)

The change in interfacial volume and structure of the crystal while decreasing its dimension are small but often lead to important modifications in many physical properties, such as mechanical properties, diffusion or ionic conductivity, and thermos- dynamical features. For instance, the melting point

of small dimensional materials is lower than in the bulk counterparts due to pressure-induced stronger surface strengths in the nanostructures. Moreover, when the size is decreased, surface strengths induce an additional pressure. It leads to disorder and then to crystal field fluctuations. Small changes in the cell parameters can also be observed (C. Dujardin, 2010). This can affect significantly the luminescence concentration quenching mechanism. After the excitation of a doped nanomaterial, energy migration occurs by the resonance between the energy levels of the donor and the acceptors and depends on both their concentrations and their relative distance. In a bulk material the energy can propagate over large distances until it is quenched by the presence of non-radiative defects. In nanocrystals, the energy transfer probability is lower than in the bulk because of crystal field fluctuations given by the pressure. This induces a mismatch among the energy levels of the involved optically active centers, thus reducing the concentration quenching effectiveness by decreasing the energy diffusivity (Fig. 1.3).

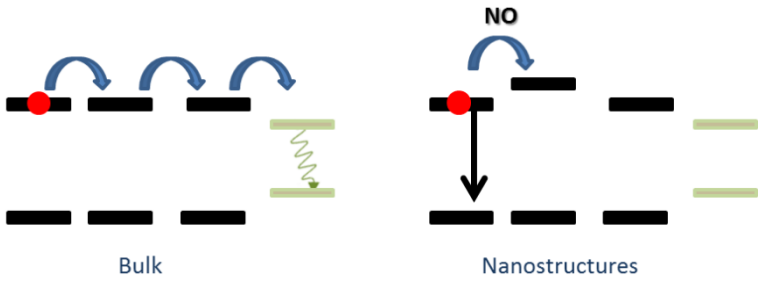

Figure 1.3 | Effect of the crystal field fluctuation on the concentration quenching. In bulk and nanostructures. (Printed from C. Dujardin, 2010)

1.4.3 SURFACE PROPERTIES

The relative number of atoms at the surfaces and interfaces increases with decreasing the size, making surface effects very important in small solids. In any material, surface atoms make a distinct contribution to the free energy, and the large changes in thermodynamic properties of nanocrystals can ultimately be ascribed to their large surface/volume ratio.

A nanomaterial is indeed a highly defective system. At the surface, substantial reconstructions in the atomic positions occur generating energy levels that lie within the forbidden gap of the crystal. These levels may be luminescent centers that induce emission bands that do not exist in the bulk crystal. At the same time, the atoms on the surface of a nanocrystal facet are incompletely bonded within the crystal lattice, thus disrupting the crystalline periodicity and leaving one or more “dangling orbital” on each atom pointed outward from the crystal. Their presence induces inhomogeneous broadening in the luminescence band spectrum - like that in glasses - and form surface energy states within the material band-gap which can trap charge carriers at the surface, increasing the probability of non-radiative decay events. Sometimes, the passivation of the surface is required. i. e. by bonding surface atoms to another material with larger band-gap by following the general strategy of producing core/shell systems.

1.4.4 SPATIAL CONFINEMENT

The electronic energy spectrum in small particles is quantized into discrete levels, and the energy separation between adjacent levels increases with decreasing the material dimensions (Fig. 1.4).

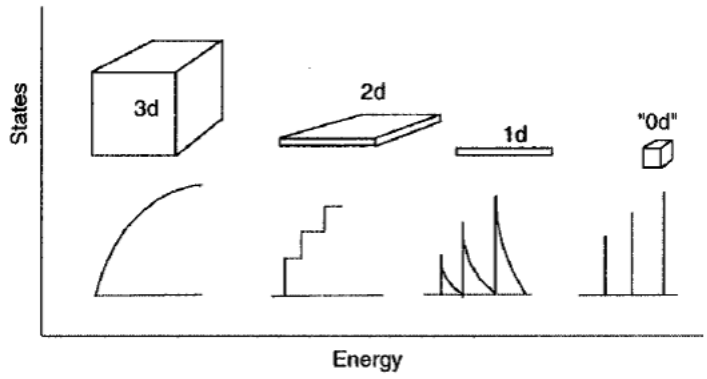

Figure 1.4 | Density of states for a band of a materials structure of 3, 2 ,1 and 0 dimensions. In 0d case, the energy levels are discrete (Printed from P. Alivisatos, 2006).

Quantum size effects appear when the particles are small enough to be comparable to the Bohr exciton diameter (a_B), which can vary from 1 nm to more than 100 nm depending on the material. If the size of a material nanocrystal is smaller than the size of the exciton, the charge carriers become spatially confined, which raises their energy (P. Alivisatos, 2006). Therefore, the exciton size delineates the transition between the regime of bulk crystal properties and the quantum confinement regime, in which the optical and electronic properties are dependent on the nanocrystal size. The wavelengths of fluorescence and absorption can be tuned through quantum confinement to emit fluorescent light throughout the visible spectrum (A. M. Smith, 2010). For semiconductors, a_B usually varies from 2 to 50 nm, therefore the quantum confinement effect appears in the nanometric dimensional range. To the contrary, for insulators the typical a_B is in the order of 1 nm. Therefore, insulators show quantum confinement by QC only for sizes already in the cluster regime (<20 atoms) (C. de Mello Donegà, 2010).

1.5 Optical properties of lanthanide (Ln) in doped nanomaterials

The physicochemical properties of the material at the nanoscale may differ markedly from those in the bulk, affecting also the luminescence properties and excited-state dynamics in inorganic host nanocrystals doped by emitting lanthanide ions. In particular, the electronic structures of Ln^{3+} ions are critically dependent on the local symmetry around them (K. Binnemans, 1996). A small difference in local structure will lead to significant change in the electronic energy levels as well as excited-state dynamics of the dopant ions. On the other side, introducing a dopant ion in a nanostructure may induce disordering and surface defects in an already size reduced distorted material. Consequently, Ln^{3+} ions experience different crystal-field surroundings in the same matrix (W. Luo, 2008). PL and luminescence decay coming from ions hosted in sites of different symmetry are expected to be distinct. Site selective PL spectroscopy and time resolved PL, confirm that the presence of multiple luminescence centers of Ln^{3+} in nanomaterials induces a variation of the decay curves of dopant ion emission for each available site. The typical surface defect states or quenching centers of nanostructures acts as effective non-radiative relaxation channels, with evident consequences on the non-radiative decay rates of the Ln^{3+}, which typically show a decrease in the PL lifetime in comparison with the case of bulk crystal.

However, the luminescence of Ln^{3+} ions embedded in wide band-gap nanomaterials can be also enhanced. For example, the increase of luminescence yield in Ln^{3+} doped nanoparticles can be achieved through inner adjustments of the local structure and local symmetry. The forbidden f–f transitions of lanthanide ions in a symmetric environment generally become allowed as the

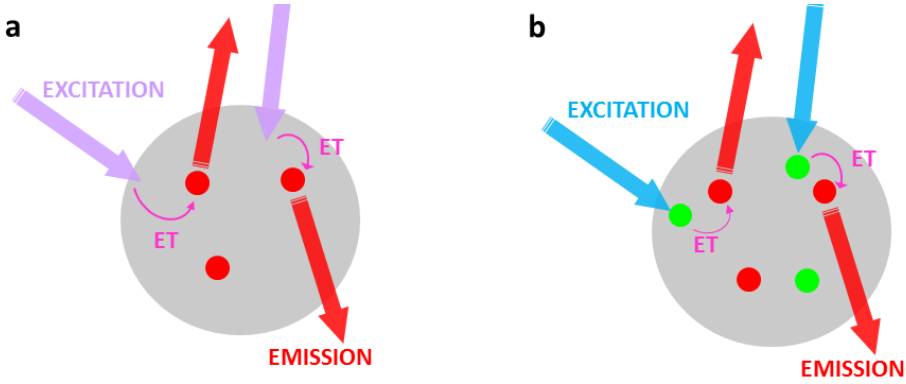

Figure 1.5 | Sensitized emission of Ln ions in nanoparticles. (a) Sensitization of the Ln ion emission (red dots) by energy transfer from the host. (b) Sensitization of Ln ion emission by co-doping with a proper light harvester (green dot).

local symmetry is reduced. Therefore, symmetry reduction in the local field and interaction that induces an asymmetric environment may be an effective and direct way to improve fluorescence in Ln^{3+} by increasing the radiative recombination probability of the involved electronic excited states.

Another efficient way to enhance the luminescence of Ln^{3+} ions is based on its sensitization by the exciton recombination in the host. The direct excitation of the parity forbidden 4f–4f transitions of Ln^{3+} is generally inefficient compared to the host absorption in ultraviolet (UV) region. Therefore, a host with property tuned band-gap can be efficiently exploited as light harvester antennae, which, upon absorption, transfers the excitation energy to the emitting ions incorporated. Alternatively, the luminescence sensitization can be achieved by a dual doping of the nanoparticle. The first dopant acts as light harvester and donor of the absorbed energy. The second moiety is then excited by energy transfer from the first one, and works as final emitting recombination center. (Y. Liu, 2011)

1.6 REFERENCES

Alivisatos P. (2004), *The use of nanocrystals in biological detection.* Nature Biotechnology, 22, 47 52.

Ayyub P. et al. (1995), *Effect of crystal size reduction on lattice symmetry and cooperative properties.* Physical Review B, 51, 9.

Bala, I., et al. (2004), *PLGA nanoparticles in drug delivery: the state of the art*. Crit. Rev. Ther. Drug Carrier Syst., 21, pp. 387–422.

Binnemans K. and Görller-Walrand C. (1996*), Application of the Eu^{3+} ion for site symmetry determination*. Journal of Rare Earths, 14, 3.

Brus L.E. (1983), *A simple model for the ionization potential, electron affinity, and aqueous redox potentials of small semiconductor crystallites*. J. Chem. Phys. 79, 5566.

Burnette D. T. et al. (2011), *Bleaching/blinking assisted localization microscopy for super resolution imaging using standard fluorescent* molecules PNAS, 108, 52, pp. 21081–21086

Cha C. et al. (2013), *Carbon-Based Nanomaterials: Multifunctional Materials for Biomedical Engineering*. ACS Nano, 7, 4, pp. 2891–2897.

Chander H. (2005), *Development of nanophosphors—A review,* Materials Science and Engineering: R: Reports, 49, 5, pp. 113–155.

de Mello Donegà C. (2010) *Synthesis and properties of colloidal heteronanocrystals*, Chem. Soc. Rev. 40, 1512–1546.

Dujardin C. et al (2010), *Luminescence and scintillation properties at the nanoscale*, IEEE TRANSACTIONS ON NUCLEAR SCIENCE, 57, 3.

Ferrari M. (2005), *Cancer nanotechnology: opportunities and challenges*. Nat Rev Cancer, 5, pp.161–171.

Garnweitner G. and Niederberger M. (2008), *Organic chemistry in inorganic nanomaterials synthesis.* J. Mater. Chem.,18, pp. 1171-1182.

Gleiter H. (1995) *Nanostructured materials. State of the art and perspective*. Nanostructured Materials, 6, pp. 3-14.

Gleiter H. (2000) *Nanostructures materials: basic concepts and microstructure.* Acta mater., 48, pp. 1-29.

Goddard, III W. A. et al. (2007), *Handbook of nanoscience, engineering, and technology* 2nd edition by Taylor & Francis Group, LLC.

Henglein A. (1982), *Photodegradation and fluorescence of colloidal cadmium sulfide in aqueous solution.* Ber Bunsen-Ges Phys Chem 86, pp. 301–305.

Hu H. and Zhang W (2006), *Synthesis and properties of transition metals and rare-earth metals doped ZnS nanoparticles.* Optical Materials, 28, 5, pp. 536–550.

LaVan DA et al.(2003), *Small scale systems for in vivo drug delivery*. Nat Biotechnol., 21, pp. 1184–1191

Liu Y. et al. (2011), *Optical spectroscopy of lanthanides doped in wide band-gap material nanocrystals*. Journal of Luminescence, 131, 3, pp 415–422.

Luo W. et al. (2008), *Evidence of trivalent europium incorporated in anatase TiO_2 nanocrystals with multiple sites*. J. Phys. Chem. C, 112,28, pp 10370–10377.

Mamalis A.G. (2007), *Recent advanced in nanotechnology.* Material processing technology, 181,1–3, pp. 52–58.

Medintz I.L. (2005), *Quantum dot bioconjugates for imaging, labelling and sensing nature materials*. Nature Materials, 4, pp. 435 - 446)

Murray C. B. et al. (1993), *Synthesis and characterization of nearly monodisperse CdE (E = sulfur, selenium, tellurium) semiconductor nanocrystallites.* J. Am. Chem. Soc., 1993, 115, 19, pp 8706–8715.

Murray C. B. et al. (1995), *Self-Organization of CdSe nanocrystallites into three-dimensional quantum dot superlattices.* Science, 270, 1335.

Nazarov, G.V. et al. (2009), *Nanosized forms of drugs (a review).* Pharm. Chem. J. 43, 163–170.

Oskam G. (2006), *Metal oxide nanoparticles: synthesis, characterization and Application* J Sol-G.el Sci Techn 37, pp. 161–164.

Pirkanniemia K. and Sillanpääb M. (2002), *Heterogeneous water phase catalysis as an environmental application: a review.* Chemosphere, 48, 10, pp. 1047–1060

Pokropivny V.V. and Skorokhod V. V. (2007), *Classification of nanostructures by dimensionality and concept of surface forms engineering in nanomaterial science.* Materials Science and Engineering: C, 27, 5–8, pp. 990–993.

Reiss P. (2009), *Core/Shell Semiconductor Nanocrystals***.** Small, 5, 2, pp. 154–168.

Smith A. M. and Nie S (2010), *Material nanocrystals: structure, properties, and band gap engineering.* Acc Chem Res. 43, 2.

Sreenivasan V. K. A. et al. (2013), *Luminescent nanoparticles and their applications in the life sciences.* J. Phys.: Condens. Matter., 25, 194101.

Sun Q. (2007), *Bright, multicoloured light-emitting diodes based on quantum dots*. Nature photonics, 1, pp. 717-722.

Talapin D.V. et al. (2010). *Prospects of colloidal nanocrystals for electronic and optoelectronic applications*. Chem Rev.,110, 1, pp. 389-458.

Tiwari J. N. et al. (2012*). Zero-dimensional, one-dimensional, two-dimensional and three-dimensional nanostructured materials for advanced electrochemical energy devices*. Progress in Materials Science, 57, pp. 724–803.

Vuojola J. and Soukka T. (2014), *Luminescent lanthanide reporters: new concepts for use in bioanalytical applications*. Methods Appl. Fluoresc., 2, 012001 .

Ye S. et al. (2010), *Phosphors in phosphor-converted white light-emitting diodes: Recent advances in materials, techniques and properties*. Materials Science and Engineering: R: Reports, 71, 1, pp.1–34.

Yoffe, A.D. (2002), *Low-dimensional systems: Quantum size effects and electronic properties of semiconductor microcrystallites (zero-dimensional systems) and some quasi-two-dimensional systems*. Adv. Phys., 42, 173–266).

Wang L. et al. (2005), *Fluorescence resonant energy transfer biosensor based on upconversion-luminescent nanoparticles.* Angew. Chem. Int. Ed., 44, 6054 –6057.

Wang L. et al. (2008), *Bioconjugated silica nanoparticles: development and applications.* Nano Res., 1, 99–115.

Zachau M. and Konrad A. (2004), *Nanomaterials for Lighting.* Solid State Phenomena, 99-100, pp 13-18.

2. WIDE BAND-GAP NANOEMITTERS: THE CASE OF HfO_2

In this chapter we introduce the properties of wide band-gap materials and present the hafnium dioxide (HfO_2 or hafnia) as a study case for its potential application in technology as optically active nanocrystal.

2.1 INTRODUCTION

A characteristic trend in modern solid-state physics is the increased interest expressed in the properties of objects in the nanometer scale. Spatial confinement markedly affects the structure of electronic states and the vibrational (phonon) properties of crystals. Among them, wide band-gap nanomaterials - insulators and semiconductors - have emerged as one of the most important class of new materials over the last decade. Most publications have been focused with investigation of the effect of confinement on the electronic bands and excitons in semiconductors (quantum wells, wires, and dots), as well as in the properties of dielectric nanostructures, which are mostly influenced by phenomena like the phonon spectrum modification and the increasing role of the surface (S. P. Feofilov, 2002).

The research efforts in the optical properties of wide band-gap nanocrystals are stimulated to a considerable extent by the application potential of these materials in optoelectronics, renewable energy technologies,

sensing and bio-diagnostics. For instance, nanostructures, such as III - nitrides, SiC, ZnO, TiO_2, and other transition metal oxides, have attracted intensive research attention owing to prospective applications in solid-state lighting, solar cells, power electronics, sensors (G. Shen, 2009), or in medical applications and environmental science (L. Wang Zhong, 2008). Also, possessing a strong tolerance to high temperatures, mechanical robustness, and a good environmental stability, these wide band-gap nanomaterials have been employed in every technological field where an enhancement or an optimization of energy conversion efficiency, optical properties, or radiation strength were required. (S. J. Pearton, 2013)

The more recent researches on wide band-gap nanostructures have been addressed on the achievement of progress in their synthesis, in order to get some advances on the crystallinity and electronic structure manipulation, as well as on impurities and doping level to fully tune their optoelectronic features. Actually, from the standpoint of optical properties, wide band-gap nanocrystals doped by rare earth (RE) and transition metal (TM) ions have gained a particular interest. Impurity ions can serve as spectroscopic probes to investigate the dynamic processes occurring in nanocrystals and the effects which are directly associated with the smallness of the nanocrystal size. At the same time a better comprehension on the phenomena involved in their chemical and physical properties must be pursued, with the aim of improving the nanomaterials based devices performances and their potential applications.

In the following, we will introduce the case of hafnium dioxide (HfO_2, or hafnia), which is currently studied in the form of both undoped and doped

nanocrystals to explore the room of applicability of these nanoemitters as scintillators and for lighting and displays applications.

2.2 WHAT IT IS HfO_2?

Metal oxides play a very important role in many areas of chemistry, physics, and materials science (M. Niederberger, 2005). These materials can adopt different structural geometries showing an electronic structure that can exhibit metallic, semiconductor, or insulator characters. In technological applications, oxides are used for example in the fabrication of microelectronic circuits, sensors, piezoelectric devices, fuel cells, and coatings for the passivation of surfaces against corrosion and as catalysts (L. Gao, 2012). The most active areas of the semiconductor industry involve the use of oxides and pursue the development of the synthetic strategy of advanced oxide nanostructures by different physical and chemical preparation methods, which produce solid powders with a controlled particle size (T. Taniguchi, 2008).

In this field, a significant attention is paid to IV-B metal oxides, especially hafnium, zirconium and titanium dioxide (HfO_2, ZrO_2 and TiO_2). Due to their electrical properties, different existing crystal polymorphs, their higher dielectric constant and wide band-gap, they show a wide range of industrial applications such as high temperature fuel cell electrolytes, oxygen sensors, and waveguides (X. Zhao, 2002). Among all IV-B oxides ,and other transition metal oxides, hafnia, is considered the most promising and technologically important, due to its large band-gap (5.5‑6.0 eV), relatively high dielectric constant (k = 25), high thermal and chemical stability, and significantly high melting point (over 2700 °C). In nature, hafnia exists as three polymorphs at atmospheric pressure.

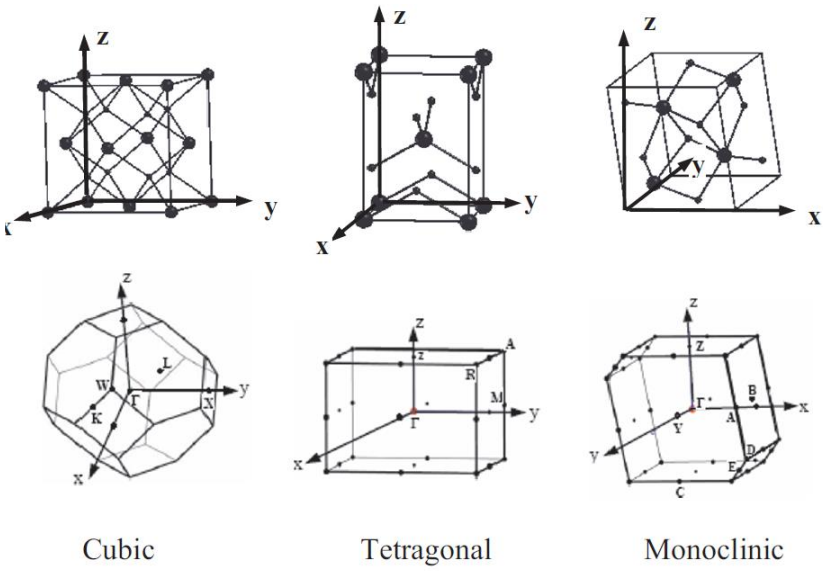

Figure 2.1 |(Upper panel) Structures of the three HfO_2 phases. Large and small black dots denote Hf and O atoms respectively. (Lower panel) Brillouin zones of the same phases (printed from T. V. Peralov 2006).

At low temperature, the monoclinic baddeleyite phase is stable (*m*, space group $P2_1/c$) and it transform to a tetragonal structure (*t*, space group $P4_2/nmc$) at around 2000 K. For higher temperature, it converts into the cubic fluorite structure (*c*, space group F*m*3*m*), as illustrated in Fig. 2.1 (R. Terki, 2008).

According to the multiplicity of its qualities, hafnia is a very interesting material for the physical and material science community. It can be employed in optical protective and thermal barrier coatings, as well as for high temperature refractory applications (B. Matović, 2012).Thanks to its mechanical resistance, hafnia finds applications as ceramic, super-hard materials and catalysts, or as component in gas sensors and fuel cell electrolytes (C.H. Lu, 2008). Significant attention has been paid to HfO_2 as potential alternative gate

dielectric to replace SiO_2 (J. H. Choi, 2001). The replacement of silicon with a new oxide is a challenge. A gate oxide has to fulfil a number of requirements such as the high dielectric constant and low defect concentrations, in order to fabricate ultra-small thickness layers with a controlled defects concentration, thus leading to the reduction of the quantum mechanical tunnelling through the dielectric and the leakage current. Although HfO_2 still suffers from a much higher defect density than SiO_2 and a more detailed studies must to be addressed in the matrix defects investigation, it resulted to be suitable for application as new generation high-k gate dielectric in microelectronics, i. e. metal oxide based semiconductors field effect transistors (MOSFET) and for the future generation of nanoelectronics devices (R Clark, 2014). Therefore, over the last decades, Hf-based high performance materials and devices have been designed

Beside electronics, the hafnium dioxide is currently considered also an attractive host as heavy scintillator with high stopping power for gamma- and X-rays, because it possesses a high density of 9.7 g/cm^3combined with the high atomic number of Hf (Z= 72). A broad bluish emission band proper of the undoped HfO_2 lattice in form of thin film has been recently observed. These features make hafnia a candidate for a number of scientific and industrial applications based on X-ray imaging techniques, even with high spatial resolution (M. Kirm, 2005). Moreover, because of its transparency in the visible spectral range, hafnia is often used as host for RE luminescent ions. Various studies on the luminescence properties of RE doped hafnia have revealed the possibility to tune the emission colour of the material by mixing the intrinsic broad emission with the one of the optical active doping ions (A. Wiatrowska, 2010). Although many efforts must be placed in the understanding of the

luminescence in both undoped and doped hafnium oxides nanoparticles, the last works of investigation have proven that hafnia nanocrystals satisfy the requirement to be used as high yield scintillators, as well as for white phosphors applications (C. LeLuye, 2008). Furthermore, progresses have been done controlling the dimensions and the structural features of nanocrystals, in order to obtain wide band-gap transparent hafnium oxide based-ceramics and nanocomposites (J. Wang, 1992 and S. Araki, 2004).

2.3 STRUCTURAL, MORPHOLOGICAL AND LUMINESCENCE PROPERTIES CONTROL IN HAFNIA NPS BY RE DOPING

An extensive and theoretical study of the optical response of nanoparticles has been performed in order to propose them both for scintillators and for high emitting photoluminescence materials. This is even the case of monoclinic HfO_2. During the last years, high quality wide band-gap nanocrystals, such as hafnia, became unique host materials for doping of optically active impurities. The increasing interest in impurity doped nanocrystals and their optical properties is stimulated to a considerable extent by application potential of these materials, as in laser technology, display applications, and nanoparticles composite films for the development of highly efficient solar cells (Y. Kanemitsu, 2006). Hafnium oxide synthesis procedures are mostly focused on doping nanocrystals with a diameter below 5 nm with several RE ions (B. L. Cushing, 2004). This aim may be achieved through a novel synthesis route, the nonaqueous sol-gel method (N. Pinna, 2004), by which the incorporation of doping elements in HfO_2 nanoparticles can be easily obtained with an appropriate choice of ions precursors.

2.3.1 OPTICAL SPECTROSCOPY OF RE IONS DOPED HAFNIA NANOPARTICLES

Doping is a common way to modify band-gaps of nanomaterials and to introduce new energy levels within the energy gap, so that the transitions among these levels produce new optical bands that are not present in the perfect crystal. A well-known way of increasing the luminescence performance of a nanoparticle is based on the incorporation of lanthanide ions into nanocrystals. Especially strong efforts have been put in theoretical and technological researches focused on trivalent RE doped nanoparticles (P. A. Tanner 2005 and Y. Liu 2011). Actually, emissions from trivalent ions are mostly in the visible and near infrared range, which is crucial for light industry, sensing and imaging. From recent years REs doped material have been used even, as contrast agents for medical magnetic resonance imaging and as luminescent chemo-sensors for medical diagnostics and, more recently, for optical imaging of cells (J.C. Bunzli, 2006). At the same time, impurity ions can serve as spectroscopic probes to investigate the dynamic processes occurring in a spatial confined material, together with the modification of the ions spectroscopic characteristics caused by nanodimensional sizes.

RE ions possess $4f^n$ electronic configuration, generating numerous electronic levels. Charge transfer, 4f–5d and f–f transitions are typical occurring electronic transitions in lanthanides. Charge transfer transitions, CT ($4f^n \rightarrow 4f^{n+1} L^{-1}$, where L=Ligand) are allowed by Laporte's selection rules and can be found for rare earth ions which like to be reduced, for instance Ce^{4+}, Pr^{4+}, Tb^{4+}. The *4f–5d* transitions correspond to the promotion of a *4f* electron to a *5d* sub-shell, which are allowed by the parity selection rule. Since *5d* orbits are external and can interact directly with ligands around them, the property of 4f–5d transition

depends largely on the environment of the active ion. Luminescence emissions resulting from the charge transfer and f–d transitions are strong and broad band. On the other side, the intra-configurational $4f^n$ optical transitions are strongly forbidden by the parity selection rule, leading to narrow and weak absorptions and emissions. This selection rule can be somehow relaxed by uneven components of the crystal field that are present when the rare earth ion occupies a crystallographic site without inversion symmetry. These *f-f* electric dipole transitions, termed as the hypersensitive transitions, show large variations in oscillator strengths depending upon the surrounding environment and work as powerful feedback mechanisms for the monitoring of the local crystalline structure (R. Francini, 1997). Recently, hafnium oxide nanoparticles have been synthetized by trivalent europium (Eu) doping (E. Zych, 2009). According to the description above, its luminescence spectrum presents the typical narrow emission related to electric dipole forbidden transition at c.ca 614 nm (Fig. 2.2), while crystal structure, local environment and coordination with ligands in the vicinity of the Eu ions are important factors influencing its optical properties. Hence, its use as dopant has been considered a promising tool for the fine investigation of the host crystal structure (K. Binnesmans, 1996).

2.3.2 CRYSTALLINE PHASE CHANGE INDUCED BY RE IONS DOPING IN HFO_2 NANOPARTICLES

The interest of the research community is now focused toward luminescent materials requiring low manufacturing costs, especially in the field of photonics and laser technology (Y.Shi, 2011 and G.C. Wei, 2009).

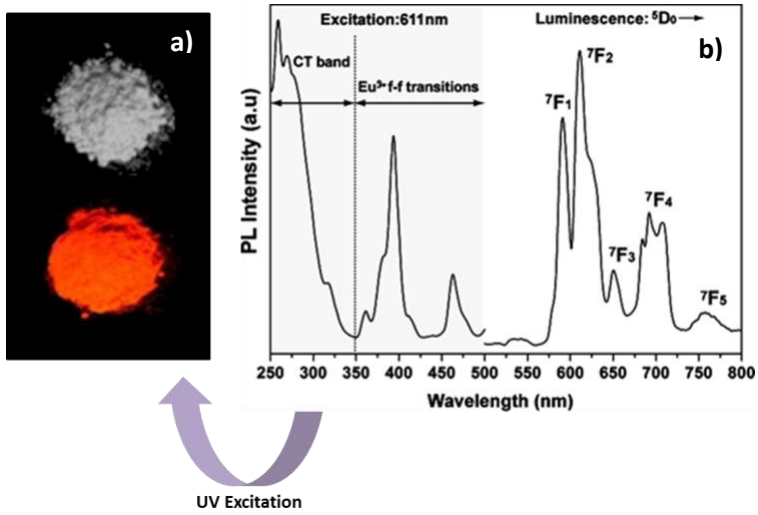

Figure 2.2 | (a) Eu related red emission in inorganic nanopowders under UV irradiation. (b) PL spectra (excited at 265 nm) and PL excitation spectra (monitored at 611 nm) for 10%Eu/HfO2 calcined at 400 °C for 5 h (printed from T. Taniguchi, 2008).

Metal oxide nanomaterials constituted a good solution for this purpose. However, all wet methods lead to the production of metal oxide nanopowders that are affected intrinsically by incident light scattering. Therefore, they have been considered suitable for optical application in the form nanocomposite by embedding of particles into a transparent host. In this case, downscaling of luminescent particles down to the nanometric size is desirable for light scattering minimization. Another strategy to obtain transparent materials is the fabrication of optical ceramics by powder-sintering, where the cubic symmetry is necessary to avoid scattering due to abrupt refractive index changes at grain interfaces (A. Krell, 2009). In such a way, for metal oxide nanomaterials, the ability to control the material structure during the synthesis becomes a powerful tool in the design of their applicability.

A primary limitation to the employment of HfO_2 powders for ceramics relies in the fact that the more stable crystal polymorph at low temperature is the monoclinic one, whereas the stability of the cubic phase occurs only at higher temperature. To this purpose, a lot of synthesis of pure cubic HfO_2 nanoparticles have also been reported, where the authors have demonstrated the importance of the reductive nature of the environment during synthesis, which led to the stabilization of the cubic phase even via post annealing treatment (C.H. Lu, 2008) or without any post-synthesis treatment by the choice of appropriate solvents (P. Rauwel, 2012). However, majority of the studies have required either a divalent or a trivalent dopant that generates oxygen vacancies and in turn stabilizes the cubic phase. Considering the similarity in the chemistry of Hf and Zr, a basic mechanism of stabilization of high-temperature phases in element doped ZrO_2 system is already proposed. The structural change is related to combined effects both of the substitutional ion and the concentration of oxygen vacancies. (L. Gao, 2012) Beyond technological reasons requiring the synthesis optimization to stabilize the cubic phase in nanomaterials, the study on the relationship between luminescence and structural properties of a nanoparticles is still an active investigation field, which can lead to the optimization of the optical characteristics of a metal oxide nanocrystal, such as hafnia.

Araki S. and Yoshimura M. (2004), *Transparent Nano-Composites Ceramics by Annealing of Amorphous Phase in the HfO_2-Al_2O_3-$GdAlO_3$ System.* International Journal of Applied Ceramic Technology, Vol. 1, No. 2.

Binnesmans, K. and Gorller-Warland, C. (1996), *Application of the Eu^{3+} ion for site symmetry determination*. J. Rare Earths 1996, 14, 173–180.

Bünzli J. C. (2006), *Benefiting from the unique properties of lanthanide ions.* Accounts of Chemical Research, 39, 53-61.

Clark R. D. (2014), *Emerging Applications for High K Materials in VLSI Technology*. Materials 7, 4, 2913-2944.

Choi J. H.et al. (2001), *Development of hafnium based high-k materials–A review.* Material Science Engineering. R, 72, 97-136.

Cushing B. L. et al. (2004), *Recent advances in the liquid-phase syntheses of inorganic nanoparticles*. Chemical Reviews 104, 3893–3946.

Feofilov S. P. (2002), *Spectroscopy of dielectric nanocrystals doped by rare-earth and transition-metal ions,* Physics of the Solid State, 44, 8, pp. 1407–1414.

Francini R. (1997), *Spectroscopy of rare-earth ions in insulating materials*. Proc. SPIE 3176, Tunable Solid State Lasers, 2, doi:10.1117/12.293423.

Gao L. et al. (2012) *Stabilization of cubic structure in Mn-doped hafnia*. Ceramics International, 38, 3, pp. 2305–2311.

Kanemitsu Y. and Ishizumib A. (2006), *Luminescence properties of impurity-doped semiconductors nanoparticle*. Journal of Luminescence 119-120, 161-66.

Kirm M.et al. (2005), *Thin films of HfO_2 and ZrO_2 as potential scintillators*. Nuclear Instruments and Methods in Physics Research A. 537, 251–255.

Krell A.et al. (2009), *Transmission physics and consequences for materials selection, manufacturing, and applications.* J. Eur. Ceram. Soc. 29, 207–221.

LeLuyer C. et al. (2008), *HfO_2:X (X = Eu^{3+}, Ce^{3+}, Y^{3+}) sol gel powders for ultradense Scintillating Materials.* Journal of Physical Chemistry A, 112, pp. 10152-10155.

Liu Y. et al. (2011), *Optical spectroscopy of lanthanides doped in wide band-gap semiconductor nanocrystals*. Journal of Luminescence, 131, 3, 415–422.

Lu C.H. et al. (2008), *Cubic phase stabilization in nanoparticles of hafnia-zirconia oxides: Particle-size and annealing environment effects*. Journal of Applied Physics 103, 124303.

Matović B. et al. (2012), *Synthesis and characterization of nanometric yttrium-doped hafnia solid solutions.* Journal of the European Ceramic Society, 32, Issue 9, 1971–1976.

Niederberger M. et al. (2005), *Non-aqueous routes to crystalline metal oxide nanoparticles: Formation mechanisms and applications*. Progress in solid state chemistry, 33, pp. 59-70.

Pearton S. J. and Ren F. (2013), *Wide bandgap semiconductor one-dimensional nanostructures for applications in nanoelectronics and nanosensors*, Nanomater. Nanotechnol. 3:1. doi: 10.5772/56188.

Peralov T. V. and Gusev E. (2006), *Defects in high-k gate dielectric stacks*. 423–434, Springer. Printed in the Netherlands.

Pinna N. et al. (2004), *Non-aqueous synthesis of high-purity metal oxide nanopowders using an ether elimination process.* Advanced Materials, 16, pp. 2196–2200.

Rauwel P. et al. (2012), *One step synthesis of pure cubic and monoclinic HfO2 nanoparticles: Correlating the structure to the electronic properties of the two polymorphs*. Journal of Applied Physics, 112, 104107.

Shen G. (2009), *Devices and chemical sensing applications of metal oxide nanowires*. Journal of Materials Chemistry, 19, 828–839.

Shi, Y. et al. (2011), *Microstructure, Optical, and Scintillation Characteristics of Pr^{3+} Doped $Lu_3Al_5O_{12}$ Optical Ceramics*. Journal of Applied Physics, 109, 013522–7.

Tanner P. A. (2005), *Synthesis and Luminescence of Nano-Insulators Doped with Lanthanide* Ions, J. Nanoscience and Nanotechnology. 5, 1455–1464.

Taniguchi T.et al. (2008), *Rational hydrothermal route to monodisperse $Hf_{1-x}Eu_xO_{2-x/2}$ solid solution nanocrystals.* Journal Physical chemistry C, 112, pp. 4884-4891.

Terki R. et al. (2008), *Cubic-to-tetragonal phase transition of HfO_2 from computational study.* Materials Letters, 62, pp. 1484-1486.

Wang J. Li H. P., Stevens R. (1992), *Review: Hafnia and hafnia-toughened ceramics* Journal of Materials Science, 27, 5397-5430.

Wang-Zhong L. (2008), *Splendid one-dimensional nanostructures of zinc oxide: a new nanomaterial family for nanotechnology.* ACS Nano, 2, 10, pp. 1987–1992.

Wei G. C. (2009), *Transparent ceramics for lighting*. Journal of the European Ceramic Society 29, Issue 2 237–244.

Wiatrowska A. et al. (2010), *Monoclinic HfO_2:Eu X-ray phosphor*. Radiation measurements, 45, 493-496.

Zhao X. and Vanderbilt D. (2002), *First-principles study of structural, vibrational, and lattice dielectric properties of hafnium oxide*. Physical Review B 65, 233106.

Zych E. et al. (2009), *Radioluminescence and photoluminescence of hafnia-based Eu-doped phosphors.* Optical Materials 31, 12, 1764–1767.

3. PROPERTIES OF UNDOPED HfO_2 NANOPARTICLES

In this chapter, we report the optical features observed in undoped HfO_2 nanocrystals. The investigations aim at a better comprehension of the relationship between particle morphology and luminescence.

This work has been developed in collaboration with the Multifunctional Materials Laboratory at the Department of Materials of EHT in Zurich (Switzerland), where the nanoparticles (NPs) has been synthesized, as fully described below, and their structural and morphological analysis has been perfumed, as described in Appendix A. In order to shed light on the relationship between structural and luminescence properties, the spectroscopic characterization of NP by means of photoluminescence (PL) and radioluminescence (RL) techniques has been performed at the Department of Materials Science at the University Milano Bicocca in Milano (Italy).

3.1 SYNTHESIS AND LUMINESCENCE CHARACTERIZATION OF HfO_2 NANOPARTICLES

Hafnium oxide (HfO_2 or hafnia) possesses outstanding properties in terms of dielectric constant, density and chemical resistance (J. Robertson, 2006); unfortunately, the very high melting point (2774 °C) makes it difficult to grow as bulk single crystal using conventional melt growth methods such as a Czochralski, Bridgman, and micro-pulling down (S. Kurosawa, 2012; H.Fujimori, 2001 and F. Cardarelli, 2008). This drawback limits the production of HfO_2 to the deposition of thin films or ceramic powders. (S. Lange, 2007; S. Lange, 2006)

More recently, the development of chemical synthesis (B. Cushing, 2004) allowed the preparation of several metal oxide micro- and nanocrystals (A. Wiatrowska, 2010; C. LeLuyer, 2008). Smaller particles usually show higher phase homogeneity, sinterability, and enhanced and tunable physical and chemical properties, which make them good candidates for the substitution of the bulk phase material (D. Koziej, 2014). With the aim of controlling the growth and thus the size and shape of nanosized objects, several approaches, such as sol-gel methods and the ultrasonically assisted hydrothermal treatment, have been explored. A good synthesis protocol is provided by the non-aqueous solution routes, which offer at the same time several advantages, such as high crystallinity at low temperatures, robust synthesis parameters and ability to control the crystal growth.(N. Pinna, 2004) The synthesis of metal oxide nanoparticles is obtained through the reaction between a solvent (for instance benzyl alcohol) and metal oxide precursors such as alkoxides or chlorides (M. Niederberger, 2006). In the following, the non-aqueous synthesis of the HfO_2 nanoparticles investigated in this work will be described (Fig. 3.1).

3.1.1 SYNTHESIS OF UNDOPED HfO_2 NPs

Hafnium(IV) tert-butoxide (99.99%+Zr) was purchased from Multivalent Laboratory, Eriswell, UK. Benzyl alcohol anhydrous (99.8%) was purchased from Sigma-Aldrich. All precursors were used as received without further purification. Syntheses by non-aqueous sol-gel were carried out in a glove box (O_2 and H_2O < 0.1 ppm). In a typical synthesis, Hafnium (IV) t-butoxide was added to anhydrous benzyl alcohol (BnOH) into a glass test tube. The reaction mixture was transferred into a Teflon liner of 45 mL, slid into a steel autoclave (acid digestion

vessel mod. 4744 by Parr Instrument Company, USA) and carefully sealed. The autoclave was taken out of the glove box and heated in a furnace at 220 °C for 96 hours. The synthesis resulted on a milky suspension that was centrifuged; then the precipitate was thoroughly washed with diethyl ether (Aldrich) and so dried in air at 60 °C overnight. For the annealing, the powders were placed in quartz crucibles and heated in a muffle oven with a heating rate of 10 °C/min; the samples were kept at the final temperature for 2 hours. Temperatures from 400 up to 1000 °C were considered.

3.1.2 SYNTHESIS OF DOPED HfO_2 NPs

a) Doping by rare earth ions.

   Hafnium(IV) tert-butoxide (99.99%+Zr) and lutetium acetate hydrated were purchased from Multivalent Laboratory, Eriswell, U.K. Europium(III) acetate hydrate (99.99%), terbium(III) acetate hydrate (99.9%), and benzyl alcohol anhydrous (99.8%) were purchased from Sigma-Aldrich. Non-aqueous sol-gel syntheses were carried out. For europium and lutetium doped samples, the appropriate volumes of the acetates, pre-dissolved in BnOH, were mixed to the solvent before addition of the Hf precursor. A total amount of 2.4 mmol of precursor and a total volume of 20 mL mixtures were used. For comparison of the optical properties, some samples were annealed in air up to 1000 °C.

b) Doping by titanium ions.

   For the 0.5 mol% Ti-doped sample, the appropriate amount of $TiCl_3$ (Sigma-Aldrich) was mixed to the solvent before addition of the Hf precursor. A total

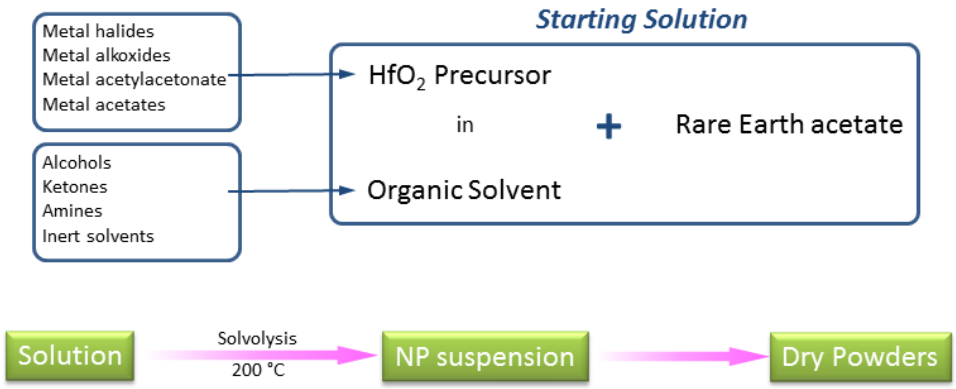

Figure 3.1 | logical outline of the synthetic procedure used to fabricate undoped and RE ions doped hafnia

amount of 2.4 mmol of precursors and a volume of 20 mL BnOH were used. The powders were placed in quartz crucibles and heated in a muffle oven with a heating rate of 10 °C/min. The samples were kept at 1000 °C for 2 hours.

3.1.3 LUMINESCENCE MEASUREMENTS

Hafnia nanoparticles have been studied by means of steady-state and time-resolved photoluminescence (PL) techniques, as well as radioluminescence measurements (RL).

Steady-state PL spectra were measured at RT by a xenon lamp as excitation source, together with a double monochromator (Jobin-Yvon Gemini 180 with a 1200 grooves/mm grating), and recorded through a nitrogen cooled CCD detector coupled to a monochromator (Jobin-Yvon Micro HR).

Time-resolved PL spectra (5 nm of bandwidth), and PL decay (20 nm of bandwidth at 490 nm) of undoped hafnia were collected by means of an

Edinburgh FLS980 fluorescence spectrometer operating in Time Correlated Single Photon Counting configuration with pulsed LED source at 250 nm or 340 nm (pulse duration 600 ps, repetition rate 100 ns or 50 μs). For time-resolved photoluminescence (PL) measurements at RT of doped samples, a Varian Eclipse spectrofluorimeter was used.

The RL measurements were carried out at RT using a homemade apparatus featuring, as detection system, a charge coupled device (CCD) (Jobin-Yvon Spectrum One 3000) coupled to a spectrograph operating in the 200-1100 nm range (Jobin-YvonTriax 180). The data were corrected for the spectral response of the detection system. RL excitation was obtained by X-rays irradiation through a Be window, using a Philips 2274 X-ray tube with tungsten target operated at 20 kV.

3.2 Structural and Morphological Properties

In this work, HfO_2 NPs are used as a model system to interpret the relationship between the optical properties of the material and its morphology at the nanoscale by analyzing their evolution while morphological changes are imparted during calcination.

From the in-situ XRD analysis of the HfO_2 nanopowders (Fig. 3.2a) the main structural effect of the annealing seems to be a gradual sharpening of diffraction peaks. This is due to surface restructuring and lattice reconfiguration (i.e, crystal growth, sintering, and rearrangement of lattice defects) induced by annealing, while the monoclinic structure is kept substantially unmodified. Despite

preserving a relatively small crystal size (still few tens of nm after annealing at 1000 °C) a considerable level of aggregation is observed in the TEM micrographs already for powders treated at 400 °C and above (Fig.3.2b-e). These simultaneous phenomena of the material transformation are associated to a partially distorted lattice configuration, leading to a certain degree of disorder, which is reflected in Raman vibrational modes slightly broadened and shifted towards lower wavenumbers (Fig. 3.3).

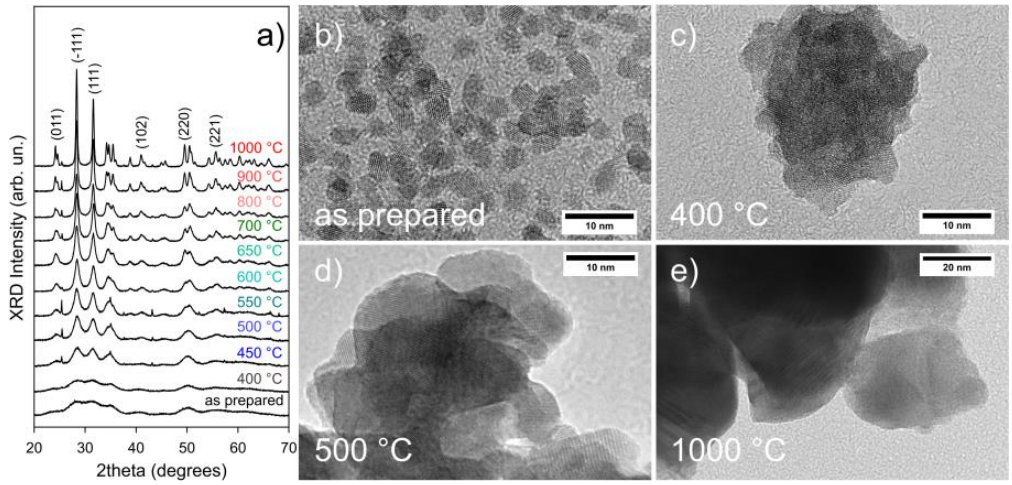

Figure 3.2 | Structural evolution of monoclinic hafnia NPs annealed at different temperatures. In situ XRD analysis performed on undoped HfO_2 reveals a significant crystalline domain growth starting at 450 °C (a). HR-TEM micrographs of "as prepared" nanoparticles (b) and of powders annealed at 400, 500, and 1000 °C (c, d and e, respectively).

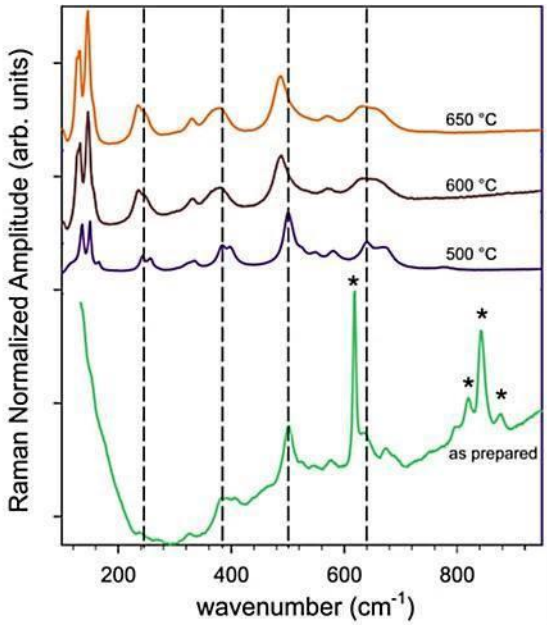

Figure 3.3 | Raman spectra recorded on HfO_2 NPs treated at different temperatures, namely from bottom to top: as prepared NPs (green curve) with benzoate capping, NPs treated at 500 °C (blue curve), at 600 °C (brown curve), and 650 °C (orange curve). The benzoate peaks visible in the untreated sample (marked with stars) disappear after annealing. Dashed lines indicate the typical spectral positions of hafnia vibrational modes for the lowest and the highest annealing temperatures. The annealing at temperatures of 600 and 650 °C, reveal Raman modes slightly broadened and shifted towards lower wavenumbers, possibly indicating a lower level of mid-range order of the nanocrystalline lattice, and altered interatomic distances.

3.3 PHOTOLUMINESCENCE

PL measurements were performed on thermally annealed undoped HfO_2 NPs. In Fig. 3.3, some of the PL spectra obtained under 4.4 eV (280 nm) continuous wave (CW) excitation for low (Fig. 3.4a-b) and high (Fig. 3.4c) temperature treated samples are shown as a function of energy. The PL spectrum of the powder treated at 450 °C shows a broad composite emission ranging from 1.5 eV to 3.9 eV. The main effect of the annealing is the narrowing

of the NPs luminescence. Together with the disappearance of the UV component, we can notice a decrease of all the visible bands with the only exception of an emission in the blue region. This emission, centered at 2.5 eV (490 nm), increases with temperature and dominates the PL spectrum when the sample is treated at 1000 °C. All the PL spectra were deconvolved into Gaussian components using the Levenberge - Marquardt algorithm. The fit was performed using four bands whose energy (E) and width (FWHM) values are reported in Table 3.1. Fig. 3.4a-c reports the obtained deconvolution, with Gaussian fits that are in very good agreement with the experimental curves.

3.3.1 THE ORIGIN OF THE BLUE BAND

The assignment of luminescence emissions to some specific defect centers is usually a challenging task. In the following, we focus mostly on the blue emission detected in our NPs. The detailed analysis of the 2.5 eV band and of its dependence upon thermal treatments allowed us to reveal some aspects of its complex nature. A blue emission in metal oxide NPs, like HfO_2 and the structurally equivalent ZrO_2, was already observed and tentatively attributed to optically active intrinsic defects and self-trapped excitons (E. Rauwel 2014 and X. Bai, 2012). Specifically, in hafnia, a band at 2.7 eV (459 nm) has been explained in terms of the presence of oxygen vacancies (T. Perevalov, 2014). On the other hand, other authors suggested an extrinsic nature for a similar band observed in ZrO_2, due to the presence of some unintentional impurities like hafnium, iron, and titanium which act as primary activators (R. Carvalho, 2015). Among the known different impurities in zirconia, Ti is the most probable candidate to show luminescence. The Ti^{3+} ($3d^1$) ion can be easily photoexcited and, through the radiative 3d1 ($e_g \rightarrow t_{2g}$) transition, it emits light at about 2.5

eV. With the aim to disclose the nature of the 2.5 eV luminescence in our HfO_2 NPs, we compared the excitation-emission features of samples calcined at increasing temperatures, with those of a sample intentionally doped with titanium (0.5 mol% nominal concentration) and treated at 1000 °C.

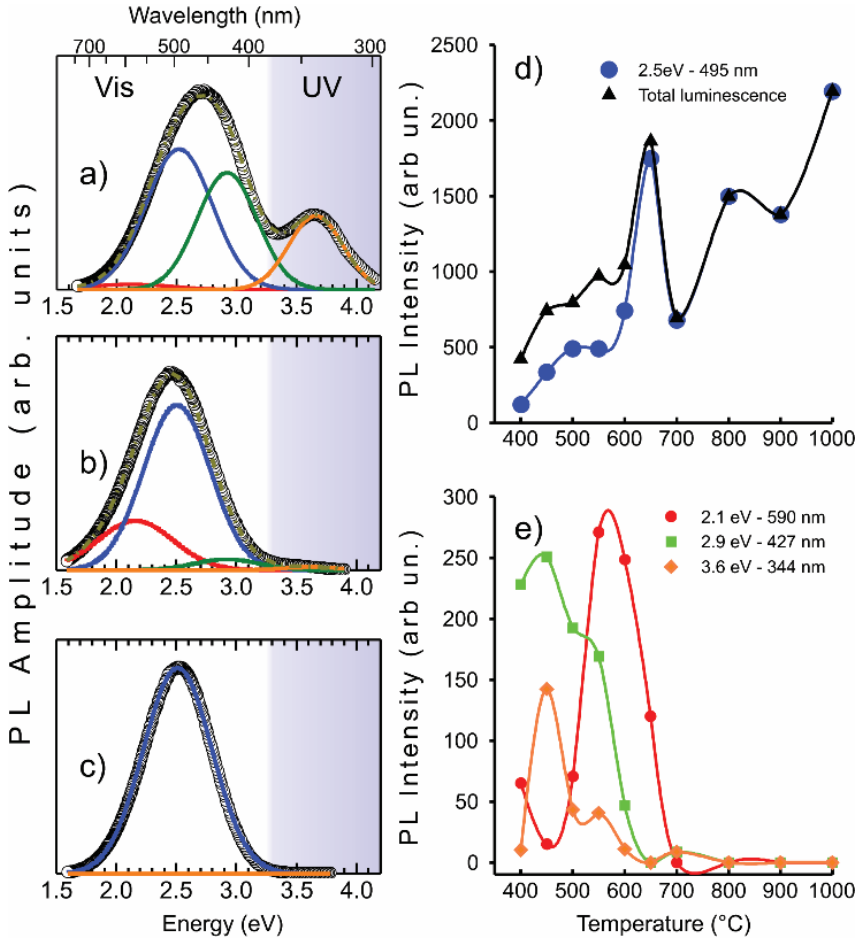

Figure 3.4 | Dependence of the optical emissions of HfO_2 nanopowders excited at 4.4 eV (280 nm) on the annealing temperature. (a), (b), (c) PL spectra of samples heated at 450, 600 and 1000 °C, respectively. Gaussian components (full lines) obtained by the numerical fit are shown together with experimental curves (markers). (d) Total emission intensity (black) and intensity of the 2.5 eV component (blue) depending on the annealing temperature. (e) Intensity of the thermally unstable components at 2.1, 2.9 and 3.6 eV (red, green and orange, respectively). In panels (d) and (e) the full lines are guides for the eye.

Table 3.1 | Results of the Gaussian fit of the luminescence excited at 280 nm (4.4 eV).

Samples	Band A		Band B		Band C		Band D	
	E (eV)	FWHM	E	FWHM	E (eV)	FWHM	E (eV)	FWHM
HfO2:Ti	-------	---------	2.51	0.66	-------	---------	-------	---------
1000°C			2.51	0.67				
900 °C	-------	---------	2.49	0.68	-------	---------	-------	---------
800 °C	-------	---------	2.50	0.69	-------	---------	-------	---------
700 °C	-------	---------	2.50	0.69	2.92	0.59	3.62	0.58
650 °C	2.16	0.73	2.51	0.65	-------	---------	-------	---------
600 °C	2.16	0.74	2.51	0.66	2.92	0.64	3.62	0.53
550 °C	2.16	0.73	2.48	0.69	2.95	0.60	3.62	0.53
500 °C	2.16	0.73	2.51	0.69	2.92	0.59	3.62	0.53
450 °C	2.12	0.78	2.52	0.59	2.92	0.59	3.66	0.53
400 °C	2.16	0.73	2.48	0.65	2.96	0.64	3.62	0.58

As representative examples, in Fig. 3.5 the photoluminescence and photoluminescence excitation (PL-PLE) spectra of undoped NPs annealed at the lowest and at the highest temperatures (400 and 1000 °C respectively) are shown, together with those of HfO_2:Ti. Relevant differences are noticed. When the undoped sample is treated at low temperature (Fig. 3.5a), the PLE shows a dominant component at 3.5 eV (350 nm) accompanied by a shoulder at about 4.4 eV. By exciting the NPs in the dominant band at 3.5 eV, a composite spectrum is obtained displaying the 2.5 eV emission and two additional components peaking at 2.1 (590 nm) and 2.9 eV (430 nm). Their spectral positions and half-widths are similar to those of the bands obtained under 280 nm excitation (Fig. 3.4). At variance, in samples treated at 1000 °C the excitation spectrum monitored at 2.5 eV emission reveals the presence of a dominant excitation component at almost 4.4 eV (Fig. 3.5b). Moreover, the excitation at this energy leads to only one emission band at 2.5 eV. Interestingly, in this case the PL-PLE spectra are in good agreement with those of the Ti:HfO_2 sample (dot

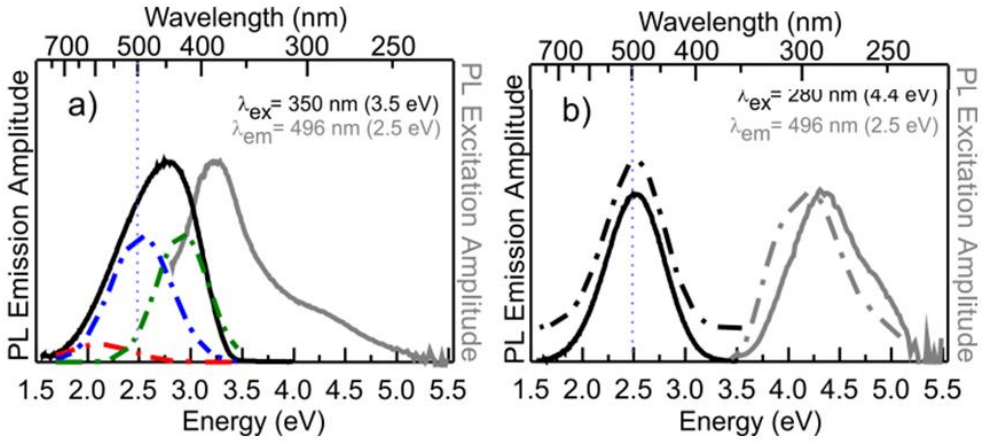

Figure 3.5 | (a) PL excitation (grey line) spectrum monitored at 2.5 eV of HfO2 annealed at 400 °C, together with the PL emission (black lines) spectrum under 350 nm (3.54 eV) excitation. The Gaussian components of the PL spectrum are also shown (red, blue, and green dash-dot lines). The high energy side of the emission spectrum is slightly distorted by the presence of a long-pass filter, reflected on its partial mismatch with the Gaussian fit of the spectrum. (b) PLE of the blue emission and PL spectra under 4.4 eV (280 nm) excitation (grey and black continuous lines, respectively) for the 1000 °C annealed NPs, compared with the Ti doped (5000 ppm) HfO2 calcined at 1000 °C (grey and black dot lines). Vertical dot lines mark the 2.5 eV emission.

lines in Fig. 3.5b). Based on the different excitation spectra reported in Fig. 3.5a-b, a double origin of the luminescence at 2.5 eV can be suggested. i) For high annealing temperature, the emission is efficiently excited at 4.4 eV and it can be associated to a Ti-related transition. ii) At low annealing temperature, the emission is preferentially excited at lower energy, and is possibly associated to intrinsic defects of such NPs as it will be discussed later.

We used time resolved photoluminescence in order to confirm the double nature of the 2.5 eV band. Again, the fluorescence decays of annealed undoped HfO_2 NPs were also compared to that of a Ti doped HfO2 annealed at 1000°C. Fig. 3.6a shows that, if the NPs are annealed at low temperature (450 °C), the PL under irradiation at 4.96 eV (250 nm) decays as a bi-exponential

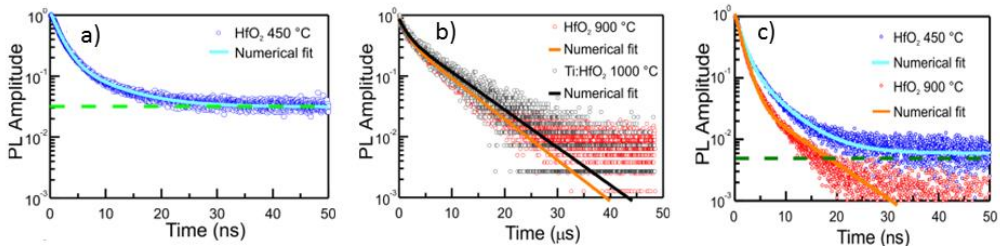

Figure 3.6 | Time resolved photoluminescence spectra of HfO_2 annealed at different temperature under 250 nm (4.96 eV) (a, b) and 340 nm (3.65 eV) (c) pulsed excitation and monitoring at 490 nm (2.5 eV). Numerical fit of the decays appear as full lines.

function with characteristic lifetimes τ_1=1.7 ± 0.2 ns and τ_2= 7.4 ± 1.2 ns (light blue line). Moreover, the high background signal suggests the presence of a third component with a significantly longer decay time, which cannot be appreciated in the nanosecond time range.

After annealing at 900 °C, the PL decay changes dramatically (Fig. 3.6b, red circles). The luminescence still decays as a bi-exponential function, but with decay times τ_1 = 1.3 ± 0.2 μs andτ_2 = 6.7 ± 0.2 μs, three order of magnitude longer with respect to the sample treated at low temperature. In fact, the observed decay is very similar to that of Ti doped hafnia NPs (Fig. 3.6b, black circles). The dominant presence of the Ti-related transition can be explained by the reduction of non-radiative channels induced by the annealing at higher temperatures, which are expected to increase the dimension of the nanocrystals and decrease the concentration of defects .By excitation at 3.65 eV (340 nm) (Fig. 3.6c), where Ti centers are poorly stimulated (Fig. 3.5b), we observe an intrinsic blue PL emission, which shows a decay time similar to the one previously recorded for samples annealed at a lower temperature Fig. 3.6a. The two luminescence components of the sample annealed at 900 °C decay with

lifetimes of τ_1 = 1.3 ± 0.1ns and τ_2 = 7.7 ± 0.8 ns; in accordance with this result, the PL of the low temperature treated NPs decays as a bi-exponential function, with τ_1 = 1.4 ± 0.1 ns and τ_2 = 5.3 ± 0.5 ns. The discrepancy over the PL decay background of the two samples may be due to the presence of other luminescence components, whose emission bands overlap the 2.5 eV one and whose time decays may be longer. In summary, the existence of two distinct emissions at 2.5 eV in low and high temperature treated samples is demonstrated by both their different excitation profiles and very different time decays. Based on these evidences, we performed the analysis of emission spectra while exciting at lower UV energies, namely at 3.5 eV (350 nm). The emission spectra (Fig. 3.7a-c) display the same spectral components revealed under 4.4 eV (280 nm) excitation (Fig. 3.4). However here, in accordance with the above shown results, the band at 2.5 eV is the intrinsic fast emission and not the Ti related one. Again, the overall shape of the spectra is clearly dependent on the annealing temperature as shown by the changes of the relative band intensities (Fig. 3.7d), The two higher energy components (violet at 2.9 eV and blue at 2.5 eV, respectively) decrease with increasing temperatures up to 700 °C, as characteristic of surface defects related emissions.

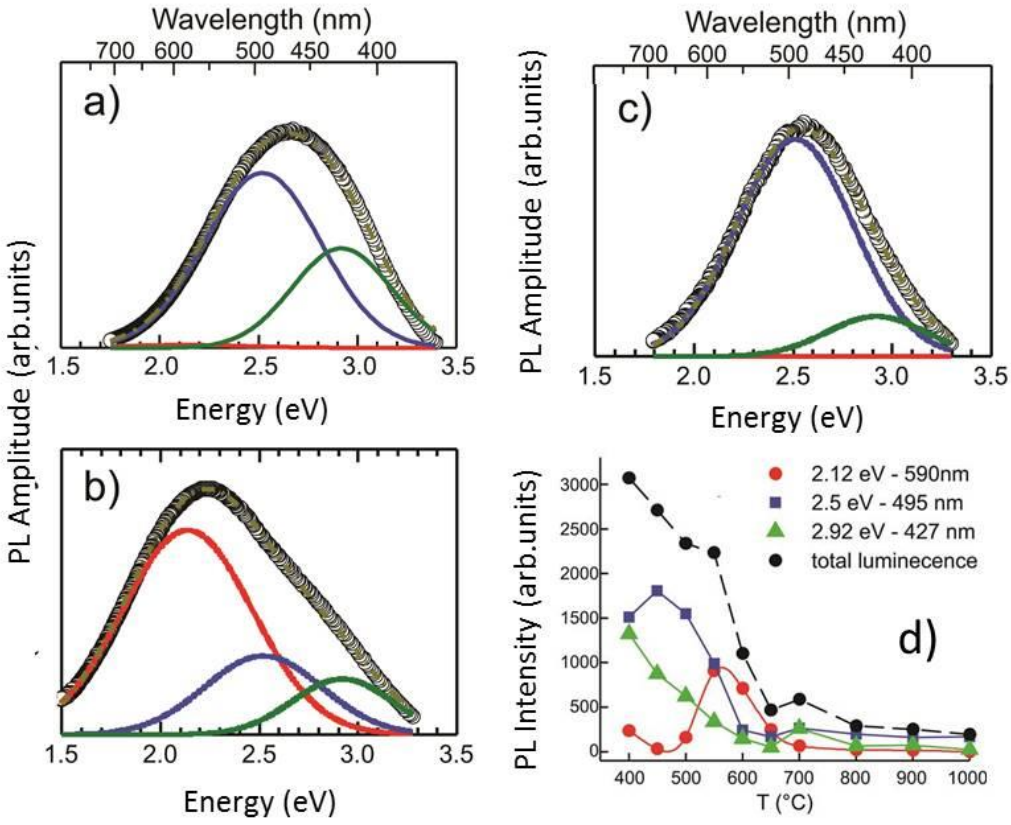

Figure 3.7 | Evolution of visible luminescence of HfO_2 nanopowders depending on the annealing temperature. (a, (b, (c) PL spectra of NPs treated at 450, 600 and 1000 °C, respectively. (d) Absolute intensity of deconvolved components depending on annealing temperature.

3.3.2 TOWARDS WHITE AND COLOUR TUNABLE EMITTING NANOPARTICLES UPON STRUCTURAL CHANGE CONTROL

As shown above, the emission colour of HfO_2 nanocrystals - upon near UV irradiation - turns from blue to cyan by increasing the temperature from 400 up to 500 °C. Therefore, nanophosphors absorbing in this energy region can be implemented in UV-pumped white emitting LEDs. They could be suitable also as downconverting materials for solar application, to recover the near-UV intensity

solar spectrum poorly harvest by commercially available devices (K. Fiaczyk, 2015, X. Huang, 2013, M. Shang, 2014, and B. M. van der Ende, 2009).

As shown in Fig. 3.7, after heating at 600 °C we observed a nearly white emission, while for higher temperatures we recorded a less intense blue emission. The evolution of the sintering process is associated to an increase in the crystal average size, together with the simultaneous decrease of surface specific area. These transformations are reported in the inset in Fig. 3.8, and account for the rearrangement of the nanocrystals towards energy minima where the discontinuities of the lattice are reduced as long as external energy is provided to the material.

The annealing promotes the growth of crystalline domains and is reflected in a lower solid-solid interface at grain boundaries which is inversely dependent on crystal size, while the coalescence of neighbour crystallites (sintering) reflects on a lowered solid-vapour interface which was here evaluated by the measurement of specific surface area (R. H. R. Castro, 2010). These measurements allowed us to suggest that different optically active defects exist in the nanocrystals, located either at inner crystal sites or at grain boundaries. In a polycrystal, the boundaries can be of two kinds: i) solid-solid interfaces between two adjacent crystallites, presenting a mismatch of the crystal lattice orientation, and ii) solid-vapour interfaces, i.e. the surface of crystal domains in contact with the environment. We tried to quantify the area of these interfaces under the assumption that crystallites are of spherical shape, leading to the total specific grain boundary surface, calculated as the total area per unit mass of nanocrystals having average diameter equal to that obtained by TEM and XRD analysis.

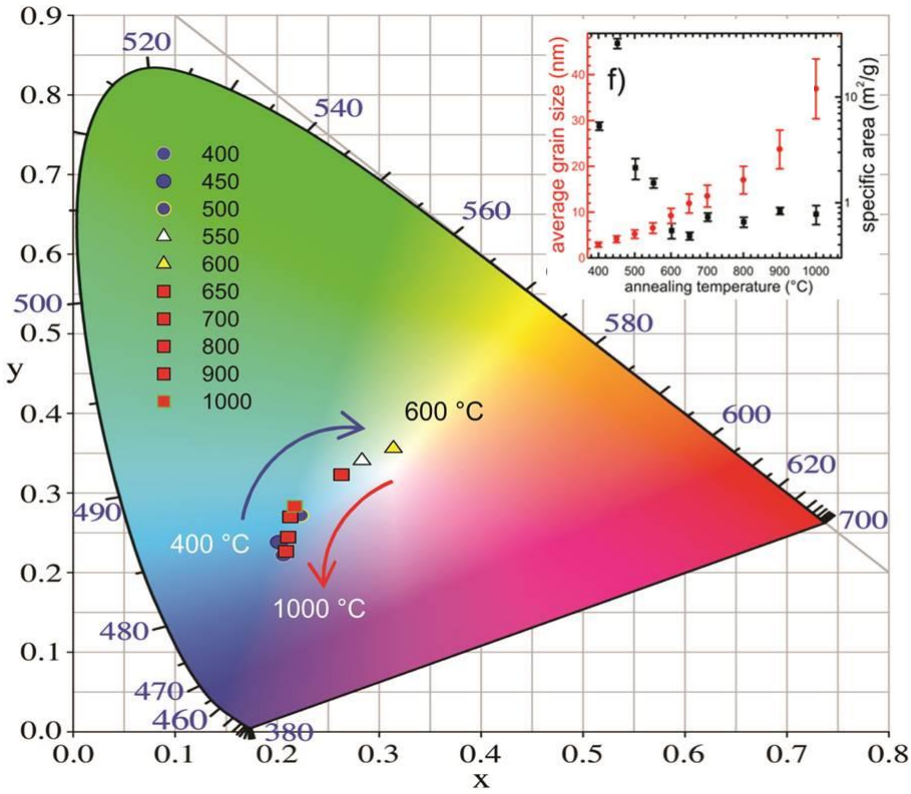

Figure 3.8 | CIE1964 chromaticity diagram reporting the coordinates of luminescent hafnia nanopowders treated at temperatures of 400 - 500 °C (blue circles), 550 °C (white triangle), 600 °C (yellow triangle) and 650 - 1000 °C (red squares). In the inset: specific surface area and average crystal size recorded ex-situ on annealed samples depending on final temperature.

On the other hand, the BET specific surface of the nanopowders was employed to directly measure the solid-vapour interface area. The specific grain boundaries area, i.e. the solid-solid interface, can be reasonably determined as difference between these two quantities. In order to find a correlation between optical emissions and structural configuration, the results of this modelling are shown in Fig. 3.9. The modifications of all these three interface areas during the annealing, arising from crystal growth and sintering phenomena at increasing temperatures, are schematically sketched together with the dependence of the

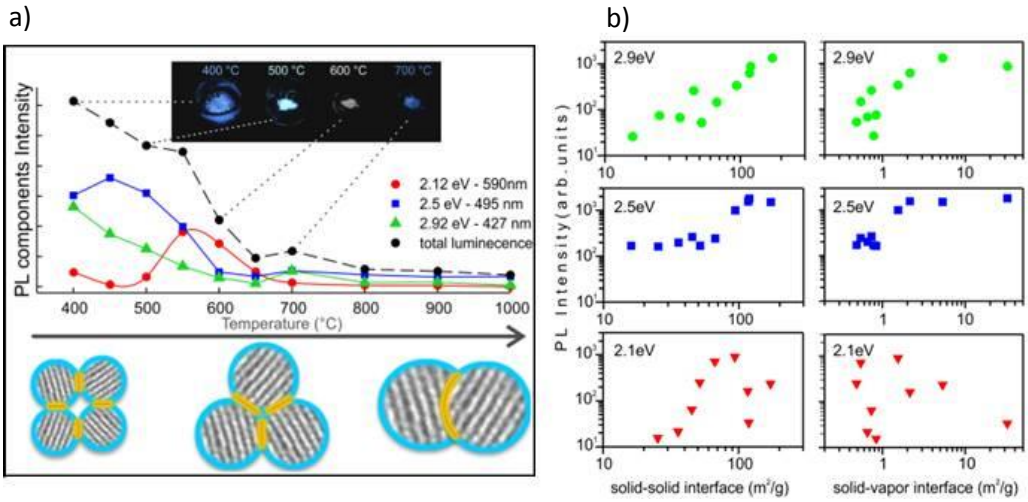

Figure 3.9 | Dependence of the intensities of spectral components detected under 350 nm excitation on the structural parameters derived from measured crystal average size and specific surface area. (a) Dependence on the total crystal interface. A representative scheme of the polycrystal structural evolution during the annealing is also shown. A sketch of the change in the emission colours at different temperatures is shown (b) Dependence of the single components either on the solid-vapour interface (measured as specific surface area by BET, right panels) or the solid-solid interface (determined as a difference between total and solid-vapour interface, left panels).

spectral components (excited at 350 nm where only intrinsic emissions belonging to monoclinic HfO2 are efficiently stimulated) displayed as a function of the different interface zones. The blue components at 2.9 and 2.5 eV show a dependence on the material interface. Their correlation with the total grain interface, shows a similar yet inverse trend with respect to temperature (Fig. 3.9a), because of the monotonic decrease of the surface of the crystallites as their average diameter increases during the annealing (Inset in Fig. 3.8).

Interestingly, these trends are strongly different when the bands intensities are displayed as a function of solid-solid or solid-vapour interfaces, separately.

The band at 2.9 eV shows a clearer linear dependence on the solid-solid interface, suggesting that the defect sites from which this emission originates are possibly located at the boundary between two misaligned crystallites. Inversely, its trend with respect of the solid-vapour interface manifests a plateau for the highest interface areas, possibly suggesting the onset of its quenching due to the interactions with species adsorbed on the outer surface of the nanocrystals. The same consideration can be done for the band at 2.5 eV, though it shows a less linear growing dependence also on the solid-solid interface. The band at 2.1 eV does not show a clear dependence on any of these structural parameters, and seems to be more strictly related to the annealing temperature. This fact cannot be interpreted in a conclusive way, and could be explained also with a partial change in the material composition due to the incorporation of contaminants, arising from the decomposed organic capping, and which are removed or passivated for the highest annealing temperatures. Alternatively, it could also arise from interface defects which are passivated, at the lowest temperatures, by the interaction with species coordinated at the surface, and successively reduced by the lowering of boundaries for the highest temperatures. Despite the nature of this latter band is still unclear, it is worth noticing that, at temperatures between 500 and 650 °C, its occurrence is responsible for the white emission of the material, representing more than 50 % of the total emission.

The photoluminescence efficiency is a crucial parameter for evaluating the potential performance of a material as phosphor in technological

applications. We measured the PL efficiency of the most interesting white emitting HfO_2 NPs treated at 600 °C, by using a LED at 340 nm as excitation source. We measured both the PL quantum yield (QY), defined as the ratio between the number of emitted photons and the absorbed ones, and the PL quantum efficiency (QE), which has been calculated as the ratio between emitted and incident photons. QY has been measured according to the method described in ref. M. S. Wrighton, 1974. The reliability of the methods has been validated experimentally by measuring the PL yield of sodium salicylate as reference sample. The results evidenced that, after heating the hafnia NPs at 600 °C, the nearly white emission features QY and QE of 7.5 % and 3.1 % respectively, which is aligned to values reported in literature for undoped phosphors (X. Chen, 2013 and B. Ho-June, 2009)

3.4 RADIOLUMINESCENCE

The measurement of the RL was employed in order to monitor the role played on the optical properties by the changes associated to annealing. RL measurements were performed on thermally annealed undoped HfO_2 NPs. In Fig. 3.10, the RL spectra of samples al low (a), middle (b), and high temperature (c) are shown as a function of energy. It can be noticed that the RL spectrum of the powder treated at 450 °C shows a broad composite emission in the VIS region. Upon annealing, other new bands in the UV region begin to increase. All the RL spectra were deconvolved into Gaussian components using the Levenberge - Marquardt algorithm. The fit (Table 3.2) was performed using the

same four bands reported in Table 3.1 for the PL spectra and new components have been added when necessary.

Table 3.2 | Results of the Gaussian fit of the luminescence under X-ray excitation.

Samples	Band E		Band F	
	E (eV)	FWHM (eV)	E (eV)	FWHM (eV)
1000°C	4.10	0.66	4.67	0.65
900 °C	4.10	0.66	4.67	0.65
800 °C	4.10	0.67	4.67	0.60
700 °C	4.10	0.65	4.67	0.60
650 °C	4.11	0.67	4.67	0.67
600 °C	4.14	0.65	4.67	0.60
550 °C	4.13	0.62	4.67	0.60
500 °C	4.14	0.62	4.67	0.60.60
450 °C	4.14	0.62	4.71	0.65

A general increase of the luminescence is to be noticed, as reported in Fig. 3.9e-f. Still an emission at 2.5 eV (490 nm) plays a dominant role in the yield enhancement and dominates the spectrum when the sample is treated at 1000 °C.

Even in the RL investigation we tried to explore the possible origin of the blue luminescence. A comparison of the RL spectrum of a Ti doped samples, annealed at 1000 °C is reported in Fig. 3.10d). Its emission properties strongly match with the high temperature HfO_2 treated sample, suggesting the dependence of the 2.5 eV band to the presence of Ti as impurity of the host. Nevertheless it was found (Fig 3.10e) that the RL yield of the undoped nanocystals reaches a value that is almost a 1/3 of the commercial intrinsic

scintillator standard BGO, (Bismuth germinate $Bi_4Ge_3O_{12}$, Fig 3.10g). This represents a good promise for the applicability of HfO_2 nanoparticles, even by controlled Ti impurity doping, as scintillator material.

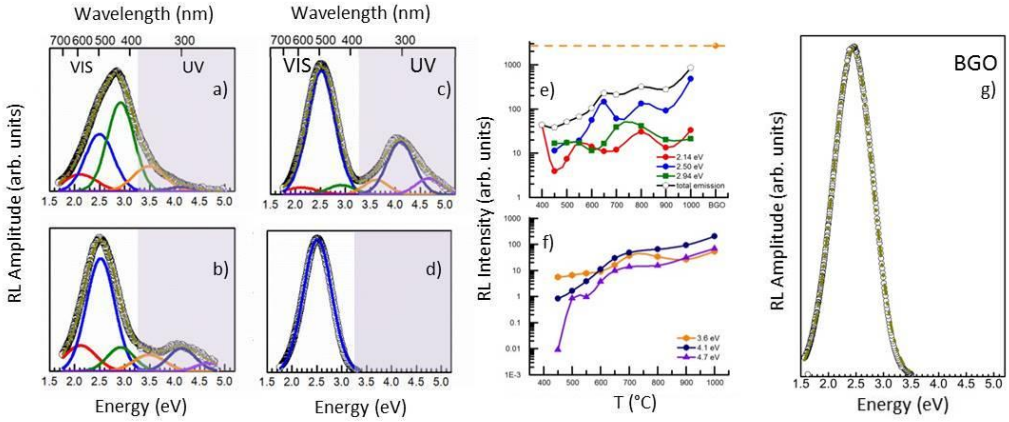

Figure 3.10 | Dependence of the RL emissions of HfO_2 nanopowders upon the annealing temperature. (a) b), c) RL spectra of samples heated at 450, 600 and 1000 °C, respectively. (d) RL narrow emission in 0.5 mol% Ti-doped sample. Gaussian components (full lines) obtained by the numerical fit are shown together with experimental curves (markers). RL efficiencies of hafnia nanoparticles during the heat treatment up to 1000 °C. (e) Intensity of the 2.1, 2.5, and 2.9 eV (red, blu and green respectively), together with the total intensity light output. The comparison with the RL intensity of the BGO (Bismuth germinate $Bi_4Ge_3O_{12}$) standard is reported. (f) Intensity of UV components at 4.6, 4.1, and 4.7 eV (orange, dark blue, and violet respectively. (g) RL spectrum of BGO powder (markers) and its numerical fit (full line) are shown.

3.5 CONCLUSION

In conclusion, the optical properties of the hafnia nanocrystals can be correlated to structural conformation occurring at the nanoscale and during the sintering of the material.

Table 3.3 |Summary the most relevant VIS luminescence band characteristics.

Band	Origin	Comments
2.1 eV	unknown	At intermediate sintering temperatures its intensity covers the 50% of the global NPs luminescence and it significantly contributes to the white emission.
2.5 eV	1. Ti impurity related emission	1. High PL output in high temperature treated samples under UV irradiation. Slow decay time (μs)
	2. Grain boundary localized defects	2. Fast decay time (ns) under near UV irradiation
2.9 eV	Grain boundary localized defects	Its intensity decreases with the enhancement of the sintering temperature

A double nature of the 2.5 eV band has been evidenced (Table 3.3). The first one arises from extraneous impurities of Ti^{3+} ions, denoted by slow decays in the range of microseconds. Secondly, another optically active center emitting at the same wavelength has been recognized, likely of defective nature, with ultrafast decays in the range of nanoseconds. The material exhibits a tunable luminescence under near-UV 350 nm excitation, depending on the structural configuration at the nanoscale. Moreover, the hafnium oxide nanocrystals may represent a good example of dopant-free white light emitting phosphors, implementing the active research in UV-led pumped lighting.

The relevant increase of the RL yield upon high temperature thermal treatment suggests the suitability of undoped hafnia nanoparticles for scintillator applications.

3.6 REFERENCES

Bai, X. et al. (2012), *One-Step Synthesis and Optical Properties of Benzoate- and Biphenolate-Capped ZrO2 Nanoparticles*. Adv. Funct. Mater. *22,* 20, pp. 4275-4283.

Cardarelli F. (2008), *Material Handbook: A Concise Desktop References*. 2nd ed.; Springer Verlag: New York.

Carvalho, J. et al. (2015), *Structure–property relationship of luminescent zirconia nanomaterials obtained by sol–gel method.* J. Mater. Sci*.,* 50*,* 2, pp. 873-881.

Castro, R. H. R. et al. (2010), *Interface Energy Measurement of MgO and ZnO: Understanding the Thermodynamic Stability of Nanoparticles.* Chem. Mater. 22*,* 8, pp. 2502-2509.

Chen X. et al. (2013), *Rare-earth free self-activated and rare-earth activated* $Ca_2NaZn_2V_3O_{12}$ *vanadate phosphors and their color-tunable luminescence properties.* J. Phys. Chem. Solids, 74, 1439.

Cushing B. L. et al. (2004), *Recent Advances in the Liquid-Phase Syntheses of Inorganic Nanoparticles.* Chemical Reviews, 104, pp. 3893-3946.

Fiaczyk, K.et al. (2015), *Photoluminescent Properties of Monoclinic HfO2:Ti Sintered Ceramics in 16-300 K*. Journal of Physical Chemistry C, 119 (9), pp 5026–5032

Fujimori H. et al. (2001), *Internal Distortion in Ceria-Doped Hafnia Solid Solutions: High-Resolution X-Ray Diffraction and Raman Scattering*. Phys. Rev. B., 64, 134104.

Ho-June B. et al. (2009), *Blue, green, and red emission from undoped and doped ZnGa2 O4 colloidal nanocrystals.* Nanotechnology, 20, 495602.

Huang, X. et al. (2013), *Enhancing solar cell efficiency: the search for luminescent materials as spectral converters.* Chem. Soc. Rev., 7, 42(19, pp. 173-201.

Koziej D.; et al. (2014), *25th Anniversary Article: Metal Oxide Particles in Materials Science: Addressing All Length Scales*. Adv. Mater, 26, pp. 235-257.

Kurosawa S. et al. (2012), *Investigation of a Tb-doped HfO2 Single Crystal Grown by a Skull Melting Method.* Key Engineering Materials, 508, pp. 81-86.

Lange S. et al. (2006), *Luminescence of Re-Ions in HfO_2 Thin Films and Some Possible Applications*. Opt. Mater., 28, pp. 1238-1242.

Lange S. et al. (2007), *Luminescence of ZrO_2 and HfO_2 Thin Films Implanted with Eu and Er Ions*. Physica status solidi (c), *4*, pp. 938-941.

LeLuyer C et al. (2008), *HfO_2:X (X = Eu^{3+}, Ce^{3+}, Y^{3+}) Sol Gel Powders for Ultradense Scintillating Materials*. J. Phys. Chem. A, 112, pp. 10152-10155.

Niederberger M. et al. (2006), *Non-aqueous synthesis of metal oxide nanoparticles: Review and indium oxide as case study for the dependence of particle morphology on precursors and solvents.* Journal of Sol-Gel Science and Technology, 40, pp. 259–266.

Perevalov, T. et al. (2014), *The origin of 2.7 eV luminescence and 5.2 eV excitation band in hafnium oxide.* Appl. Phys. Lett.**,** 104*,* 7, 071904.

Pinna N. et al (2004), *Non-Aqueous Synthesis of High-Purity Metal Oxide Nanopowders Using an Ether Elimination Process*. Adv. Mater., 16, pp. 2196-2200.

Rauwel, E. et al. (2014), *Photoluminescent cubic and monoclinic HfO2 nanoparticles: effects of temperature and ambient.* Mater. Res. Express 1*,* 1, 015035.

Robertson J. et al.(2006), *High Dielectric Constant Gate Oxides for Metal Oxide Si Transistors.* Rep. Prog. Phys., 69, pp. 327-396.

Shang, M. et al. (2014), *How to produce white light in a single-phase host?* Chem. Soc. Rev.**,** 43*,* 5, pp. 1372-1386.

Van der Ende, B. et al. (2009), *Lanthanide ions as spectral converters for solar cells.* Phys. Chem. Chem. Phys*.* 11, 47, pp. 11081-11095.

Wiatrowska A. et al. (2010), *Monoclinic HOf2:Eu X-Ray Phosphor*. Rad. Meas., 45, 493-496.

Wrighton M. S. et al. (1974), *Technique for the determination of absolute emission quantum yields of powdered samples*. J. Phys. Chem., 78, 22, pp. 2229–2233

4. PROPERTIES OF DOPED HfO_2 NANOPARTICLES

The luminescence of hafnia nanoparticles (NPs) under UV and X-ray irradiation will be reported. The role of their doping with rare earths (RE) ions has been studied both from the point of view of the structural related optical properties and of the achievement of the low-temperature stabilization of the hafnium oxide (HfO_2 or hafnia) cubic phase, throughout trivalent RE ions incorporation into the host. The possibility of tuning the colour of the emission by multiple RE doping, while changing the lattice crystal phase has been explored.

4.1 FROM MONOCLINIC TO CUBIC PHASE: A STRUCTURAL AND RL INVESTIGATION

Doping is the introduction of trace impurity elements in order to tune the properties of a material. The recent increasing use of trivalent lanthanide (Ln^{3+}) ions finds its reasons in enhancing the metal oxide nanoparticles (such as hafnia) properties, while widening the field of their applications. At the same time, the active studies on the technological importance of undoped and rare doped hafnia, underline the need to control the crystal lattice structure and to stabilize the high temperature phases of HfO_2 nanocrystals and films at room temperature (L. Gao, 2012). In this work, we achieved the stabilized cubic phase of HfO_2 through Ln^{3+} incorporation in the lattice during the non-aqueous sol-gel synthesis method. In order to probe the effectiveness of phase change, as well

as to active the luminescence, we investigated the strong site symmetry sensitivity of 4f-4f emissions of Eu^{3+}.

The aim of obtaining the NPs crystal cubic phase is strictly connected to production of optical ceramics. Due to its high melting point, hafnia single crystals cannot be synthetized with the normal routes. A solution for the productions of transparent ceramics is the use nanometric materials with cubic symmetry that strongly reduce the light scattering and even the birefringence, thus enhancing the optical performance of the ceramic.

We refer to hafnia nanocrystals doped with rare earths ions as follows: HfO_2:RE x mol % (RE = Lutetium (Lu), Europium (Eu); x = nominal concentration in the initial solutions). Samples doped with more than one element are named as HfO_2: RE1/RE2/RE3 (c1, c2, c3 mol %). All samples are mentioned according to the nominal concentration (c1, c2, c3) in the initial solutions.

4.1.1 Europium Doped Nanoparticles

A result of the non-aqueous sol- gel route, HfO_2 nanophosphors doped with $Eu3^+$ have been prepared. Fig. 4.1 shows the morphology of hafnia nanoparticles doped with different amounts of the optically active ions. Despite the fact that the first aim of doping is the optimization of nanophosphors optical properties, it is worth to notice that Eu^{3+} doping concentration influences both structural and optical modifications in the host. TEM analyses allow concluding that the synthesis leads to the formation of well dispersed nanoparticles with an elongated shape, while agglomeration of nanoparticles is not observed (Fig. 4.1a-d). The linear dimension of nanoparticles has been measured to be ca. 3.0 ± 0.4 nm. At the same time, high resolution images (Fig. 4.1b, d) show very clear

lattice fringes that evidence the high crystalline grade of nanoparticles, irrespective of the doping level.

Table 4.1 | Induced Coupled Plasma (ICP) elemental analysis of doped HfO_2 NPs.

Nominal composition of $Hf_{(1-x-y)}Lu_xEu_yO_2$ NPs		at% measured by ICP		
		Hf	Lu	Eu
x	y	1-x-y	x	y
-	0.01	0.987	-	0.013
0.10	0.01	0.842	0.150	0.008
-	0.08	0.931	-	0.069

Above a certain value, the concentration of trivalent dopant ion is able to induce a crystal lattice phase change, as depicted for ZrO_2 where a few percent of trivalent ions incorporated into the lattice stabilizes the cubic polymorph (C.H. Lu 2008, M. Bhagwat 2003 and P. Li, 1994). The electron diffraction pattern recorded on the sample doped with 10 mol % Eu is compatible with the cubic structure (Fig. 4.1e), while the undoped NP structure remains monoclinic. In order to confirm that the incorporation of the trivalent ions has been successful, ICP elemental analysis has been performed. The results (Table 4.1) confirm that the concentration of Eu in the samples matches with the nominal one. As an example, from ICP measurement the nominal 8 mol % Eu corresponds to an actual concentration value of 6.9 mol %.

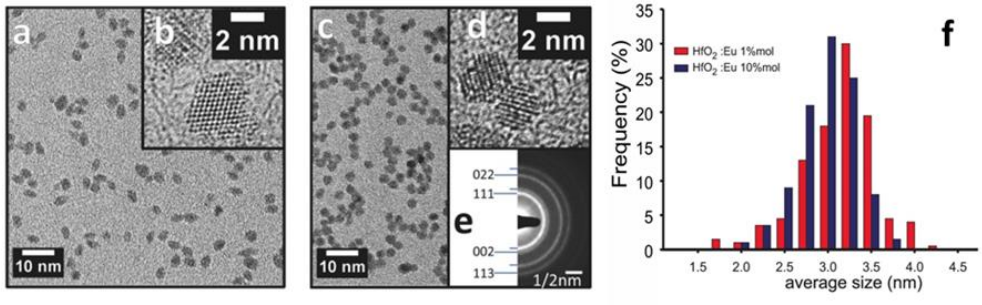

Figure 4.1 |(a and c) TEM micrographs of HfO2:Eu 1 mol % and HfO_2:Eu 10 mol %NPs, respectively; (b and d) HRTEM image of single particles of the same samples, respectively; (e)electron diffraction of cubic phase of HfO_2:Eu 10 mol %NPs;(f) particle size distributions of the 2 and 10 mol %Eu doped nanopowders.

A more detailed description of the structural modifications induced by doping is depicted in Fig. 4.2 (Left). The expected monoclinic structure of hafnium dioxide is observed for Eu^{3+} concentrations up to 3 mol %, as shown by XRD (Fig. 4.2left) according to reference ICDD PDF no. 00-006-0318. For RE concentrations exceeding 5 mol %, the diffractogram is converted to that of cubic HfO_2. Consequently, the threshold value for the stabilization of cubic hafnia at room temperature could be set above 5 mol %. In fact, the HfO_2:Eu 5 mol % NPs exhibit occurrence of both structures presenting minor features of the monoclinic phase while the majority of the peaks are ascribable to the cubic one. Considering the small volume of individual NPs, this fact could be explained by the incorporation of a sufficient number of trivalent ions inside a partial fraction of nanocrystals.

The analysis of the 4f-4f transition emission in the red spectral region, stimulated by X-ray radiation (Fig. 4.2right), confirms the threshold of Eu concentration in order to change the host crystal phase.

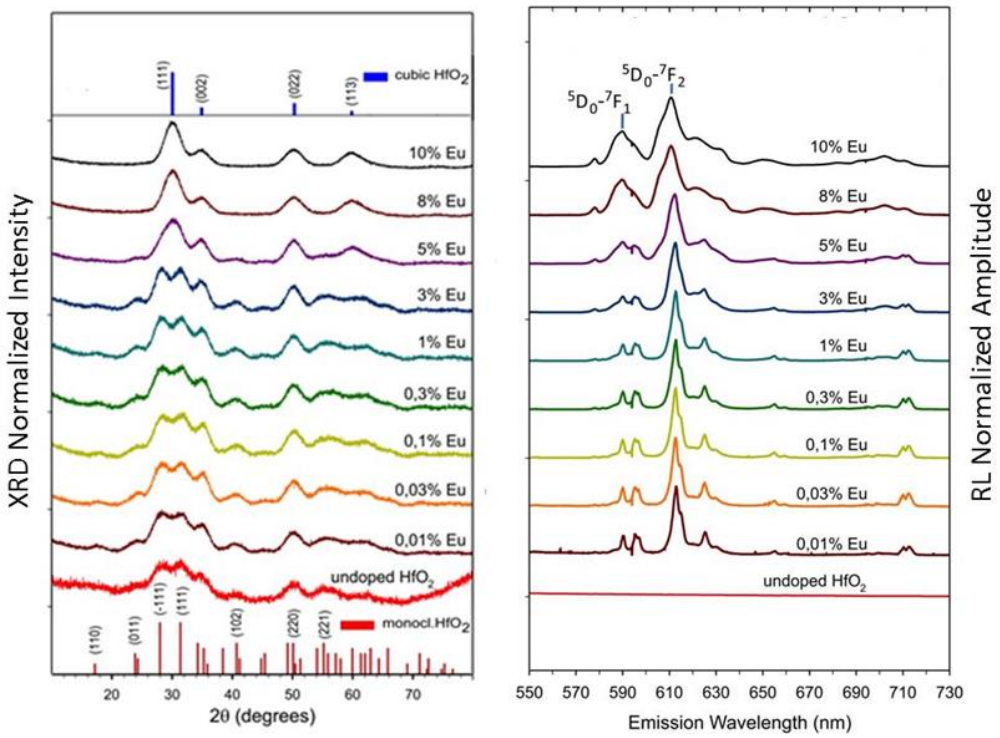

Figure 4.2 |Structural parameters and optical emission properties of HfO_2 nanoparticles depending on the molar concentration of Eu^{3+} used as dopant. (Left) XRD patterns. Bar plots are the calculated diffractograms from reference patterns. (Right) RL spectra. For concentration of trivalent dopant higher than 5 mol %, both diffractograms and RL emissions exhibit a clear change corresponding to the stabilization of the cubic phase.

The structural modification is reflected by the RL emission properties, where two families of spectra could be recognized, with an exact correlation with the crystalline structure. A dominant $^5D_0$-$^7F_2$ emission line (at almost 613 nm) is observed in the radiative recombination of charge carriers at Eu^{3+} sites for all monoclinic hafnia nanopowders. Because this hypersensitive transition is strongly forbidden, its presence proves the lack of inversion symmetry of Eu^{3+}sites. In contrast, cubic samples show a modified emission shape towards a higher symmetry of the RE ions (E. Zych 2002, E. Zych 2009). The increasing local

symmetry is evidenced by the relative intensities of $^5D_0$-$^7F_1$and $^5D_0$-$^7F_2$ transitions turning out to be more similar. Nevertheless, the presence of the $^5D_0$-$^7F_2$ line and the rather large width of all optical emissions reflect the presence of different slightly distorted surroundings for Eu^{3+} incorporated inside the nanoparticles or at surface sites.

4.1.2 Lutetium Doped Nanoparticles

Another way to stabilize the cubic hafnia polymorph has been investigated by employing another non-emitting RE ion with a stable trivalent at a similar concentration level. The aim of such a study was to obtain cubic NPs to be purposed for ceramic materials with the lowest concentration of optically active doping ions, avoiding drawbacks like the concentration quenching of the luminescence. Thus, it is preferable to arrange luminescent ions concentrations according exclusively to the emission spectrum required, while designating an optically inactive ion to the structural stabilization. Lu is a good ion for operating fine structural modifications because it is optically inert. Therefore, the stabilization of hafnia might be obtained by Lu incorporation with a minimum perturbation of the luminescence properties. The Lu doped HfO_2 powders show a trivalent ion concentration dependent morphology and structure, similar to the case of HfO_2:Eu. In Fig. 4.3a-d TEM analysis reveals the formation of ultrasmall isolated NPs with a slightly elongated appearance. The average diameter was measured to be ca. 3.1± 0.4 nm, with a quite regular size distribution, irrespective of the Eu or Lu doping levels (Fig. 4.3e).

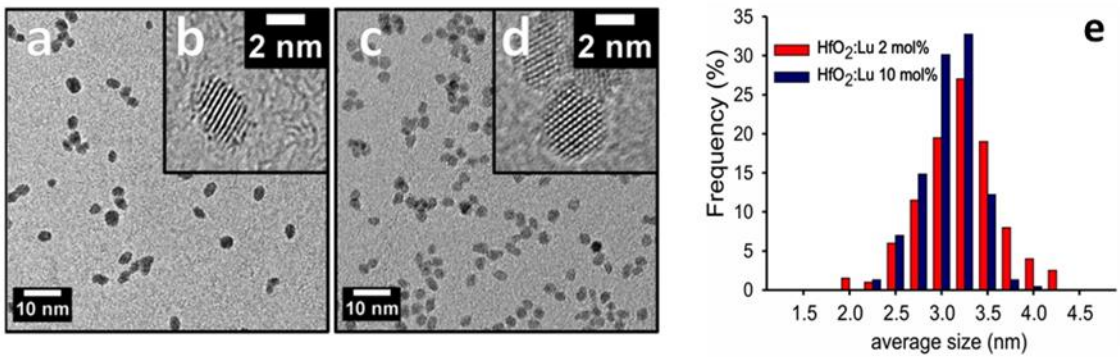

Figure 4.3 |TEM micrographs of Lu doped HfO_2 NPs: (a) 2 mol % and (c) 10 mol % doped; insets (b and d) HRTEM of highly crystalline single particles of the same samples, respectively; (e) particle size distributions of the 2 and 10 mol % Lu doped hafnia nanopowders

The role played by Lu in the structural rearrangement of HfO_2nanophospors is displayed in Fig. 4.4a, by means of the XRD diffractograms measured on the undoped, 2 mol % Lu, and 2 mol % Lu + 1 mol % Eu doped nanopowders, together with the 10mol % Lu, and 10mol % Lu + 1 mol % Eu doped ones. In all these samples, containing a total level of trivalent incorporated REs of few (from 0 to 3) mol %, the monoclinic lattice is able to host the dopant without changing its geometry and their XRD patterns are comparable to the reference pattern of pure monoclinic hafnium dioxide (ICDD PDF no. 00-006-0318). For a total doping exceeding 5 mol %, a structural rearrangement is observed, and the cubic polymorph features can be seen on XRD. The broadening of XRD peaks accounts for the nanosized morphology of crystallites, well below 5 nm in linear length. Energy dispersive spectroscopy (EDS) analysis (Fig. 4.4b) shows values for final concentration of Lu in good agreement with the ICP values in Table 4.1 and with the nominal ones.

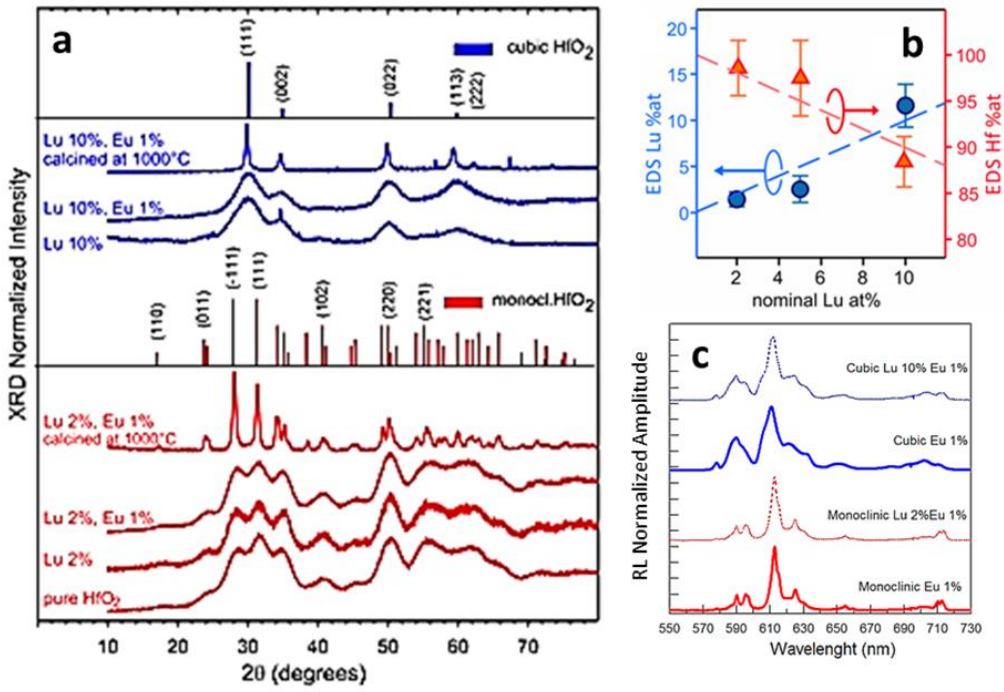

Figure 4.4 |Structural parameters and optical emission of HfO_2 nanoparticles depending on the molar concentration of Lu^{3+} used as dopant. (a) XRD patterns (bar plots: diffractograms from reference patterns) before and after annealing at 1000 °C. (b) EDS analysis of Lu and Hf atomic concentrations depending on nominal Lu (dashed lines represent theoretical concentrations). (c) RL spectra of samples with incorporation of Lu^{3+} (2 and 10 mol %) in the lattice and a smaller concentration Eu (1%). Only 10 mol % Lu stabilizes the cubic polymorph of the NPs. The luminescence of Eu in Lu doped samples replicates that of samples doped by Eu only, in both monoclinic and in cubic lattice phase. All curves are shifted over the ordinate axes for clarity.

The effect of the structural change on luminescence properties is reported in Fig. 4.4c. Data recorded on samples prepared only with 1 and 10 mol % Eu, are also shown for comparison. As in this last case, the luminescence spectra of Eu and Lu co- doped NPs are modified by the phase change induced by increasing impurities level, inserted into the system during the synthesis procedure. RL spectra manifest the red luminescence corresponding to the f-f transitions of europium centers, whose relative intensity varying according to the crystal lattice and to the activator site symmetry. The hypersensitive emission at c.ca

613 nm dominates only the monoclinic NPs spectra, as due to a stronger distortion of the Eu local site.

4.1.3 HIGH TEMPERATURE EFFECT ON THE NPS STRUCTURE

In the last part of the chapter, we present the structural evolutions of Eu^{3+}-doped HfO_2 and Eu and Lu co-doped NPs as a function of the annealing temperature. For this reason, powder samples have been annealed in air up to 1000 °C and examined. The results of the annealing can be seen in the XRDs of Fig. 4.4a, where the NPs doped with both low and high concentration of Lu and 1 mol % Eu show the sharpening of peaks after their calcination. Moreover, although preserving the assigned structure on the basis of the measurements presented before, highly doped samples exhibit a more stabilized cubic phase, as demonstrated by the now more reliable match with the reference pattern (ICDD PDF no. 00-053-0560). The thermal promotion of crystal growth may be responsible of gradual increase of the crystalline degree of the NPS and, thus, of the sharpening of the XRD peaks. Fig. 4.5d describes the XRD transformation during annealing of cubic HfO_2:Lu 10 mol % NP, revealing a crystallite size growth from 2.9 to 23.0 nm, obtained by applying the Scherrer formula on the diffraction peak located at $2\theta = 30°$.

The effect of the removal of residual organic molecules from the NPs surface has been analysed under their thermal behaviours. Indeed, the special nature of non-aqueous sol-gel route involves the solvolysis of precursor molecules governed by benzyl alcohol at lower temperature with respect to the other wet and vapour-based approaches (Pechini, Sol Gel, Atomic Layer Deposition) (J. Meng, 2010). This promotes the formation of organic species

coordinated to the surface of the inorganic material (M. Niederberger, 2009). A description of this phenomenon is needed, in order to predict the evolution of the nanomaterial properties, like agglomeration state and phase transformations, after successive thermal treatments. Therefore, Fig. 4.5a-b shows the typical TGA and DSC profile of dried as prepared NPs. A weight loss of 12% at around 450 °C associated with the main exothermal events is ascribed to the thermal decomposition of organic residuals present in the system. The vibrational spectroscopy analysis on as prepared and annealed products, through FT-IR absorption measurements recorded on ATR configuration, show the presence of bands at 1598, 1497, and 1450 cm^{-1} assigned to phenyl ring C=C stretch modes, while the peaks at 1545 and 1427 cm^{-1}could be ascribed to the asymmetric and symmetric stretching of COO^- groups, respectively (K. D. Dobson, 2000; C. A. Koutstaal, 1993). The absence of OH stretching bands in the 2500-3000 cm^{-1} range suggests the presence of benzoate groups coordinated to the nanoparticles surface, disappearing after annealing in air at 1000 °C. The Raman investigation on the same materials (Fig. 4.5c) exhibits peaks at 618, 1004, and 3066 cm^{-1} typical of phenyl rings of benzoate, together with HfO_2 vibrational modes signals at 377, 399, 495, 552, 586, 641, and 670 cm^{-1}.(X. Bai 2012, B. K. Kim, 2002, H. Fujimori, 2001, P. E. Quintard, 2002) The modes of benzoate groups decomposed as the powders are calcined above 500 °C. As expected, thermal treatments have a double effect: on one hand the nanoparticles growth and their aggregation, on the other hand the removal of organic species from the particles surfaces.

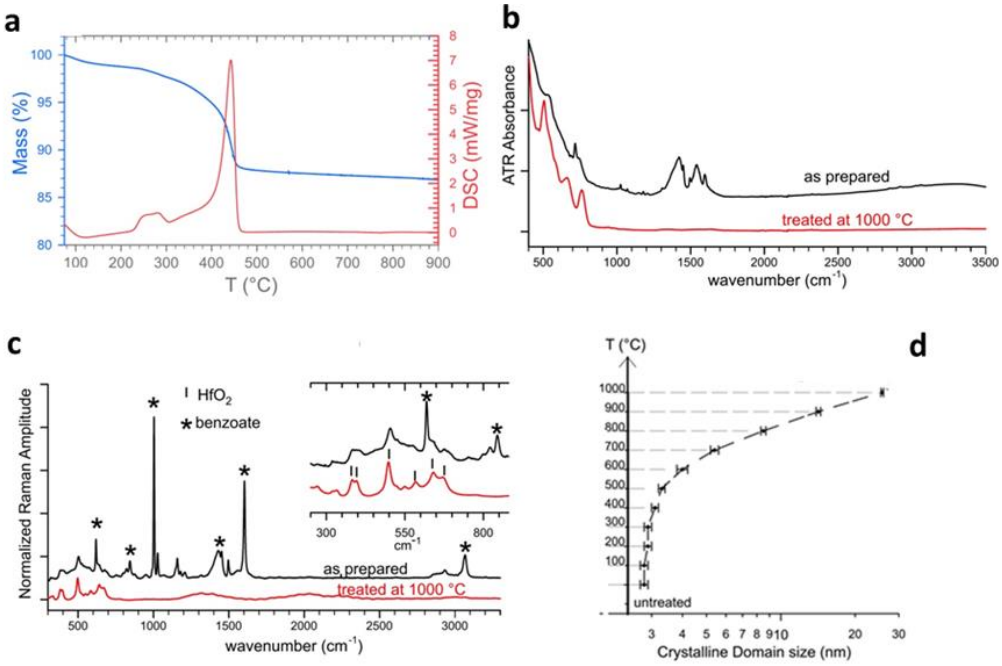

Figure 4.5 |(a) TGA (blue line) and DSC (red line) curves of 10 mol % Lu doped HfO2 nanopowders. (b) ATR-FTIR absorption of as prepared 2 mol % Lu (black line) and calcined 10 mol % Lu doped (red line) HfO2 powders. (c) Raman spectra of as prepared 2 mol % Lu (black line) and calcined10 mol % Lu doped (red line) HfO2 powders; inset shows spectra enlarged in the low wavenumbers region (asterisks mark Raman modes of benzoate species, vertical lines mark Raman modes of HfO_2). (d) Increase of crystalline domains as measured by XRD of 10 mol % Lu doped HfO2 NPs and calculated according to the Scherrer formula. The temperature related increase of the NPs diameter was found also in only Eu doped samples (not reported).

4.1.4 HIGH TEMPERATURE EFFECT ON THE NPS LUMINESCENCE

These above described structural modifications are reflected in a change in the luminescence properties, both in the RL spectrum components and in its total efficiency. In Fig. 4.6 the optical emissions under X-ray irradiation of 4f-4f transitions of Eu^{3+}, used as probe for the crystal symmetry level on a set of Lu/Eu doped and Eu doped samples are reported. RL spectra of monoclinic NP are completely unaffected by the thermal treatment (not reported), while a further

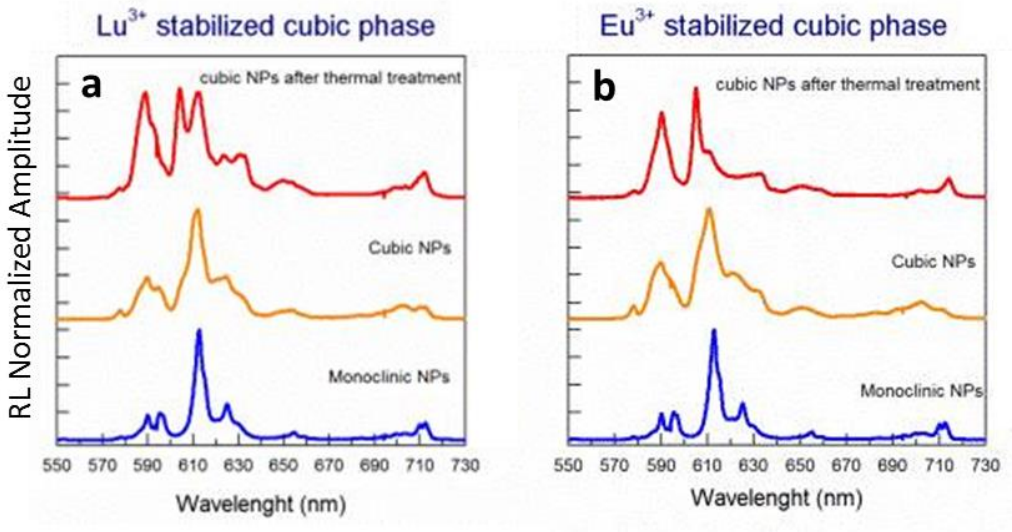

Figure 4.6 | Effect of the thermal treatment on RL properties of lanthanide doped hafnia nanoparticles. As optical probe, we use the typical emission of Eu^{3+} ions. For high Ln^{3+} concentration, i.e. in Lu 10 mol % and in Eu 10% mol cubic samples, the RL modification after calcination suggests an enhancement of the Eu site symmetry. All curves are shifted over the ordinate axes for clarity.

lattice ordering is promoted for the cubic phase nanopowders. It has to be pointed out that the relative intensity between $^5D_0$-$^7F_1$ (590 nm) and $^5D_0$-$^7F_2$ (613 nm) transitions is close to 1 in thermal treated samples. This reflects a very high symmetry of the Eu^{3+} site in the calcined samples, which is also evidenced by the clear observation of both $^5D_0$-$^7F_1$ and $^5D_0$-$^7F_2$ splitted components thanks to the local crystalline field effect.

The role played on the optical properties by the changes of morphology and structure associated to annealing, may affect even the total yield of the luminescence. The measurements of the RL efficiency of Eu and Eu/Lu co-doped HfO_2 are reported in Fig. 4.7a, both before and after annealing. Untreated NPs show a monotonic increase of the RL efficiency with the Eu concentration up to

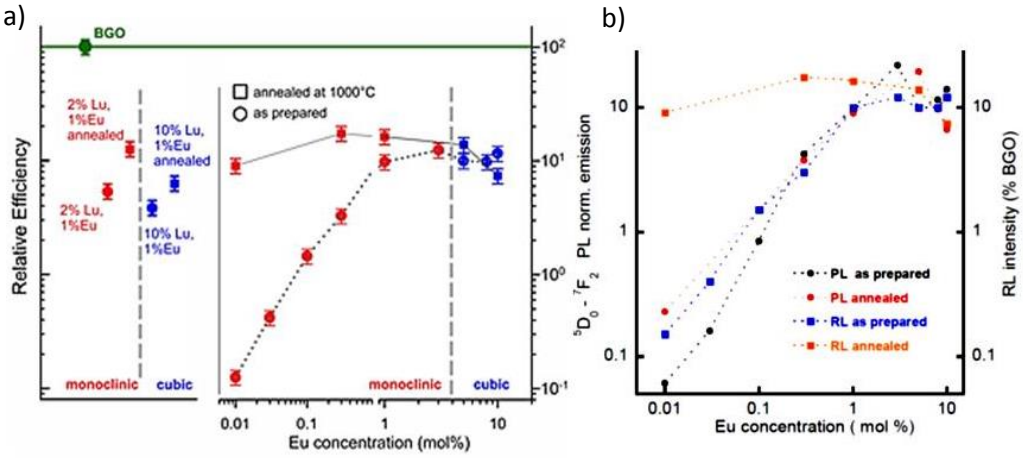

Figure 4.7 | (a, left) RL efficiencies of hafnia nanoparticles co-doped with Lu (2 and 10 mol %) and Eu (1 mol %), before and after heat treatment at 1000 °C (BGO shown as reference). (a, right) RL efficiencies of as prepared (dotted line) and treated (full line) Eu doped HfO_2 NPs, depending on nominal Eu concentration (values determined as integrals over the 500-750 nm range of RL spectra recorded in the same conditions). (b) Comparison of PL amplitude of the $^5D_0$-$^7F_2$ transition and RL efficiencies (relative to BGO) depending on Eu concentration, in as prepared and calcined powders (the same PL trends are observed by analyzing the amplitude of the $^5D_0$-$^7F_1$ transition). For a better visualization of trends, the PL values were scaled so to be equal to the RL one for the untreated sample doped with 5 mol % Eu. The experimental error on PL measurements was estimated to be circa 50% of the measured amplitude.

1 mol %, followed by a nearly constant signal up to 10mol %. After annealing, a considerably higher RL signal is observed at low Eu concentrations, which however does not increase significantly by varying the Eu content for higher dopant value. A similar situation has been found for the Lu co-doped samples, revealing that neither the dopant types nor the host polymorph effect the luminescence efficiency. The study of the intensity of steady state PL emission measurements using the same excitation and emission conditions completes the study of the effect of the annealing on the NPs optical properties (Fig. 4.7b).

Interestingly, the PL efficiency is not significantly modified, indicating that the removal of surface defects, shown in Raman and FT-IR spectra (Fig. 4.5) and due to the high temperature treatment, does not play a role in the PL. The striking differences between PL and RL efficiencies after annealing can be explained considering that the radiative emission at Eu^{3+} centers occurs in RL only after a fast transport stage of free carriers, which migrate in the lattice losing their energy until they are captured by Eu ions. In this migration stage, carriers can also be trapped by defects, finally reducing the efficiency of radiative recombination. Therefore, it can be argued that the reduction of defect states after annealing is also reflected in a much efficient carriers transfer to Eu luminescent ions occurring during the RL measurement. Also, the saturation of the signal increase observed in annealed sample as a function of the dopant level has been explored. We suppose that this effect could be related to the occurrence of concentration quenching for heavy dopings, especially after the annealing of the NPs. It could be in fact assumed the coexistence of multiple luminescence sites in the same very small nanocrystal, before annealing. On the other hand, the calcined powders are expected to show a higher degree of compaction, a lowered average distance between luminescence sites, and the consequent stronger quenching of the luminescence at minor Eu^{3+}concentration values. In Fig. 4.8 the time resolved PL spectra on untreated and calcinedHfO_2 and by monitoring the $^5D_0$-$^7F_2$ transition are shown. The thermal treatment removes non-radiative channels caused by organic residuals (absent after calcination) and surface defects (reduced by crystal growth), which are responsible for a slight decay distortion and a decay lengthening at high Eu concentrations (Fig. 4.8a) in the untreated samples. In turn, the results obtained on all annealed samples by exciting at 290 nm (Fig. 4.8b), does not reveal any

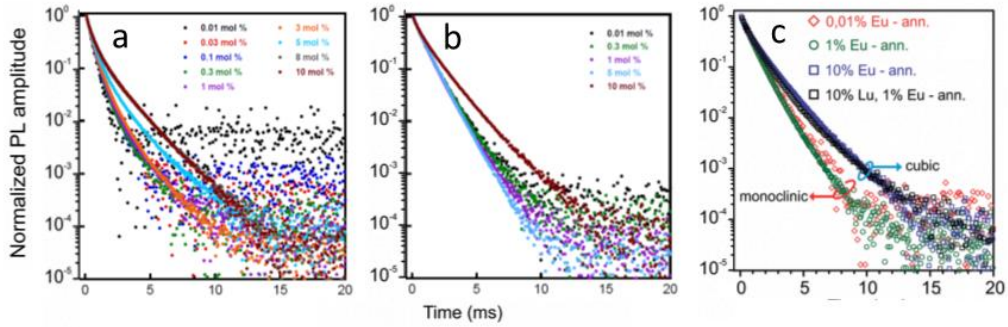

Figure 4.8 | Room temperature PL time decays of untreated Eu doped HfO^2 nanoparticles λ_{exc} = 290 nm, λ_{em}= 613 nm(a) before and (b) after annealing. (c) Comparison of room temperature PL decays between Eu doped and Lu co doped HfO_2 nanoparticles after annealing at 1000 °C (λ_{exc} = 290 nm, λ_{em} = 613 nm).

clear sign of decay acceleration or distortion depending on the doping. On the contrary, Fig. 4.8c, shows a decay time increase, likely related to structural parameters, that is the modification from the monoclinic to the cubic lattice. Indeed, the time decay of the Eu emission increases in cubic phase samples because of the low local field distortion of the symmetric sites. Concluding, although the lack of RL increase above 1 mol % Eu for untreated samples and in the whole concentration range for calcined samples could suggest the presence of concentration quenching effects, no evidences of this phenomenon have been observed from time decay of PL decay at 612 nm.

4.2 Tuning The Emission Colour of Doped Hafnia NP

The study conducted above suggests the possibility of changing the emission properties of hafnia nanopowders even at low concentration of dopants, because of the crystal lattice phase modification obtained varying the

concentration of Ln^{3+} ions, like optically inactive Lu. The tunability of luminescence colour in structurally modified HfO_2 NPs is illustrated in Fig. 4.9, showing RL spectra of nanopowders and photographs of their suspensions in ethanol under UV laser excitation. It is observed that the addition of Tb ions, together with Eu, gives rise to a composite luminescence spectrum featuring also the green lines at 490 and 550 nm belonging to the $^5D_4$-$^7F_{5,6}$ transitions of Tb^{3+}. As long as the total doping is only 2 mol %, the structure is unchanged and monoclinic hafnia nanophosphors are obtained. When adding also 10 mol % Lu, the structural stabilization of the cubic polymorph is actuated. The emission profile is slightly modified, since the relative ratio between Tb^{3+} and Eu^{3+} emissions is increased in the cubic structure with respect to the monoclinic one, thus suggesting that the NP structure can affect the energy transfer between the two emitting ions.

Finally, the PLE and PL data of HfO2:Lu/Eu (10, 1mol %) powder are reported in Fig. 4.10. The excitation spectrum of the $^5D_0$-$^7F_2$ transition at 613 nm shows the charge transfer (CT) band peaking at 285 and 293nm before and after the thermal treatment, respectively, whereas the Eu^{3+} transitions from $^7F_{0,1}$ levels are significantly increased by calcination (Fig. 4.10a). The PL emission spectrum of the untreated sample excited at 364 nm is dominated by a broad blue band, which vanishes by exciting at 292 nm where, in turn, only Eu^{3+} red emission is detected (Fig. 4.10b). After the thermal treatment, the UV excited PL emission is dominated by the forbidden $^5D_0$-$^7F_2$ transition of Eu^{3+}, although a broad band at the higher energy side of the spectrum is observed, by exciting at 364 nm. Hence, the material exhibits an evident spectral emission modification by slightly changing the excitation wavelength, also depending on thermal treatment. The inset in Fig. 4.10c shows photographs of cubic phase HfO_2 NPs

(Eu 10 mol % and Lu/Eu (10/1 mol %), respectively) illuminated with the two lines of a common Wood's lamp. Here, the 365 nm line well excites the blue emission and only partially excites the Eu-related red emission. Therefore, the excitation with the lower energy line results in a pink emission for the higher concentration of europium, whereas the blue component dominates in the sample with only 1 mol % Eu.

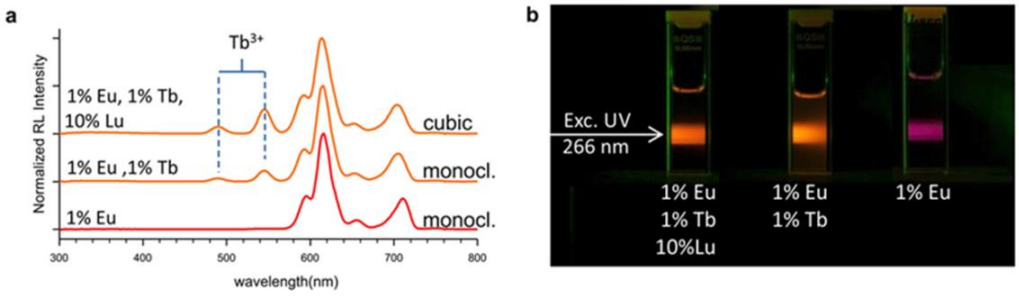

Figure 4.9 | (a) RL of HfO_2:Eu 1 mol %, HfO2:Eu/Tb (1, 1 mol %), and HfO_2:Lu/Eu/Tb (10, 1, 1 mol %) NPs, from bottom to top, respectively. Spectra are shifted over the ordinate axis for clarity. (b) Photograph of the same NPs suspended in ethanol, recorded under 266 nm NdYAG laser illumination.

4.3 CONCLUSION

In this work, by a facile synthesis approach hafnium dioxide nanoparticles have been obtained through a strategy where RE dopants are employed both as luminescent activators and as cubic structure stabilizers. The additional incorporation in the lattice of optically inactive Lu ions is effective in order to operate the structural stabilization of the cubic polymorph at room temperature, leaving the role of luminescence activator to Eu ions present in

small concentration. Although the deep comprehension of such materials confined into nanometric dimensions deserves further investigations, the data reported represent an important result in the investigation of the relationship between structural and optical properties in nanometric materials. The crystalline phase and luminescence properties strategy control by doping applied in this work increases the room for further applications of HfO_2 as nanoscintillators, and to produce transparent ceramics or nanocomposites that could be employed in optoelectronics. Moreover, it represents a powerful tool toward a higher control of the overall functional and structural properties of innovative materials.

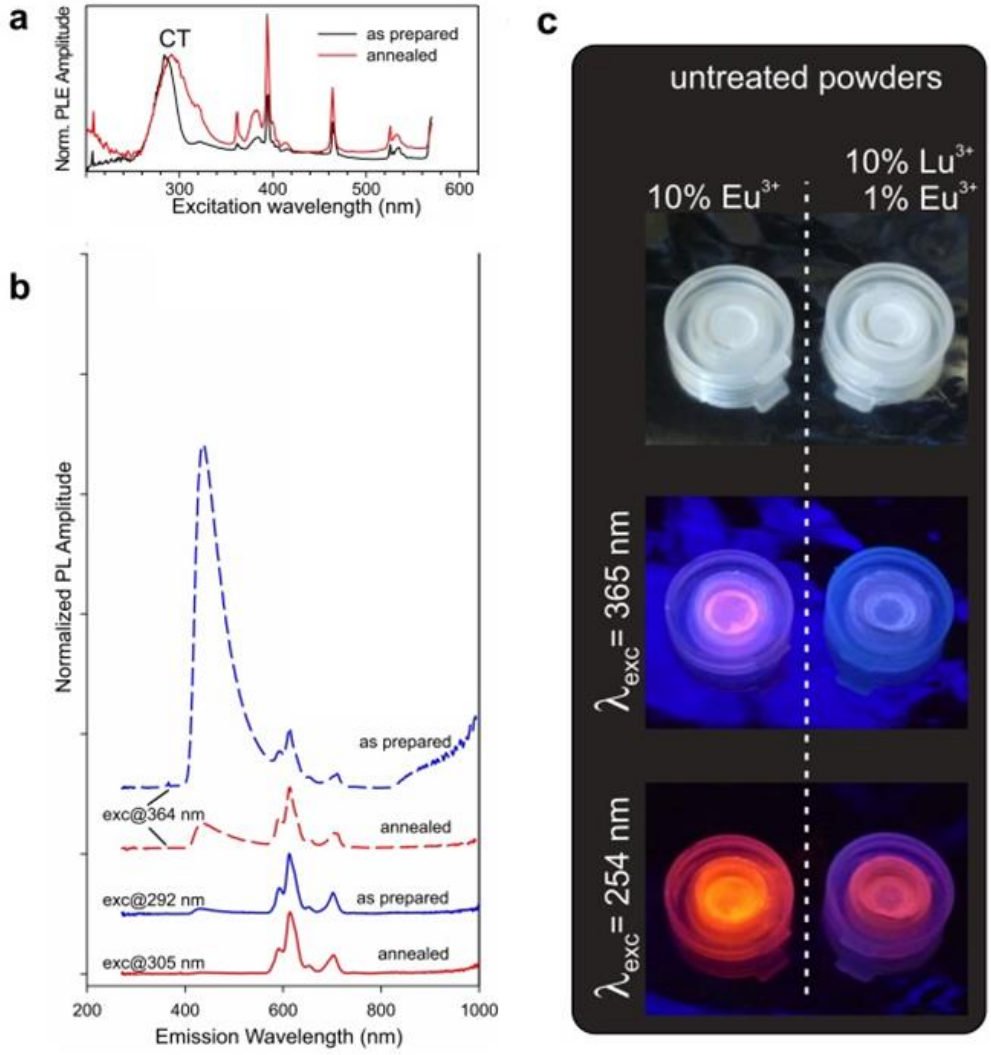

.

Figure 4.10 | (a) PL excitation (PLE) spectra of the600-620 nm emission range of HfO2: Lu/Eu (10, 1 mol %) before (black line) and after (red line) treatment at 1000 °C (spectra normalized to CT maximum). (b) PL emission (PL) spectra of HfO2:Lu/Eu (10, 1 mol %) before (blue lines) and after (red lines) annealing, with λexc =364 nm (dashed lines) and in CT (full lines) at λexc = 292 or 305 nm (all emission spectra normalized at 612 nm, and shifted over the ordinate axis for clarity; spectra are altered in the higher energy region by the use of a cutoff filter at 418 nm). (c) Optical images taken on untreated powders by exciting with the 365 or 254 nm lines of a Wood's lamp.

4.4 REFERENCES

Bai, X. et al. (2012), *One- Step Synthesis and Optical Properties of Benzoate- and Biphenolate-Capped ZrO2 Nanoparticles*. Adv. Funct.Mater. 22, pp. 4275–4283.

Bhagwat, M. et al. (2003), *Refinement Study of Nanocrystalline Copper Doped Zirconia*. Mater. Res. Bull. 38, pp. 1713–1724.

Dobson, K. D. and McQuillan, A. J. (2000), *In Situ Infrared Spectroscopic Analysis of the Adsorption of Aromatic Carboxylic Acids to TiO_2, ZrO_2, Al_2O_3, and Ta_2O_5 from Aqueous Solutions.* Spectrochim. Acta, Part A 56, pp. 557–565.

Fujimori, H. et al. (2001), *Cubic-Tetragonal Phase Change of Yttria-Doped Hafnia Solid Solution: High-Resolution X-Ray Diffraction and Raman Scattering*. Chem. Phys. Lett.346, 217–223.

Gao L. et al. (2012),. *Stabilization of cubic structure in Mn-doped hafnia*. Ceramics International, 38, 3, pp 2305–2311.

Kim, B. K. and Hamaguchi, H. (1997), *Raman spectrum of 18O labelled hafnia*. Mater. Res. Bull. 32, pp. 1367–1370.

Koutstaal, C. A. and Ponec, V. (1993), *FT-IR Study on the Adsorption of Benzoic Acid and its Derivatives on Transition-Metal Oxides*. Appl. Surf. Sci. 70_71 (Part 1), pp. 206–210.

Li, P. et al. (1994), *Effect of dopants on zirconia stabilization; an X-Ray absorption study: I, trivalent dopants*. J. Am. Ceram. Soc. 77, pp. 118–128.

Lu, C.H. et al. (2008),*Cubic phase stabilization in nanoparticles of hafnia-zirconia oxides: particle-size and annealing environment effects*, J. Appl. Phys. 103, pp.124303–124307.

Meng, J. et al. (2010), *Luminescent properties of Eu^{3+} doped HfO_2 powders prepared by combustion*. Key Eng. Mater. 434-435, pp. 805–807.

Niederberger, M. and Pinna, N. (2009), *Metal Oxide Nanoparticles in Organic Solvents*. Springer Verlag, London.

Quintard, P. E. et al. (2002), *Comparative lattice-dynamical study of the raman spectra of monoclinic and tetragonal phases of zirconia and hafnia*. J. Am. Ceram. Soc. 85, 1745–1749.

Zych, E. at al. (2009), *Radioluminescence and photoluminescence of hafnia-based Eu-doped phosphors*. Opt. Mater. 31, pp.1764–1767.

Zych, E. (2002), *Concentration dependence of energy transfer between Eu^{3+} Ions occupying two symmetry sites in Lu_2O_3*. J. Phys. Condens. Matter 14, 5637.

5. Nd^{3+} Doped Nanoparticles for optical bio-imaging

The research on luminescent nanoparticles (LNPs) as new bio-compatible optical probes is an active field of nanomedicine. LNPs can be metallic, semiconductor (QDs), carbon based nanoparticles and rare earth doped nanocrystals. The last category can work in the whole spectral range according to the choice of the rare earth (RE) dopant ion. In this work we focused the attention on Nd^{3+} ion doped infrared (IR) strontium fluoride (SrF_2) NPs.

5.1 Nanoparticles in bio-medicine: Light excited nanoparticles

Nanomedicine has been defined as a scientific field based on the "applications of nanotechnology for treatment, diagnosis, monitoring, and control of biological systems". Actually, the flexibility of nanotechnology allows for the interaction of many technical disciplines, such as physics, chemistry, engineering and computer science, molecular and cell biology, genetics, or neuroscience. Nanoscale entities for nanomedicine are normally defined as being less than 100 nm in length (Fig. 5.1), a size similar to proteins, some viruses, DNA, and much smaller than cells and bacterias. Moreover this range size matches the dimension of the class of nanoparticles exhibiting tunable optical properties.

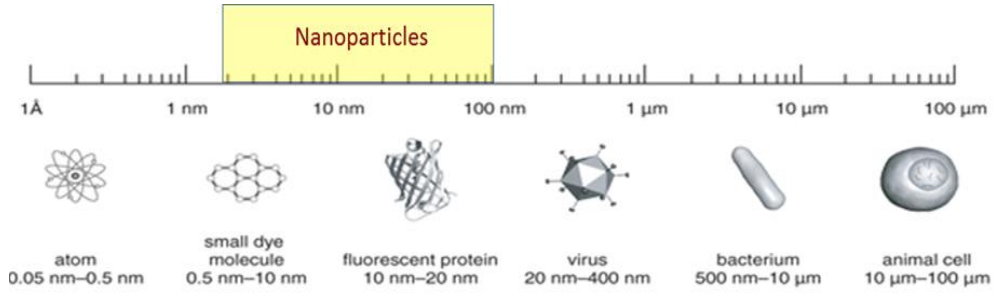

Figure 5.1 | Representation of nanometric unity in life science and biology. The range size of nanoparticles to be used in nanomedicine is pictured.

The use of materials in nanoscale provides freedom to modify fundamental properties such as solubility, diffusivity, blood circulation half-life, drug release characteristics, and immunogenicity. An increasing number of nanoparticle-based therapeutic and diagnostic agents have been developed for the treatment of diabetes, pain, asthma, allergy, and infections. For instance, among the different nanomedical applications, nanoparticle-based drug delivery has been most extensively explored. Many advantages of nanoparticle-based drug delivery have been recognized: It improves the solubility of poorly water-soluble drugs, prolongs the half-life of drug systemic circulation by reducing immunogenicity, releases drugs at a sustained rate, thus lowering the frequency of administration and suppressing drug resistance. (L. Zhang, 2008). At the same time, strong efforts have been put in the development of a novel class of materials, where self-assembling particles and nanomaterial improve the mechanical properties and the biocompatibility of biomaterials for medical implants. Examples include nanocomposite materials used as dental fillers for implant coatings and bone substitutes. (G. Bao, 2013).

In the last 20 years, the scientific community has carried out lots of efforts in the field of the nanotechnology applied to medicine in order to

improve the detection and diagnosis of cancer, and the monitoring of cancer therapies. The “cancer nanotechnology” focuses on the design, synthesis, characterization, and application of nanometer-size particles as biosensors, drug delivery vehicles, and biomarkers, by linking them with tumor targeting ligands such as monoclonal antibodies, peptides, or small molecules. Metal, semiconductor, and insulating inorganic systems, as well as polymeric compounds have been considered (B. Gang, 2013; I. Willner, 2010; I. Brigger, 2002).

Thanks to the progresses in nanocrystal synthesis, mostly inorganic nanoparticles can be generated with a great deal of control over size, shape, and composition, as well as physical properties to be applied in the field of cancer therapies. The control of the NPs characteristics, together with their versatility, influence the behaviour of the nanoprobes for in vivo methodologies, such as imaging and diagnostics of many diseases where early diagnosis is key to obtaining maximum treatment effects or the opportunity to intervene as early as possible (S. Krol, 2013). The unique physical and optical characteristics of nanomaterials have motivated efforts to investigate their use as sensitizers in the photodynamic, radio and photothermal cancer therapies (N. Idris, 2012 and P. Juzenas, 2008) as well as in drug delivery applications (D.J. Naczynski, 2014). Properly designed nanostructures are used as heat generators for hyperthermia treatments, aimed to damage tumoral cells by the locally induced temperature increase, which can also be monitored by changes of the optical features of selected nanoparticles (D. Jaque, 2012).

Another example of an important area of medicine in which nanometer sized particles can be applied for benefit is early diagnosis (X. Yi, 2014).

Nanoparticles help to identify abnormalities such as fragments of cancerous cells that cannot be detected with traditional diagnostics, such as X-ray imaging, blood cell counting, plasma or anatomic imaging by computer tomography (CT) or magnetic resonance imaging (MRI) (M E. Labatto, 2011). Recently, much attention has been paid to the development of luminescent nanoparticles (LNPs) for *in vitro* and *in vivo* bioimaging applications. The optimization of the synthesis procedures has made possible the production of LNPs with specifically engineered and tailored properties. Indeed, LNPs display a much higher photostability than the luminescent organic probes that have been traditionally used for bioimaging. This is of great help in the case of certain *in vitro* studies in which the UV radiation was found to induce cytotoxic effects into living cells and tissues (Y. Matsumura, 2004). In turn, for *in vivo* applications, the achievement of large penetration depths into tissues implies the use of luminescent probes working in the infrared biological windows (D.J. Naczynski, 2013). Thus, the excitation and emission operating spectral ranges of many LNPs should be pre-designed during synthesis procedure. While for semiconductor quantum dots (QDs) the spectral working range is determined by both the semiconductor host matrix and its size, for RE doped nanoparticles the spectral working range can be controlled by an adequate selection of the RE dopant ions. In addition, chemical methods have evolved such that tuning of the surface of LNPs is now possible. These surface treatments could grant the LNP with long term colloidal stability in biological fluids, thus allowing for their direct injection in the blood stream for *in vivo* bioimaging experiments. As a result of all these and many other key advancements in the field, LNPs are currently being considered for real *in vivo* tumor detection at early stages, which would lead to a substantial increment in the treatment efficacy.

5.2 *IN VIVO* FLUORESCENCE IMAGING BY RARE EARTH ION BASED NANOPARTICLES

Fluorescence imaging is a high sensitive non-invasive tool playing an important role in biomedicine due to the increasing availability of fluorescent proteins, dyes, and probes that enable for non-invasive study of a large number of cellular processes. In parallel, there is an increasing list of fluorescent imaging techniques that offer microscopic resolutions and video-rate scans, or methods that operate at resolutions beyond the diffraction limit, yielding unprecedented insights into biology (V. Ntziachristos, 2006). Nevertheless, more effort must be employed in enhancing the performances - in term of resolution range, contrast, and penetration depth in the tissue - of the imaging methods for real *in vivo* tumor detection at early stages. *In vivo* optical imaging suffers from several intrinsic effects caused by the interaction of light with biological tissues. The first is the light attenuation (extinction) in living specimens, which is caused by the interplay between the light scattering due to the inherent tissue inhomogeneity and the optical absorption of the different biological media (water, blood, hemoglobin, melanin and lipids) as reported in Fig. 5.2a-c (A. Smith, 2009). Indeed, the extinction coefficient of tissues and living specimens ($\alpha_{ext.}$) is usually written as the sum of the scattering coefficient ($\alpha_{sct.}$) and the absorption coefficient ($\alpha_{abs.}$), therefore $\alpha_{ext.} = \alpha_{sct.} + \alpha_{abs.}$. During *in vivo* fluorescence imaging experiments, a reduced intra-body penetration length of both excitation and fluorescence radiations takes place (Fig. 5.2c-d). This, in turns, inhibits imaging of deep tissues, for instance, intra-body (non-superficial) tumors. Furthermore, autofluorescence, i.e. fluorescence generated by tissues and intra-body components when excited in the UV–visible range, can occur. This autofluorescence can overlap with that of the fluorescent label and then partially or totally masking the label fluorescence signal.

5.2.1 RARE EARTH ION BASED NANOPARTICLES WORKING IN THE BIOLOGICAL WINDOWS

Biological optical imaging greatly relies upon the use of sensitive and stable optical labels. So far, organic dyes, quantum dots, and metal nanoparticles are the most commonly used optical labels, but they also come with essential limitations. Organic dyes suffer from a short observation time, partly due to photobleaching, poor stability under physiological conditions, and limited Stokes shift (T. Maldiney, 2012). Typical fluorescence imaging techniques rely on fluorophore labels that are excited with UV light, where the cited well-known drawbacks occur (Fig. 5.2d). (F. Vetrone, 2010). Although QDs display good photostability, size-dependent emissions, and high quantum yield, they still require constant UV-Visible excitation, which is responsible for undesirable autofluorescence and elevated background signal that reduce the sensibility of the assay (R. Naccache, 2012). So the design of probes which absorb and emit in an appropriate spectral range aims to increase the optical contrast, to a greater light penetration depths, and to a minimal autofluorescence contribution and reduced scattering.

It is in this regard that luminescent lanthanide (Ln^{3+})-doped nanoparticles (LNPs) have been proposed for imaging, diagnostics and therapeutics far into the subcutaneous regions of the body. Especially, one of the most suitable solutions is the use of LNPs working in the so-called biological-windows (BWs), spectral regions in which tissues are partially transparent (Fig. 5.2 and 5.3a). BWs are spectrally allocated in the infrared (>750 nm) since the use of long wavelengths reduces tissue-induced light scattering.

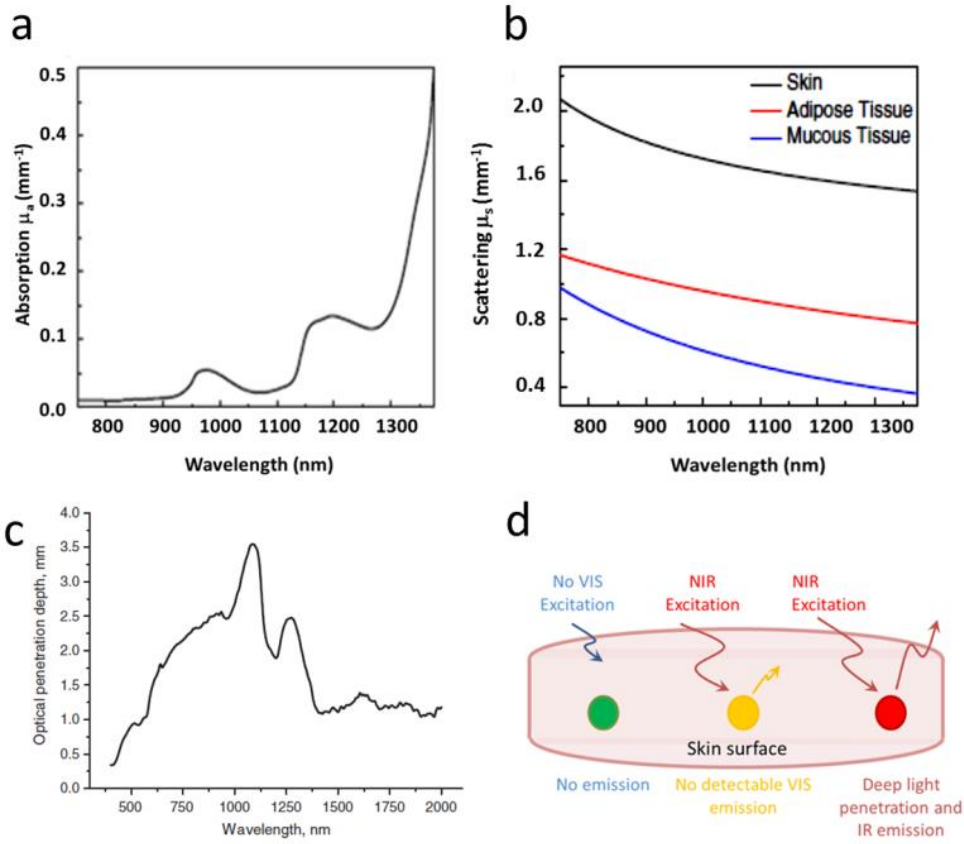

Figure 5.2 | (a) Absorption coefficient of water in the NIR region, from 800 n to 1300 nm. (b) Extinction scattering for skin, adipose tissue and mucous tissue. Notice that all show a decreased scattering with increasing wavelength. (c) Optical penetration of human skin in the wavelength range from 400 to 2000 nm (a, b printed from K. Welsher, 2011. C (printed from A N Bashkatov, 2005). (d) Sketch of the attenuation of both excitation and emission beams for different excitation energy ranges.

There are three main BWs. i) The first (I-BW) extending from 750 to 950 nm, which is limited by the visible absorption of hemoglobin and the 980 nm absorption band of water. ii) The second (II-BW) extending from 1000 up to 1450 nm and limited by the 980 and 1450 nm absorption bands of water. iii) The third (III-BW) that extends from 1500 up to 1700 nm, limited by two water

absorption bands. A given LNP is said to work within BWs when both the excitation and emission radiations lie within any of these three spectral ranges. This ensures that both excitation and fluorescence signals are weakly attenuated, resulting in a larger optical penetration and, thus, allowing for deeper imaging.

For instance, significant improvements have been achieved in small animal whole body imaging by using upconverting $NaYF_4$:Yb, Er nanoparticles (UPCNPs) (D. J. Naczynski, 2013) Recent developments of down-converting lanthanide inorganic fluoride nanoparticles, like core–shell $NaGdF_4$:Nd(3%)@$NaGdF_4$ nanocrystals, have also demonstrated their feasibility to be used as probes for in vivo small animal imaging (G. Chen, 2012). A smart alternative to avoid autofluorescence is the use of LNP showing what is called persistent luminescence, i.e. light emission persisting for a long time after the excitation has ended. The most efficient materials possessing persistent luminescence are Eu^{2+}/Ln^{3+} or $Eu^{2+}/Mn^{2+}/Ln^{3+}$ (Ln = Dy, Nd, Tm, Pr) co-doped aluminates, silicates and nitride-silicates (T. Maldiney, 2011). In summary, high contrast, minimized autofluorescence background IR *in vivo* imaging requires the use of LNPs that specifically show intense fluorescence in the 1000-1400 nm region following optical excitation in any of the BWs (D.J. Naczynski, 2013). This condition has been demonstrated to be efficiently satisfied by a limited number of LNPs, including single walled carbon nanotubes (SWCNTs) and Ag_2S quantum dots (Ag_2S-QDs). Indeed, recent studies have shown excellent “in vivo” mice biodistribution fluorescence images by using carbon nanotubes or AgS_2 quantum dots as nanoprobes (K. Teker, 2005 and H. Guosong, 2012). These nanoprobes emit in the II-BW by means of one-photon excitation within the I-

BW but their weak NIR absorption and low fluorescence quantum yields still limit their applicability.

5.2.2 Nd^{3+} ION DOPED NANOPARTICLES

RE nanomaterials are also capable of generating emissions in 1000 – 2300 nm range with large Stokes shifts following excitation with low power-continuous-wave sources in the NIR first tissue-transparent window. They offer outstanding properties such as large fluorescence quantum yields, absence of induced fluorescence deterioration, long term chemical and physical stability and low toxicity. In particular, Nd^{3+} ion doped nanoparticles (Nd:NPs) are quite interesting as they possess close-to-unity luminescence quantum yields and well-defined emission bands, matching both the I and II-BWs, that can be efficiently excited by 808 nm radiation (see the case of SrF_2 Nd doped in Fig. 5.3b). The emission spectrum of neodymium (Nd^{3+}) doped NPs after 808 nm optical excitation possesses three emission bands centered at around 900, 1060 and 1340 nm and corresponding to the $^4F_{3/2} \rightarrow {}^4I_{9/2}$, $^4F_{3/2} \rightarrow {}^4I_{11/2}$ and $^4F_{3/2} \rightarrow {}^4I_{13/2}$, 4f-4f transitions of the Nd^{3+} ions, respectively (Fig. 5.3b and Diecke diagram in Fig. 5.4). The optical properties of Nd^{3+} in various materials have been largely studied, because neodymium is the most common activator ion in laser crystals, owing to its intense luminescence, and it is, therefore, of considerable interest in quantum electronics and its applications (F. Ramos-Lara, 2006). Recently, Nd^{3+} ion doped fluoride nanocrystals have been used in nanomedicine, since the dopant ion optical response in these host revealed features suitable even for

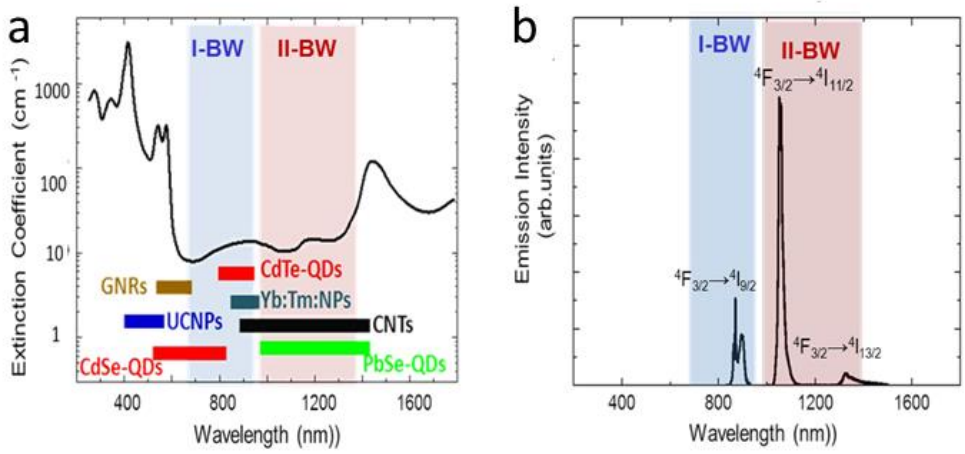

Figure 5.3 | (a) Extinction coefficient of human blood (oxygenated) in the 300–1700 nm spectral range. The spectral ranges of both first (blue colour) and second (pink colour) biological windows are schematically indicated. The emission spectral ranges of the different LNPs previously used for fluorescent bioimaging are also included. (b) Emission spectrum of a colloidal solution of Nd^{3+}:SrF_2 NPs as obtained after 808 nm optical excitation. The three emission bands are labelled according to the excited and ground states of Nd^{3+} ion.

the cancer diagnosis and therapy. The hypersensitive fluorescence lines at around 900 nm correspond to the low energy emissions within the $^4F_{3/2} \rightarrow {}^4I_{9/2}$ transition of Nd^{3+} and show a remarkable thermal sensitivity. Indeed, Nd^{3+} ion doped crystalline host, like LaF_3 NPs, have been already used as sub-tissue thermal sensors (U. Rocha, 2013). The same band of Nd^{3+} ion lying within the I-BW have proposed for deep tissue bioimaging, together with the one at lower energy related to $^4F_{3/2} \rightarrow {}^4I_{11/2}$ Nd^{3+} transition (U. Rocha, 2014). At the same time, the 1300 nm fluorescence band of neodymium doped NPs has not been largely used for in vivo imaging, due to its lower intensity when compared to the 900 and 1060 nm bands. Indeed, in most of the neodymium doped crystals the fluorescence branching ratio of the $^4F_{3/2}\rightarrow{}^4I_{13/2}$ transition is three times lower than that of the $^4F_{3/2}\rightarrow{}^4I_{9/2}$ or of $^4F_{3/2}\rightarrow{}^4I_{11/2}$transitions. As a matter of fact, only

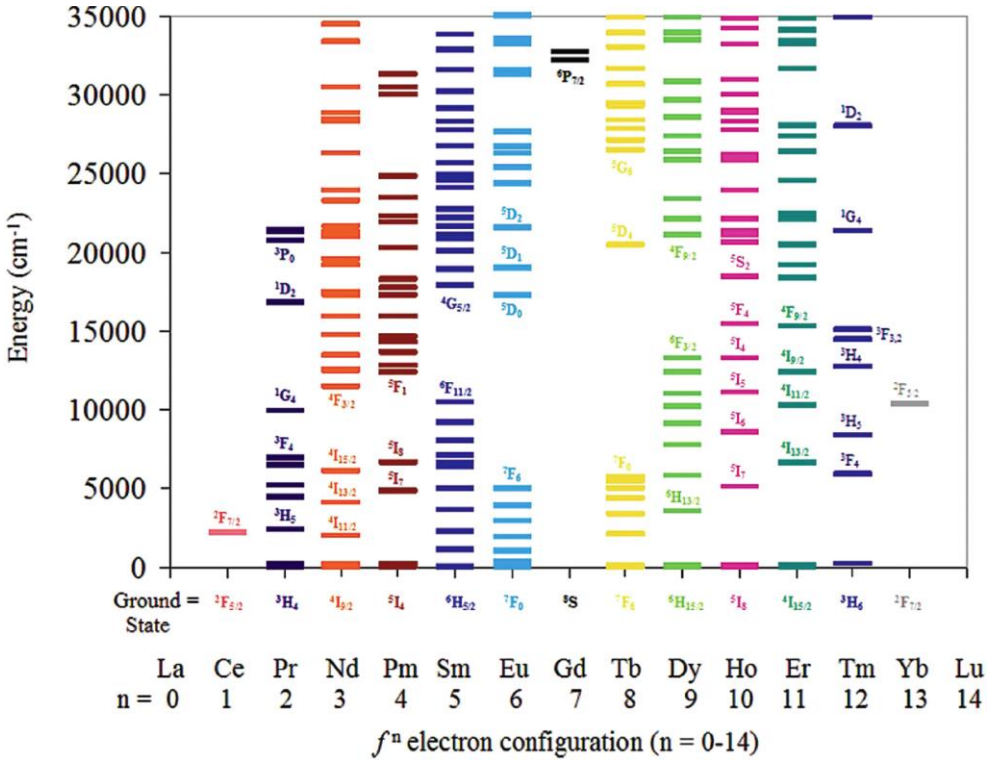

Figure 5.4 A summary of electronic excited-state energy levels for Ln3+ ions. Reprinted with permission from ref (E. Moore, 2009)

15% of the radiative de-excitations generated from the $^4F_{3/2}$ metastable state of the neodymium ions is produced through the $^4F_{3/2} \rightarrow {}^4I_{13/2}$ fluorescence channel.

This ensures that using the 900 or 1060 nm emission bands allows obtaining brighter images than those obtained by exploiting the 1300 nm emission. However, as we will see below, this emission band is particularly interesting in order to avoid the fluorescence given by the food pellets usually given to feed mice. Thus, the achievement of 1300 nm fluorescence bright enough for in vivo fluorescence imaging becomes of relevance but it would require the development of a host matrix that provides large radiative probabilities for neodymium ions. Otherwise, the combination of moderate to low radiative

probabilities and the reduced branching ratio of the $^4F_{3/2} \rightarrow {}^4I_{13/2}$ transition would lead to a weak 1300 nm fluorescence signal. To summarize, Nd^{3+} ion doped nanocrystals provide three main emission bands that make Nd doped nanoparticles as promising multifunctional nano-agents, due to its capability of simultaneous imaging, thermal sensing and heating under infrared laser light excitation in animal models.

5.3 Nd^{3+} ion doped SrF_2 NPs

The incorporation of trivalent lanthanide ions into divalent fluorides (such as CaF_2 and SrF_2) seems to be particularly interesting in order to get bright emitting Nd based nanoparticles (J. Payne, 1991). Due to the needed local charge compensation, strong non-inversion crystal field environments around Nd^{3+} ions are expected to occur, giving rise to intense dipole forced transitions. Thus, if this ion is incorporated in an appropriate host matrix, even the $^4F_{3/2} \rightarrow {}^4I_{13/2}$ Nd^{3+} ion transition would provide a bright 1300 nm luminescence and then it could be used for in vivo imaging, leading to a high resolved deep tissue imaging. In this work we have synthetized and studied Nd^{3+}:SrF_2 nanoparticles, in term of the evaluation of the suitability of these novel NPs for *in vivo* fluorescence imaging, comparing the results with the already explored Nd^{3+}:LaF_3 NPs (U. Rocha, 2014).

5.3.1 Synthesis of SrF_2 nanoparticles

The preparation of the lanthanide doped SrF_2 NPs has been previously described by M. Pedroni et al. (M. Pedroni, 2013). Briefly, stoichiometric amounts of the lanthanide chlorides and strontium chlorides were dissolved in

7 ml of de-ionized water (total metal amount of 3.5 mmol). To this solution, 20 ml of a 1 M solution of potassium citrate were added dropwise under vigorous stirring for a few minutes. Then, an amount of 8.75 mmol of ammonium fluoride was added to the previous solution. The resultant clear solution was heated in a 50 ml stainless steel Teflon lined digestion pressure vessel at 190 °C for 6 h. After washing with acetone and drying at room temperature, the obtained NPs were directly dispersed in water.

5.3.2 Characterization of SrF_2 nanoparticles

The Zeta-potential value for the nanoparticles was measured using a Malvern Zetasizer Nano ZS90 operating with a He-Ne laser at 633 nm. Measurements were carried out in water colloidal dispersions of SrF_2 NPs with a 25 g/L concentration. A Zeta-potential value of -24 ± 9 mV was obtained. Particles in aqueous systems may have charged surfaces depending on their chemical reactivity towards the solvent. The surface charge of many nanomaterials is due to acid-base reactions at the surface (i.e., gain or loss of protons or hydroxide ions). At the surface, isomorphic replacements within the solid lattice structure, or adsorption of charged species on the particle surface, may also occur. The surface chemistry of nanomaterials is often engineered by coating with organic surfactants responsible for the surface charge. In the present experiment, citrate ions are coordinated to the surface of the strontium fluoride nanoparticles, creating a negative surface charge that stabilizes the particles by preventing, through electrostatic repulsion, coalescence and agglomeration.

X-Ray powder diffraction (XRPD) patterns were measured with a powder diffractometer (Thermo, ARL XTRA), operating in Bragg-Brentano geometry, equipped with a Cu-anode X-ray source (Kα=1.5418) and using a Peltier Si(Li) cooled solid state detector. The patterns were collected at a scan rate of 0.04 °/min the 15°-90° 2θ range. The powdered samples were finely ground in a mortar and then deposited in a low-background sample stage for the measurements. A structural analysis revealed that the present SrF_2 nanoparticles are single phase with a cubic fluorite structure. The calculated lattice parameter for the cubic cell is of 5.774(1) Å, slightly higher than that found for Tm^{3+},Yb^{3+} doped SrF_2 nanoparticles (M. Pedroni, 2013). The size and morphology of the Neodymium doped SrF_2 nanoparticles were determined by using a Transmission Electron Microscope (TEM, JEOL JEM1010) working at 80 kV of accelerating voltage. The histograms to obtain the size dispersion were made from the analysis of several images by using the Mac Biophotonics-Image J software.

Fluorescence measurements were carried out in a conventional confocal fluorescence microscope. A fibre coupled laser diode (Lumics LU0808M100) operating at 808 nm (peak of the $^4I_{9/2} \rightarrow {}^4F_{5/2}$ absorption band of Nd^{3+} ions) was used as excitation beam. The excitation beam was focused into the Nd:SrF_2 Nps/ water solutions by using a 50× infrared microscope objective (0.55 NA). The subsequent fluorescence was collected by the same objective and spectrally analysed by a nitrogen cooled AsGaIn array connected to a high resolution monochromator (IR550M). For time-resolved measurements, a multichannel scaler ORTEC 9353 Time Digitizer/MCS has been used in photon counting acquisition mode, with a time resolution better than 100 ns.

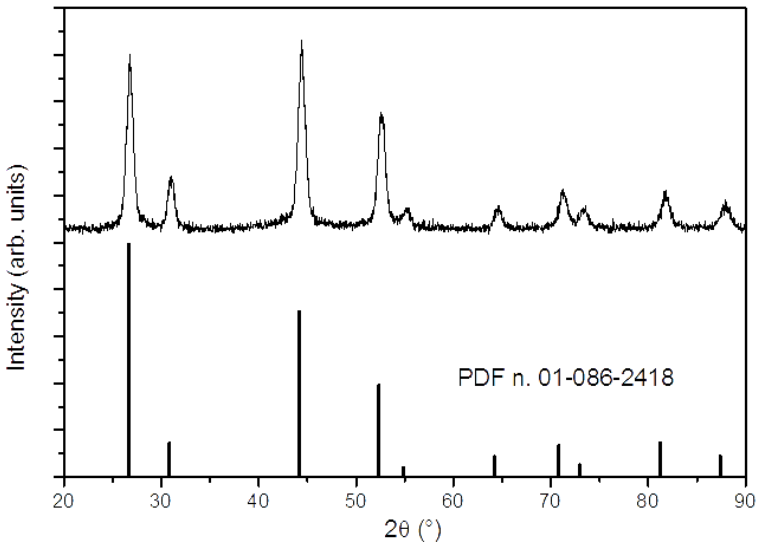

Figure 5.5 | X-ray powder diffraction powder pattern for cubic SrF_2 (PDF card n. 01-086-2418).

Fluorescence images were performed by means of a confocal fluorescence microscope equipped with an AsGaIn camera with enhanced sensitivity in the 850-1500 nm spectral range.

5.3.3 FOOD AUTOFLUORESCENCE SPECTRUM ACQUISITION

Fig. 5.6 (Top panel) includes the fluorescence images of a food pellet under 808 nm excitation, as obtained by using a set of different long-pass filters with cut-off wavelengths ranging from 900 up to 1400 nm. The wavelength dependence of the food emission was obtained from the analysis of these images. For this purpose, the total (integrated) emission intensity generated by the food pellet was calculated from each fluorescence image (each filter). This integrated intensity is denoted as I_λ^{int} where λ is the cut-off wavelength of the

long-pass filter used for image acquisition. Long-pass filters with cut-off wavelengths increasing in 50 nm steps have been used. Subtracting the integrated fluorescence intensities obtained by two consecutive long-pass filters (I_{λ}^{int} - $I_{\lambda+50nm}^{int}$) the difference gives the intensity generated by the food pellet in the spectral range from λ up to λ+50 nm. This could be, in a first order approximation, identified as the emission intensity at a wavelength of λ+25 nm; that is the medium value between λ and λ+50 nm. This allowed to obtain the food emission spectrum given in Fig. 5.6(Bottom panel).

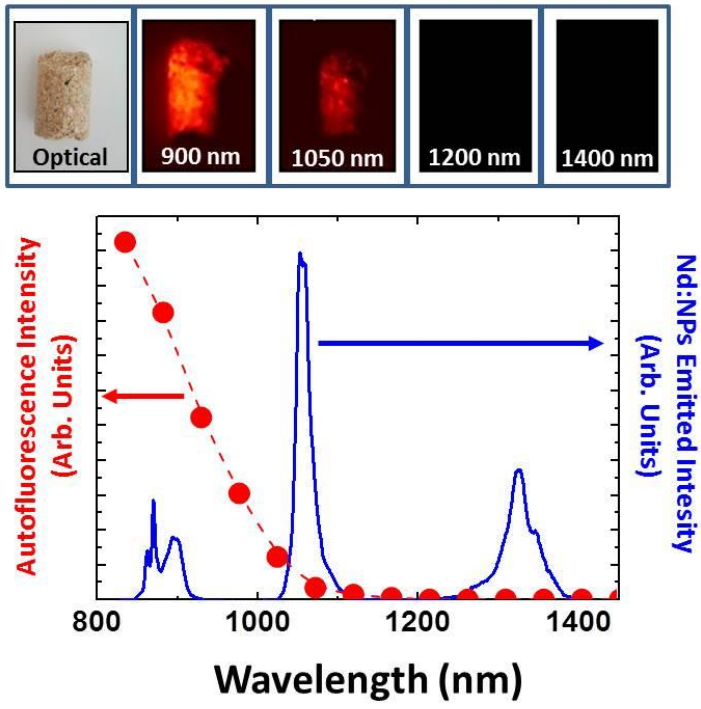

Figure 5.6 | (Top panel) Optical image of a mouse food pellet and fluorescence images of the same pellet as obtained using different long-pass filters when excited with a 808 nm laser. (Bottom panel) Wavelength dependence of the infrared autofluorescence intensity generated by a mouse food pellet. Dots are experimental data and dashed line is a guide for the eyes.

5.3.4 TOXICITY STUDIES

MTT colorimetric assay was performed to evaluate cell viability and proliferation. Briefly, the MTT (3-(4,5-dimethylthiazol-2-yl)-2,5-diphenyltetrazolium bromide) is a yellow, water soluble, tetrazolium salt. Viable and metabolically active cells are able to convert this yellow dye into a water-insoluble dark blue formazan crystals (T. Mosmann, 1983). Formazan crystals within cells are then dissolved in an organic solvent, such as dimethylsulfoxide (DMSO), released from cells and quantified by measuring the absorbance of the solution at 540 nm; the absorbance value is related to the number of living cells. To determine nanoparticles cytotoxicity on cells, immortal human epithelial cells (HeLa cells) were placed in a 24 well plate at 37 °C in a 5% CO_2 atmosphere. After 48h of culture, culture medium was replaced with the fresh medium containing Nd:SrF_2 nanoparticles at three different concentrations (25, 50 and 100 µg/ml). HeLa cells were incubated with medium containing nanoparticles for different timing, from 2 up to 48 hours. After the selected incubation timing, culture medium containing nanoparticles was removed and fresh completed medium was added, in order to stop Nd:SrF_2 uptake from HeLa cells. Cells were maintained in culture for 24 hours, and subsequently 5% (w/v) of MTT dye solution (Sigma) was added to each well. After 2-3 h of incubation at 37 °C and 5% CO_2, the medium containing MTT was removed and formazan crystals were solubilized with 0.5 ml/well of DMSO (Merck) and the solution was vigorously mixed to dissolve the reacted dye. The absorbance at 540 nm was read using a microplate reader (Espectra Fluor 4, Tecan). The percentage of viability of HeLa cells incubated with NPs as compared to control cells (i.e. without incubation with nanoparticles) was calculated as [A] test/[A] control x 100, where [A] test

is the absorbance of the tested sample and [A] control is the absorbance of the control sample.

5.3.5 In vitro imaging

Fluorescence images of HeLa cells incubated with Nd:SrF_2 NPs have been obtained with an epi-fluorescence microscope equipped with an AsGaIn camera with enhanced sensitivity in the 850-1500 nm spectral range. Excitation was performed by using an 808 nm fibre coupled diode. Excitation radiation was blocked by using a long-pass filter with a cut-off wavelength of 850 nm.

5.3.6 In vivo experiments

Fluorescence in vivo imaging was performed by using a peltier cooled AsGaIn camera (XEVA 1.7, Xenics Corp) coupled to a C-Mount objective. Laser excitation was achieved by using a fibre coupled laser diode (LIMO GmbH). A long-pass filter blocking all wavelengths below 850 nm (FEL1000 from Thorlabs GmbH) was continuously attached to the C-Mount objective in order to remove any contribution from the 808 nm (excitation) laser scattered radiation. The C-Mount objective was attached to a filter wheel equipped with six long pass filters with cut-off wavelengths ranging from 900 up to 1400 nm. The excitation intensity (808 nm) was always kept below 1 W/cm^2, which is needed for safe animal measurements. For all the in vivo experiments, 50 µl of a solution of Nd:SrF_2 NPs dispersed in Phosphate Buffered Saline (PBS, at a concentration of 0.3 % in mass) were intravenously injected through the retro-orbital sinus into 9-week-old female CD1 mice. For the in vivo imaging, the previously shaved mice were anesthetized with 2% isoflurane. For monitoring the weight evolution, the animals were weighted daily at the same time, during 30 days after the inoculation. The average weight and the standard deviation were

calculated and represented for each time point in order to establish the comparisons between NPs-inoculated mice and their corresponding controls (only inoculated with PBS), including n = 3 animals per group. The obtained data will be discussed below.

Mice were housed and maintained under specific pathogen-free conditions and all the experimental procedures with animals were carried out in compliance with the guidelines in RD 53/2013 (Spain) and were approved by the Ethics Committee of the Universidad Autonoma of Madrid (CEIT).

5.4 Nd^{3+} IN SrF_2 HOST -SPECTROSCOPY

A systematic investigation of morphological and structural and optical properties of the synthetized SrF_2:Nd nanoparticles has been carried out with the main aim of solving the problem of food fluorescence. In particular, an aqueous colloidal solution of Nd:SrF_2 NPs (2.5 % wt in distilled water) was investigated. Fig. 5.7a-b show the results obtained from TEM measurements, revealing that the NPs are monodispersed with a Gaussian distribution characterized by an average diameter of 10 nm and a Full Width at Half Maximum (FWHM) of about 3 nm. The as-synthesized Nd:SrF_2 NPs were easily dispersed in both water and phosphate saline buffer solution (PBS), showing an outstanding colloidal stability without any evidence of precipitation or agglomeration during a period of several months (Fig. 5.7c).

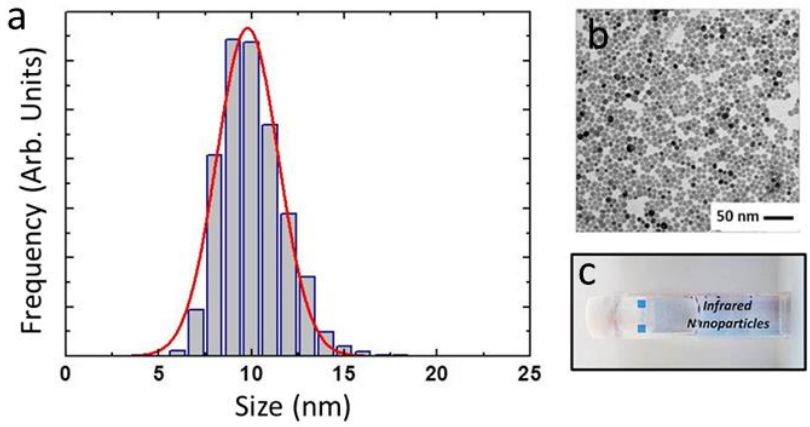

Figure 5.7 | (a) Size distribution of the Nd:SrF_2 NPs used in this work as obtained from the statistical analysis of the TEM image given in (b). (c) Digital picture of an aqueous colloidal solution of Nd:SrF_2 NPs.

Fig. 5.8 shows the absorption spectrum of obtained NPs. The emission spectrum of neodymium doped SrF_2 NPs (after 808 nm optical excitation) possesses three emission bands centered at around 900, 1060 and 1340 nm and corresponding to the $^4F_{3/2} \rightarrow {}^4I_{9/2}$, $^4F_{3/2} \rightarrow {}^4I_{11/2}$ and $^4F_{3/2} \rightarrow {}^4I_{13/2}$, 4f-4f transitions of the Nd^{3+} ions, respectively. This spectrum is that given in Fig. 5.6 (Bottom panel). Due to the requirement of local charge compensation, strong non-inversion crystal field environments around the Nd^{3+} ions are expected to occur in SrF_2. Thus, neodymium doped SrF_2 RENPs are expected to provide a brighter 1300 nm luminescence when compared to other previously studied neodymium doped nanoparticles.

According to this, we decided to analyze the $^4F_{3/2}$-$^4I_{13/2}$ ion transition(emission at around 1340 nm) in order to perform the IR in vivo fluorescence imaging , avoiding from the food emission.

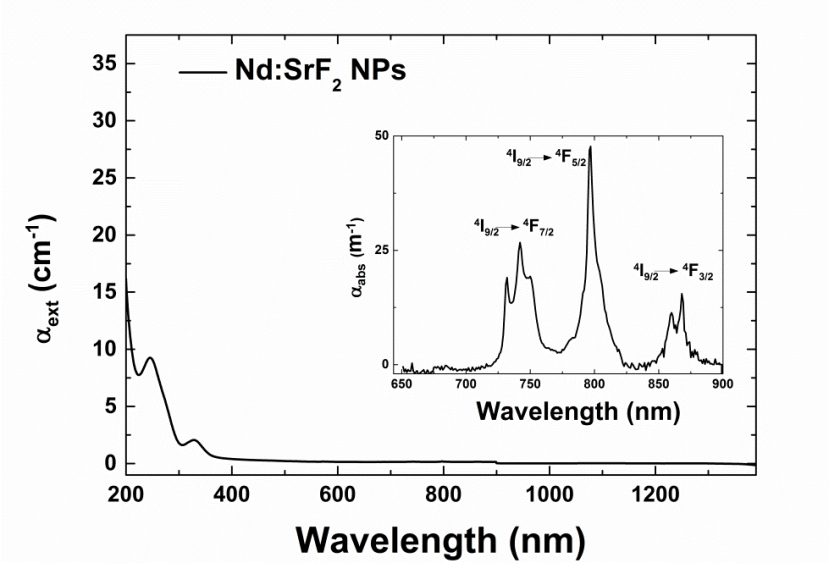

Figure 5.8 | Room temperature extinction spectrum (200-1400 nm spectral range) as obtained from a colloidal water solution of Nd:SrF2 nanoparticles. The nanoparticle concentration was set to 25 mg/mL. Inset shows the absorption spectrum as obtained by subtracting the scattering background to the extinction coefficient.

Fig. 5.9a displays the referred $^4F_{3/2} \rightarrow {}^4I_{13/2}$ (1340 nm) emission spectrum for an aqueous solution of Nd:SrF_2 NPs (2.5 % wt in distilled water, 3 at % Neodymium concentration in the SrF_2 host nanocrystals), after exciting the solution with an 808 nm laser diode. For the sake of comparison, we have also included the emission spectrum obtained under identical experimental conditions from an aqueous solution of Nd:LaF_3 (i.e. 2.5 % wt in distilled water) NPs. The neodymium concentration in these NPs (having an average size of 15 nm) was 5 at. %. In order to provide a proper comparison of the Nd^{3+} intensity emission in two different matrices, the emission spectra given in Fig. 5.9a have been normalized to the total number of Nd^{3+} ions present in each solution. The superior performance (in terms of fluorescence intensity) of the Nd:SrF_2 NPs over the Nd:LaF_3 NPs (in the 1300-1500 nm range) is evident. SrF_2: the

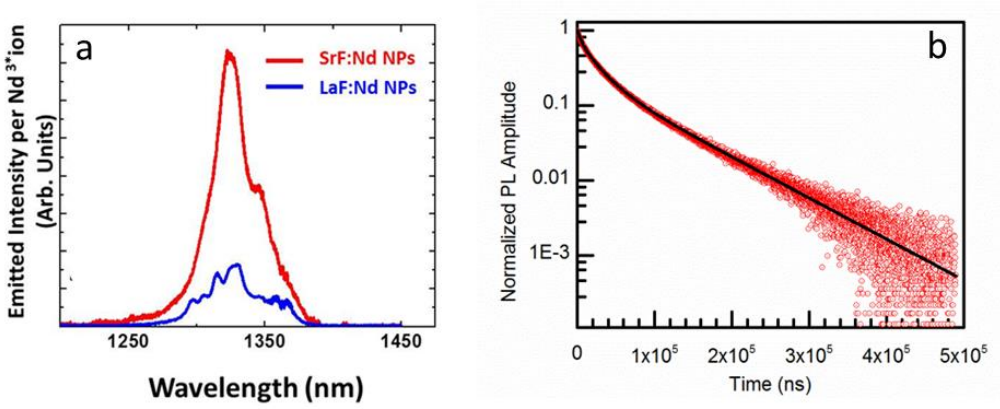

Figure 5.9 | (a) Infrared emission spectrum as obtained from an aqueous colloidal solution of Nd:SrF2 NPs (see inset). For the sake of comparison, we also include the emission spectrum obtained, under exactly the same experimental conditions, for a colloidal suspension of Nd:LaF_3 NPs. In both cases the fluorescence intensity has been corrected by the number of Nd^{3+} ions in each system. (b) Time resolved NP photoluminescence at 1330 nm recorded under pulsed excitation at 355 nm (pulse width 10 ns). PL decay does not behave a single exponential function, thus demonstrating the coexistence of different emitting centers within the particles. A triple exponential function (with characteristic lifetimes of t_1 =79 µs, t_2= 58 µs and t_3= 23 µs with relative weight of 61.5%, 4.4% and 34.1%) is used to fit the PL decay.

luminescence is almost 10 times enhanced in the SrF_2 NPs. This superior performance could be due to a perturbed local crystalline field. Although the local site symmetry at the cationic sites is highly symmetric in the SrF_2 lattice (O_h), due to the necessity of charge compensation (Nd^{3+} replaces Sr^{2+}), non-centrosymmetric crystal field components around the neodymium ions are expected to be present, giving rise to intense dipole forced transitions and, hence, to bright fluorescence.

Time resolved photoluminescence (PL) measurements of the $^3F_{3/2}$-$^4I_{13/2}$ transition are given in Fig. 5.9b. The obtained data point out the existence of different luminescence Nd^{3+} centers (local environments) within the SrF_2:Nd^{3+} nanocrystals, whose emission properties depend on the local crystalline field symmetry. In order to get additional information to understand the excellent

fluorescence performance of Nd:SrF_2, we have estimated their average fluorescence Quantum Yield (QY) based on that previously reported (0.55, as obtained by thermal lens spectroscopy) for the Nd:LaF_3 NPs (A. Gautama, 2013). For this purpose we carefully measured the extinction spectra of our aqueous solution of Nd:SrF_2 and Nd:LaF_3 NPs. The extinction spectrum of the Nd:SrF_2/water solution is shown in Fig. 5.8. The solution showed an almost negligible extinction coefficient in a wide spectral range (300-1300 nm) that can be explained in terms of the large band-gap of the SrF_2 host together with a low scattering coefficient of the Nd:SrF_2 NPs and the low concentration of Nd. The inset of in Fig. 5.8 shows the absorption spectrum (obtained by subtracting the scattering background to the extinction coefficient) in the 650-900 nm spectral range, in which the optical transitions corresponding to Nd^{3+} ions are observed and properly labelled according to the involved transitions of this ion. We also obtained the same absorption spectrum but for the Nd:LaF_3 nanoparticles (not given here for the sake of simplicity). Once the absorption coefficients are determined for the Nd^{3+}ions (at the excitation wavelength of 808 nm) for both NPs, the QY of the Nd:SrF_2 NPs can be directly obtained from the comparative emission spectra given in Fig. 5.9a. In such a way we were able to estimate a fluorescence QY of 0.9 ±0.1 for our Nd:SrF_2 NPs. In conclusion, the superior fluorescent properties (in terms of 1340 emitted intensity) of the Nd:SrF_2 NPs have been demonstrated. Thus their potential application for high-contrast in vivo imaging has been also studied.

Infrared-emitting nanoparticles working in the so-called second biological window (1000 -1400 nm) allow for the acquisition of high resolution, deep tissue images due to the partial transparency of tissues in this particular spectral range. Nevertheless, although the use of non-absorbed infrared radiations has led to a drastic reduction in the tissue autofluorescence, it does not ensure the complete absence of background signal, which could be also generated by intra-body, non-intrinsic fluorescent components.

In order to explore the possibility of employing SrF_2 NPs as a novel class of Nd doped luminescent materials for real in vivo imaging in the II BW, we firstly measured the infrared emission of a control mouse, before any nanoparticles injection, under optical excitation in the I-BW (808 nm); in turn, infrared fluorescence image was obtained in the II-BW by recording the entire emitted fluorescence signal in the 1000-1400 nm spectral range (Fig. 5.10). As can be observed, even in the absence of tissue absorption (and hence of tissue fluorescence), a background signal is still generated. A NIR abdominal fluorescence of the animal tissue was collected in the 900- 1600 nm spectral region through an InGaAs camera (Fig. 5.10a-c). Results recently published by several groups already reported on the presence of visible fluorescence generated from both the abdominal and lumbar regions of living animals during in vivo imaging experiments (S. Bhaumik 2007: Y. Inoue 2008 and T. Troy 2004). Recently, Boschi et al. (F. Boschi, 2011) studied the visible emission from abdominal and lumbar region of living animals during *in vivo* fluorescence measurements, revealing that this emitted signal could even mask that of the investigated probe. The authors tried to relate the VIS background emission

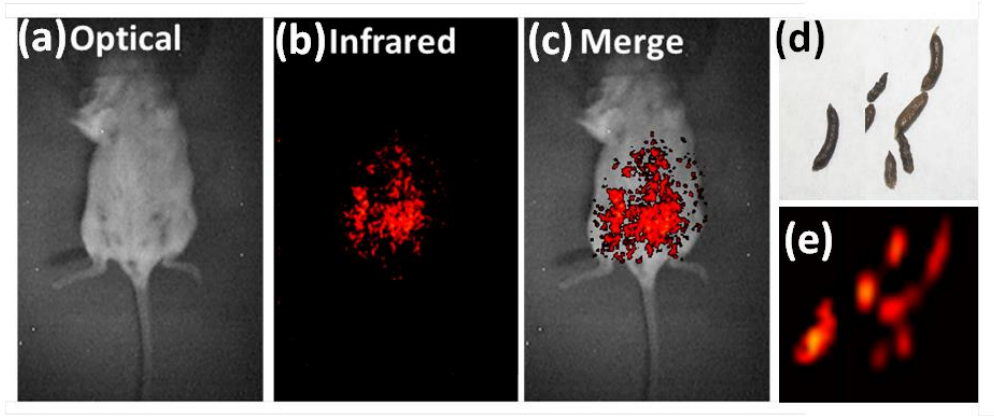

Figure 5.10 | (a) Optical, (b) fluorescence and (c) merged images of a control mouse. (d) optical image of several dregs as obtained from a conventionally fed mouse. (e) Infrared fluorescence image of the dregs. Fluorescence images were obtained with an InGaAs camera with a 900 nm long pass filter, so they account for the total emitted intensity between 900 and 1500 nm.

with the animal diet. Similarly, the collected IR emission signal coming from the ventral zone of the small mouse, could be due to a still unreported IR persistent luminescence of the molecules contained in the pellets of food used in animal facilities. Indeed, the infrared food fluorescence here reported (extending up to 1100 nm) may be generated by the presence of plant components, in particular by chlorophyll. This assumption is based on previous works published by A. A. Krasnovsky et al., who reported on chlorophyll related emission bands extending from 850 up to 1120 nm, in good agreement with the autofluorescence spectrum included in Fig 5.6 (Bottom panel) (A. A. Krasnovsky, 2014). The proposed assignment of the IR autofluorescence to the residual food is further supported by the images included in Fig. 5.10d-e that correspond to the optical and infrared fluorescence images of several dregs obtained from conventional fed mice as obtained under 808 nm laser excitation. Indeed, high concentrations of food residuals and components are expected to be present in

dregs. As can be observed, dregs also showed and intense infrared autofluorescence and this fact supports the tentative assignment of the infrared fluorescence background to the presence of different food components.

Therefore, working solely in this II biological window does not ensure a complete removal of autofluorescence as the specimen's diet shows a remarkable infrared fluorescence, which extends into the infrared spectral range when excited by 808 infrared radiation. This fact was also corroborated by the infrared fluorescence images of a conventional food pellet. Again, optical excitation was performed in the I-BW (808 nm) but fluorescent images were obtained by using different long-band pass filters. As can be observed in Fig. 5.6 (Top panel) when the fluorescent image of a food pellet is built up by recording the 900-1500 nm luminescence, a clear (high brightness) image is obtained. The intensity of pellet infrared fluorescence decreases as the “cut-off” wavelength is shifted to the infrared. No fluorescence image was obtained when the image was built up by recording wavelengths longer than 1200 nm. Fig. 5.6 (Bottom panel) reports a raw evaluation (see details of the procedure in section 5.3.3) of the NIR emission tail of a typical mouse food (red dots). By comparing it with the emission spectrum of Nd^{3+} ions (one of the most used luminescent lanthanides) in SrF_2 host nanocrystals, it is clear that food induced *in vivo* autofluorescence cannot be neglected. It completely overlaps the highest energy Nd^{3+} emission (at 900 nm) and partially overlaps the most intense one at 1050 nm. As a consequence, only the lower energy emission at 1300 nm can be used to perform high resolution bio-imaging with Nd^{3+} doped nanomaterials. From Fig. 5.6, it is clear that SrF_2: Nd NPs show an intense fluorescence in the 1100-1400 nm spectral region, following optical excitation in the I-BWs. Thus,

these NPs satisfy the essential requirements for high contrast, autofluorescence free, infrared *in vivo* imaging.

As already mentioned, the NIR light has relative low tissue absorption and high tissue penetration, therefore, the SrF_2: Nd NPs seem to be ideal bioprobes for in vivo imaging in small animals under low energy irradiation. *In vivo* imaging has been studied by injecting in a nude mouse theSrF_2:NdNPs. For this experiment, 50 μL of SrF_2:Nd nanocrystals in a phosphate buffered saline solution (PBS) (at a concentration of 4.5 10^{12} NPs/μL), were intravenously injected through the mouse retro orbital venous sinus. Afterwards, different IR fluorescence imaging experiments were performed by using an 808 nm diode laser as the excitation source and a Peltier cooled InGaAs infrared camera for detection. Two different experimental configurations were adopted. In the *free-running* mode (FRM) the obtained fluorescence images accounted for the spatial distribution of emitted light integrated in the 900-1500 nm range. Additionally, fluorescence images were also obtained in the *food fluorescence free* mode (FFFM), by attaching a 1300 nm long-pass filter to the camera objective. Thus, in this mode images were constructed by only recording the 1300-1500 nm fluorescence range. The complete removal of food fluorescence by using the FFFM configuration is demonstrated in Fig. 5.11. It shows an optical image of a food pellet and an Eppendorf partially filled with the aqueous solution of Nd:SrF_2 NPs (Fig. 5.11a).). Both the food pellet and Nd:SrF_2 NPs appear in the FRM fluorescence image (Fig. 5.11b). At variance Fig. 5.11c shows how the contribution of food emission to the fluorescence image is completely removed for images acquired in the FFFM mode.

Fig. 5.11d-f show the fluorescence images of a nude mouse after intravenous injection of 50 μL of a PBS solution containing Nd:SrF_2 NPs (at a

concentration of 0.3% in mass), as obtained in the FRM and FFFM configurations, respectively. Both images were obtained 1 hour after injection using an excitation intensity 0.5 W/cm^2 at 808 nm. The FRM fluorescence image (Fig. 5.11e) reveals luminescence signal generated from the whole abdominal and lumbar zones. On the other hand, autofluorescence free high contrast fluorescence images in Fig. 5.11f reveals that SrF_2:Nd nanocrystals are localized in the abdominal mouse zone, especially in liver and/or spleen. This was already observed in previous works on in vivo mice imaging but using other nanoparticles, like single walled carbon nanotubes with a biocompatible surface coating (A. M Smith 2009). The suitability of the 1340 nm emission of Nd:SrF_2 NPs for autofluorescence-free in vivo and ex vivo imaging is therefore clearly demonstrated. In Fig. 5.11e,f,h,i the acquired fluorescence is mainly generated from the liver and spleen, without relevant contribution from other organs such as lungs or kidneys. Moreover, it is worth to notice that by acquiring the luminescence in the two spectral ranges (900-1500 nm and 1300-1500nm), the intensity, the shape, and the image resolution are different for the IR images of both a living mouse and a sacrificed open one. Indeed, by selecting the luminescence at around 1330 nm, the emission area decreases together with the intensity of the NPs signal, while, in turn, a better image resolution is obtained. This is due to the low relative intensity of the 1330 nm emission ($^3F_{3/2}$-$^4I_{13/2}$ transition) in respect to the one at 1050 nm ($^3F_{3/2}$-$^4I_{11/2}$ transition), while the better resolution is due to the lower scattering contribution at longer emission wavelengths. A complete removal of autofluorescence is not only required to get high contrast fluorescence in vivo images but also to extract reliable information about the biodistribution of intravenously injected NPs. As a general procedure, long-term biodistribution of NPs in small animals is studied

by measuring the NPs fluorescence intensity generated by the different organs, after removal from dissected animals at different times after the injection of the NPs. The amount of NPs retained in each organ is, then, estimated from the measured fluorescence intensity. Obviously, this procedure is only valid when there is absolute certainty that no background fluorescence is present. Fig. 5.12 shows the biodistribution profile of the Nd doped SrF_2 NPs in mouse organs together with the IR images collected by the InGaAs camera in the two spectral regions. High fluorescence in the 900-1500 nm spectral range is recorded for liver and spleen, this may be due to the accumulation of the injected dose in these organs; whereas the lung, heart, kidney, and brain seem to account for a lower NPs concentration and, consequently, weaker IR emission. The stomach and the intestine present a small signal that can be related to the presence of food.

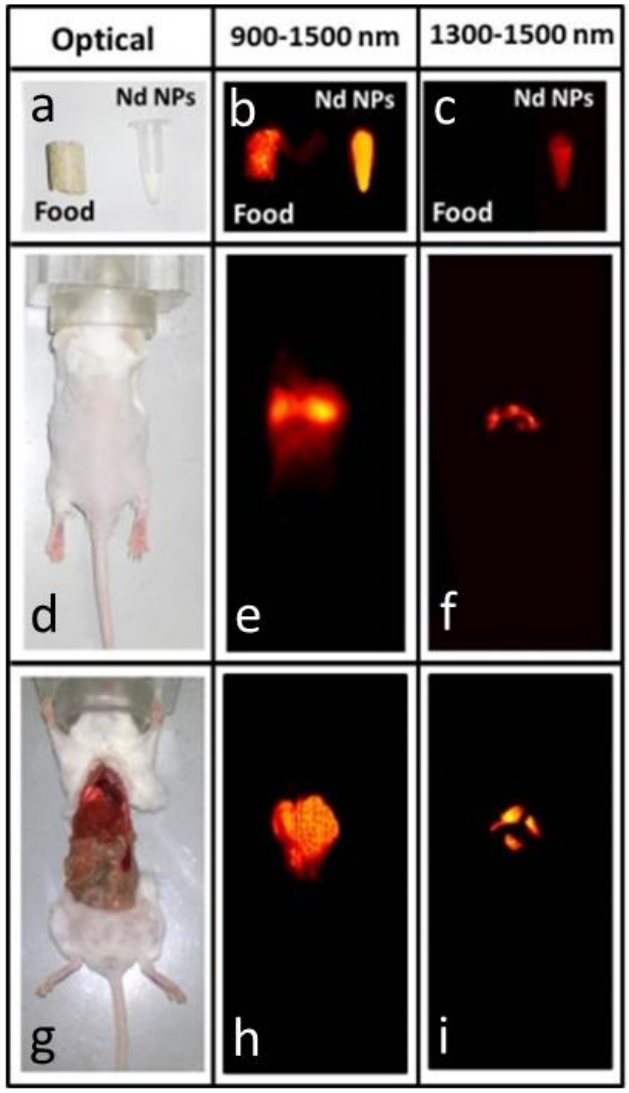

Figure 5.11 | (Left Column). Optical images of a mouse food pellet and an Eppendorf containing a colloidal solution of SrF_2 : Nd NPs (a), of a living mouse after intravenous administration through the retro-orbital venous sinus of 50 µL of a colloidal solution of SrF_2:Nd NPs in phosphate buffered saline (d) and of the same mouse after being sacrificed and opened to get direct access to organs (g). (Middle column) Corresponding fluorescence images of the three systems obtained under 808 nm illumination and recording the fluorescence in the 900-1500 nm range. (Right column). Fluorescence images also obtained under 808 nm excitation but in this case recording fluorescence intensity in the 1300-1500 nm range.

By selecting the 1330 nm luminescence, we can avoid the strong autofluorescence background given by the mice food, which can affect NPs luminescence when using the higher 1050 nm emission band. Indeed, after the signal of food is removed, the relative intensities in liver and spleen remain the same as for the 1050 nm Nd^{3+} ion emission). However, the lack of observation of minor signals from other organs is probably due only to the smaller signal-noise ratio.

The results on autofluorescence-free biodistribution pattern of SrF_2 :Nd NPs, pointing out preferential NP accumulation by liver and spleen, are in reasonable agreement with those previously found for other LNPs, concerning short and long term biodistribution of nanoparticles in mice. For instance, Naczynski et al. investigated the time-resolved biodistribution of rare earth doped infrared NPs in mice after intravenous injection (D. J. Naczynski, 2013). They found that RENPs were efficiently retained by the liver for post injection times larger than 1 minute. This result is also in agreement with previous works dealing with the dynamical biodistribution of carbon nanotubes intravenously injected in mice (G. Hong, 2012).

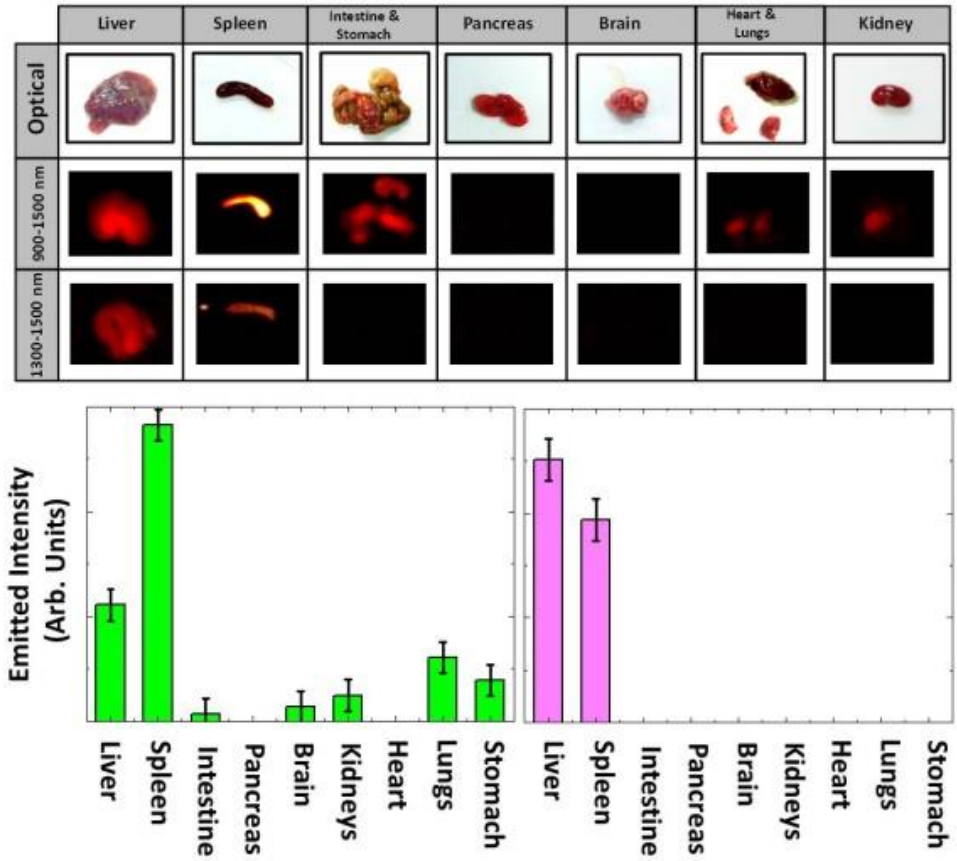

Figure 5.12 | (a) Optical images and fluorescence images in the 900-1500 and 1300-1500 nm spectral detection ranges of the organs extracted from a sacrificed mouse 1 hours after an intravenous injection of SrF_2:Nd NPs. (b) 900-1500 nm integrated fluorescence intensity obtained from the different organs. (c) 1300-1500 nm integrated intensity obtained from the different organs. In all cases, the integrated fluorescence intensity has been normalized by the organ´s weight.

The enhanced uptake from the highly perfused organs such as liver and spleen may be attributed to the macrophages residing in these tissues, which are responsible for capturing particulates and macromolecules circulating in the blood (R. Kumar, 2010.**)**. Moreover, it is widely assumed that bio-distribution of intravenously injected NPs is also strongly determined by the particular surface charge of the injected NPs. This charge dependence is correlated with the

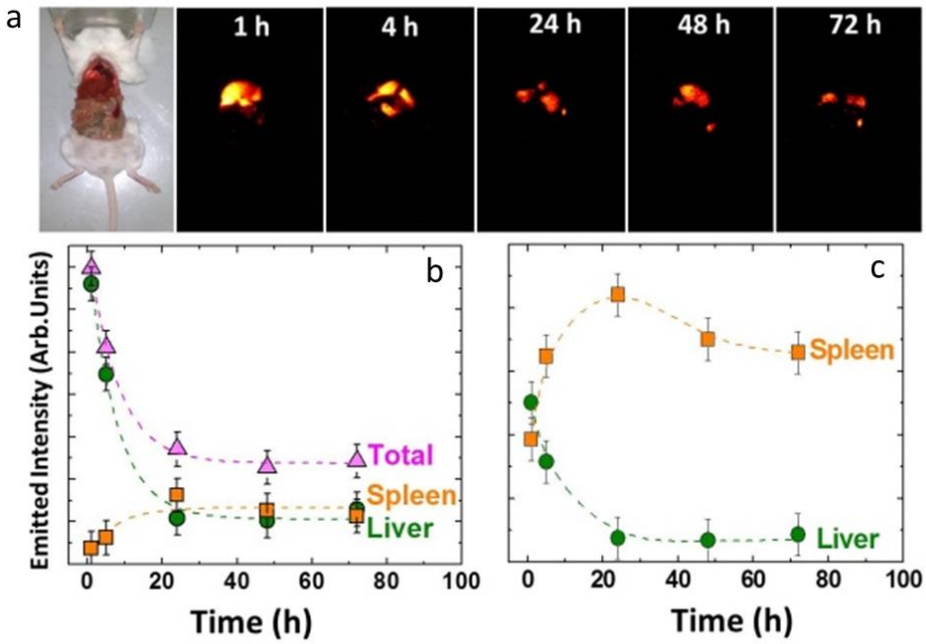

Figure 5.13 | (a) Ex vivo fluorescence images (obtained in the 900-1500 nm detection spectral range) corresponding to different mice sacrificed at different times from the intravenous injection of SrF_2:Nd NPs. (b) Integrated fluorescence intensity obtained from the liver and spleen as a function of the time elapsed between injection and ex vivo image procedure. (c) Evolution of the weight normalized fluorescence from the liver and spleen as a function of the time elapsed between injection and ex vivo image procedure. Dots are experimental data and dashed lines are guides for the eyes.

binding to different proteins as a result of the different NP charges. As strontium fluoride NPs are negatively charged with a Z potential close to -25 mV, they are expected to accumulate preferentially in both liver and spleen; whereas, from the literature, positively charged NPs display a larger accumulation rate in the other organs (S. Hirn, 2011; K. Xiao, 2011; L. Balogh, 2007).

The biodistribution pattern of LNPs in mice is also strongly time dependent. In order to check for the possible time dependence of SrF_2:Nd NPs

accumulation by different organs, we monitored the 1330 nm IR signal over a period of 72 h on different post retro orbital venous injected mice. We intravenously injected the same dose of SrF_2:Nd NPs (50 µL of a 0.3 % in mass concentrated aqueous solution) in 5 different mice. Then these mice were sacrificed at different times after injection (1h, 4, 24, 48 and 72 hours) and the *ex vivo* fluorescence images were systematically acquired (see Fig. 5.13a) in the FFFM configuration. Results show that the amount of SrF_2:Nd NPs accumulated in liver and spleen follows a completely different time evolution. For a more quantitative estimation, the signal from the organs of the sacrificed mice was integrated as a function of time and is displayed in Fig. 5.13b, together with the total fluorescence intensity (sum of the fluorescence intensities) generated from the liver and spleen.

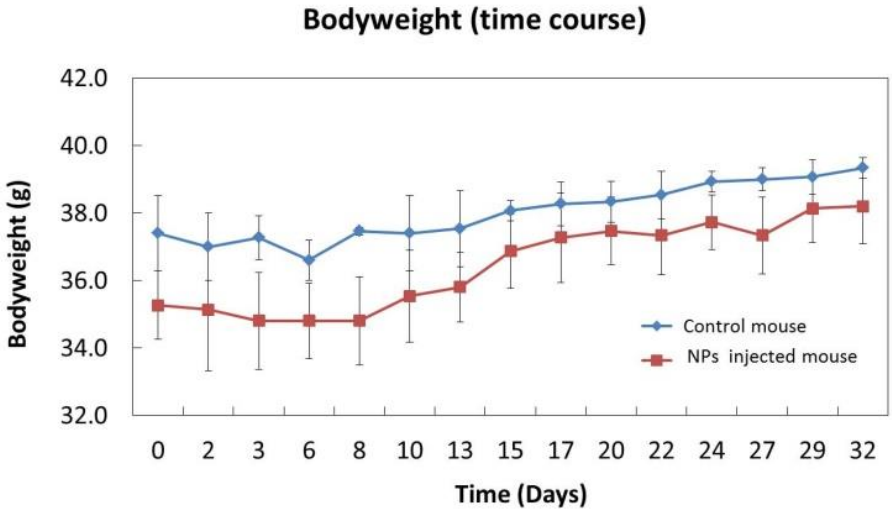

Figure 5.14 | Time evolution of the averaged weight (calculated over 3 individuals) after intravenous injection of Nd:SrF_2 NPs. The time evolution of the averaged weight calculated over 3 control mice has been also included. Error bars correspond to the weight standard deviation in each group.

At short times (< 20 hours after injection) SrF_2:Nd NPs were mainly retained by the liver whereas for longer times, the fluorescence generated from the spleen becomes dominant, reaching a saturation level after 24 h. This fact reveals a dynamical transfer of SrF_2:Nd NPs from the liver to the spleen during the first 80 hours after intravenous injection. The different time evolution of the fluorescence generated from both liver and spleen is more evident in Fig. 5.13c, which shows the time evolution of the fluorescence intensities from these two organs normalized to their respective weight.

The possible toxicity of the SrF_2:Nd NPs was studied by controlling their effect on mice over a period of 1 month. Fig. 5.14 shows the body weight variations of a mouse after intravenous injection of an identical dose of SrF_2:Nd RENPs as that used throughout the previously described for *in vivo* fluorescence imaging experiments. For the sake of comparison, the body weight variation of a "control" mouse intravenously injected with the same volume (50 µL) of PBS, has been also included. No weight loss induced by stress and pain conditions is registered in the injected mouse with respect to a control one. The *in vitro* cytotoxicity of the SrF_2:Nd NPs has been also investigated (Fig. 5.15). The toxicity of the SrF_2:Nd nanoparticles was investigated in HeLa cells after incubation with a medium containing NPs at different concentrations (25, 50 and 100 µg/mL). No evidence of relevant cytotoxicity has been found for the concentrations and incubation times studied in this work. Fig. 5.15 shows as an inset an infrared fluorescence image of HeLa cancer cells incubated during 2 hours in a PBS solution containing SrF_2:Nd NPs at a concentration of 50 µg/mL. This fluorescence image evidences the adhesion of SrF_2:Nd NPs to the cell membrane.

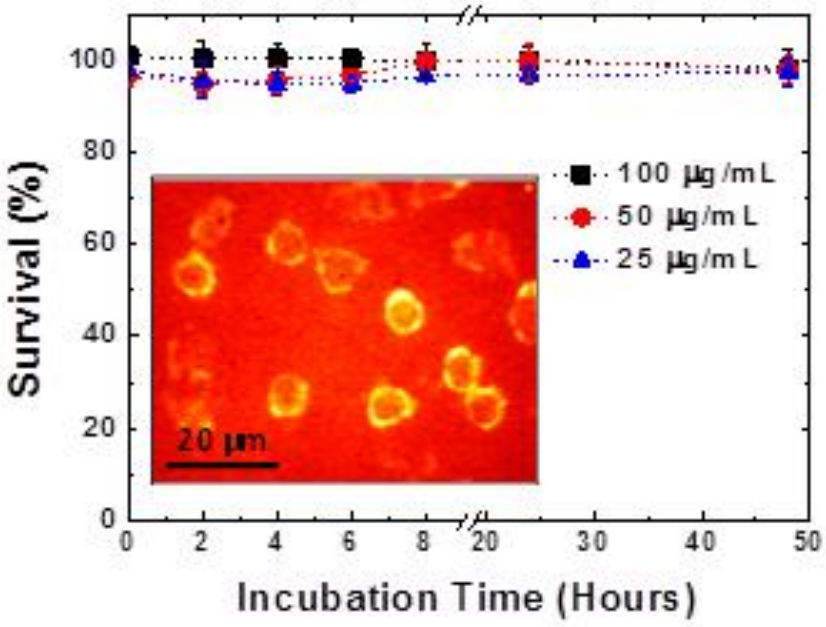

Figure 5.15 | Percent survival of HeLa cell line incubated with different concentrations of SrF_2:Nd NPs for different incubation times. Each experimental point (dot, square or triangle) corresponds to the mean value (SD) obtained from three different experiments. Inset shows the infrared fluorescence infrared image (850-1450 nm) of HeLa cells incubated with a SrF_2:Nd NPs/PBS solution (50 µg/mL) during 2 hours**.**

5.6 CONCLUSION

Novel approaches for high contrast, deep tissue, in vivo fluorescence biomedical imaging are based on infrared-emitting nanoparticles working in the so-called second biological window (1000 -1400 nm). SrF_2:Nd NPs could behave as promising high penetration infrared contrast agents for dynamical fluorescence anatomical in vivo imaging, with even a drastic reduction in the

contribution of autofluorescence. In this chapter, the 1340 nm emission band of Nd^{3+} ions embedded in SrF_2 nanoparticles has been systematically studied in order to produce high contrast *in vivo* fluorescence images. A complete removal of autofluorescence due to the specimen's diet infrared fluorescence is imperative for the development of reliable bio-distribution studies. The *in vivo* imaging through Nd emission at the lowest energy is completely free from the food-related fluorescence. This allows investigating the biodistribution pattern of these NPs in mice as a function of the post injection time. The obtained results indicate a main accumulation of these NPs in the liver and spleen and a transfer of NPs from the liver to spleen with the post injection time.

5.7 REFERENCES

Balogh L. et al. (2007), *Significant effect of size on the in vivo biodistribution of gold composite nanodevices in mouse tumor models*. Nanomedicine 3, pp. 281-296.

Bao G. et al. (2013), *Multifunctional Nanoparticles for Drug Delivery and Molecular Imaging*. Annu. Rev. Biomed. Eng. 15, pp. 253–282.

Bhaumik S. et al. (2007), *Strategies to minimize background autofluorescence in live mice during noninvasive fluorescence optical imaging*. Lab Animal 36, pp. 40-43.

I. Brigger et al. (2002), *Nanoparticles in cancer therapy and diagnosis*. Adv. Drug Deliv. Rev. 54, 5, pp. 631–651.

Chen G. (2012), *Core/shell $NaGdF_4:Nd^{3+}$/NaGdF4 nanocrystals with efficient near-infrared to near-infrared downconversion photoluminescence for bioimaging applications*. ACS Nano. 24, 6, pp. 2969-2977.

Boschi F. et al. (2011), *Optical imaging of alpha emitters: simulations, phantom, and in vivo result.* J. Biomed. Opt. 16.

Gautama et al. (2013), *Synthesis of nanoparticles, their biocompatibility, and toxicity behaviour for biomedical applications*. J. Mater. Chem. B 1. pp. 5186-5200.

Guosong H. et al. (2012), *In Vivo Fluorescence Imaging with Ag_2S Quantum Dots in the Second Near-Infrared Region*. Angew. Chem. Int. Ed. 51, pp. 9818-9821.

Hirn S. et al. (2011), *Particle size-dependent and surface charge-dependent biodistribution of gold nanoparticles after intravenous administration*. Eur. J. Pharm. Biopharm. 77, 407-416.

Hong G. et al. (2012), *Multifunctional in vivo vascular imaging using near-infrared II fluorescence*. Nature Medicine 18, 1841-1846.

Idris N. et al. (2012), *In vivo photodynamic therapy using upconversion nanoparticles as remote-controlled nanotransducers.* Nature Medicine 18, 10, pp. 1580–1585.

Inoue Y. et al. (2008), *Diet and abdominal autofluorescence detected by in vivo fluorescence imaging of living mice*. Mol. Imaging 7, pp. 21-27.

Jaque D. and Vetrone F. (2012), *Luminescence nanothermometry*. Nanoscale 4, pp.4301-4326.

Juzenas P. et al. (2008), *Quantum dots and nanoparticles for photodynamic and radiation therapies of cancer*. Adv. Drug Deliv. Rev. 60, 15, pp. 1600-1614.

Krasnovsky A. A., Jr. and Kovalev Y. V. (2014), *Spectral and kinetic parameters of phosphorescence of triplet chlorophyll a in the photosynthetic apparatus of plants*. Biochemistry -Moscow 79, pp. 349-361.

Krol S. et al. (2013), *Therapeutic Benefits from Nanoparticles: The Potential Significance of Nanoscience in Diseases with Compromise to the Blood Brain Barrier*. Chem. Rev. 113, pp. 1877−1903.

Kumar R. et al. (2010), *In Vivo Biodistribution and Clearance Studies Using Multimodal Organically Modified Silica Nanoparticles. ACS Nano* 4, 2, pp. 699–708.

Labatto M. E. (2011), *Perspectives and opportunities for nanomedicine in the management of atherosclerosis* Nature Reviews: Drug Discovery 10, 835.

Gang. B. et al.(2013), *Multifunctional Nanoparticles for Drug Delivery and Molecular Imaging*. Annu. Rev. Biomed. Eng, 15, pp. 253–282.

Maldiney T. (2011), *Controlling Electron Trap Depth To Enhance Optical Properties of Persistent Luminescence Nanoparticles for In Vivo Imaging*. J. Am. Chem. Soc. 133, pp. 11810–11815.

Maldiney T. (2012), *In Vitro Targeting of Avidin-Expressing Glioma Cells with Biotinylated Persistent Luminescence Nanoparticles*. Bioconjugate Chem. 23, pp. 472−478.

Matsumura Y. and Ananthaswamy H. N. (2004), *Toxic effects of ultraviolet radiation on the skin*. Toxicol. Appl. Pharmacol. 195, pp. 298-308.

Moore E. G. et al. (2009), *From Antenna to Assay: Lessons Learned in Lanthanide Luminescence*. Acc. Chem. Res. 42, 4, pp. 542-553.

Mosmann T.(1983), *Rapid colorimetric assay for cellular growth and survival: application to proliferation and cytotoxic assay.* J Immunol Methods., 65, 1-2, pp.55-63.

Naccache R. (2012), *High Resolution Fluorescence Imaging of Cancers Using Lanthanide Ion-Doped Upconverting Nanocrystals*. Cancers, 4, pp. 1067-1105.

Naczynski D. J. et al. (2013), *Rare-earth-doped biological composites as in vivo shortwave infrared reporters.* Nature Commun., 4, 2199.

Naczynski D. J. et al. (2014), *Rare Earth Nanoprobes for Functional Biomolecular Imaging and Theranostics.* J Mater Chem B Mater Biol Med., 2, 20, pp. 2958–2973.

Ntziachristos V. (2006), *Fluorescence Molecular Imaging*. Annu. Rev. Biomed. Eng. 8, pp. 1–33.

Payne A. et. Al (1991), *Spectroscopy and gain measurements of Nd^{3+} in SrF_2 and other fluorite-structure hosts.* J. Opt. Soc. Am. B 8, 4, pp. 726-739.

Pedroni M. et al. (2013), *Water (H2O and D2O) Dispersible NIR-to-NIR Upconverting Yb3+/Tm3+ Doped MF2 (M = Ca, Sr) Colloids: Influence of the Host Crystal*. Cryst. Growth Des. 13, pp. 4906-4913.

Ramos-Lara F. (2006), *Optical spectroscopy of Nd3+ ions in poly(acrylic acid).* J. Phys.: Condens. Matter 18 pp. 7951–7959.

Rocha U. et al. (2013*), Subtissue Thermal Sensing Based on Neodymium-Doped LaF_3 Nanoparticles.* ACS Nano 7, 2, pp. 1188–1199.

Rocha U. et al. (2014), *Neodymium doped LaF_3 nanoparticles for fluorescence bioimaging in the second biological window*. *Small* 10,6, 1141-54.

Smith A. M. et al. (2009), *Bioimaging. Second window for in vivo imaging*. Nat. Nanotechnol. 4, 710-711.

Teker K. (2005), *Applications of Carbon Nanotubes for Cancer Research*. NanoBiotechnology 1, 2, 171-182

Troy T. et al. (2004), *Quantitative comparison of the sensitivity of detection of fluorescent and bioluminescent reporters in animal models*. Mol. Imaging 3, 9-23.

Vetrone F. (2010), *Intracellular imaging of HeLa cells by non-functionalized $NaYF_4 : Er^{3+}$, Yb^{3+} upconverting nanoparticles*. Nanoscale, 2, 495–498.

Willner I. and Willner B. (2010), *Biomolecule-Based Nanomaterials and Nanostructures*. Nano Letters. 10, 10, 3805–3815.

Xiao K. et al. (2011), *The effect of surface charge on in vivo biodistribution of PEG-oligocholic acid based micellar nanoparticles*. Biomaterials 32, 3435-3446.

Yi X. (2014), *Near-infrared fluorescent probes in cancer imaging and therapy: an emerging field*. J. Nanomed. 9, 1347–1365.

Zhang L. *et al.* (2008), *Nanoparticles in medicine: therapeutic applications and developments*. Clin. Pharmacol. Ther. 83, pp. 761–769.

6. CONCLUSIONS

The aim of this PhD thesis was the study of inorganic nanoparticles to be applied in different fields, such as in lighting, sensing, and even in the novel rapid developing field of nanomedicine. We propose a brief discussion of the investigation performed on HfO_2 and SrF_2 NPs, together with a view of the perspectives of this thesis.

6.1 APPLICATIONS AND PERSPECTIVES OF TUNABLE AND WHITE COLOURS EMITTING NANOPARTICLES – THE NOVELTY OF HfO_2

AIM 1. INVESTIGATION OF THE STRUCTURE – EMISSION RELATIONSHIP. IS IT POSSIBLE A DEEP CONTROL OF THE NPS LUMINESCENCE PROPERTIES?

In the last years, monoclinic HfO_2 has gained interest for its dielectric properties and, because of its excellent physical properties and wide band-gap, it has been proposed as phosphor for fluorescent lighting, display devices, X-ray monitoring and imaging, and as scintillator. However, hafnia industrial applications as well its optical applications in nanocomposites and ceramics require that many problems and drawbacks must be solved. In the case of the nanocomposites, a strong reduction of the emitted light scattering is desirable which can be obtained through the tailoring of the dimensions of the materials. At the same time, the crystalline structure control through synthetic parameters can assure the fabrication of transparent ceramic with luminescent materials showing a cubic structure.

In this work, a facile synthesis approach has been exploited to produce metal oxide nanoparticles can be obtained by non-aqueous sol - gel method. This strategy has shown several important advantages like the great versatility, and the enhanced crystal phase control of the final product, especially when it is confined in nanometric dimension. The technique has allowed to obtain (< 300 °C) HfO_2 nanoparticles at low T, featuring a uniform spherical morphology, diameter < 5nm, and a high crystalline grade. The RE ions doping of the NPs has allowed the investigation of the optical response of the material, while controlling the structural properties.

The XRD and TEM results have evidenced the possibility to stabilize at room temperature the cubic phase of HfO_2. The monoclinic to cubic phase change has been induced by the incorporation of trivalent RE with a concentration of at least 5 mol %. Such phase modification has been carried out simply by doping with Eu^{3+} as well as by simultaneously co-doping with $Eu^{3+}$and non-luminescent Lu^{3+}ions. The consequent change in the luminescence features of hafnia NPs has been evidenced by RL and PL studies, by monitoring the variation of the hypersensitive 4f-4f related red emissions of Eu^{3+}, which are strongly sensitive to symmetry of the environment.

These results represent an important data set for a better comprehension of the structure-property relationship in materials confined into nanoscale dimensions. Although more effort must be focused on exploring the luminescence mechanism involved in nanoscale hafnia in order to successively optimize its light output and luminescence characteristics, these findings open the way for a high level of control on the functional/structural properties through the appropriate choice of dopants and their concentrations. Moreover,

in the perspective of hafnia application as optical nanocomposites or ceramics, the transformations occurring during thermal treatments can help to predict the stability of the modified crystalline cubic phases and the optical performance gain.

AIM 2. COLOURS TUNABILITY OF REs DOPED HAFNIUM OXIDE NPs.

Once the possibility to control and change the crystal structure of hafnia nanoparticles has been proved, the possibility to induce a colour tunability of its emission, has been also investigated. The incorporation of different rare earth emitting ions, like Tb and Eu, in the hafnia host has been successful, and it led to the modification of the NPs luminescence spectra depending on the type and the concentration of the dopants, together with the phase of the matrix. In this regard, the possibility of tuning the emission spectrum by co-doping with multiple RE has been demonstrated, while the NP cubic structural stabilization can be obtained by using optically inert Lu^{3+} ions.

Finally, it has been possible to highlight a luminescence colour switch depending on excitation wavelength thanks to the selective excitation of intrinsic or activator-related emissions. The emission light varies from blue to orange, while switching the europium dopant related luminescence. The blue contribution may be attributed to different origins, among which the surface defects related origin is the most probable, as the blue band decreases after the high temperature thermal annealing of the sample.

AIM 3. INTRINSIC WHITE LIGHT EMISSION OF UNDOPED NPS – AND ITS POTENTIAL APPLICATIONS.

Given the importance of HfO_2 as host material for luminescent lanthanides, its intrinsic optical response is also worth of investigation. Undoped HfO_2 NPs have been studied considering the effect of the size and of the fine structural modifications, in terms of crystal growth and coalescence of crystalline domains, occurring during the calcination process.

In this thesis the tunable optical features observed in undoped monoclinic HfO_2 have been reported; a broad emission has been observed in the visible range, and correlated both to intrinsic surface defects and to impurities. The observed blue emission is composite and it was possible to distinguish all of its spectral components mainly from PL time decay measurements. A slow decay contribution is due to the accidental titanium impurities; in turn the faster components have been attributed to intrinsic defects. In particular, the blue emissions at 2.5 and 2.9 eV are clearly related to defects lying at NPs grain boundaries. Moreover, the presence of an emission at 2.1 eV enables a white luminescence under near-UV excitation.

The investigation of these intrinsic optical features with the evolution of all the structural transformations such as the growth and coalescence of crystals, discloses the possibility to design and optimize the luminescence properties of Hf oxide NPs, by finely tuning structural coordinates. In general, the data reported might inspire future research on the development of new luminescent phosphors based on metal oxides and dopant-free white light emitting phosphors. Moreover, due to its excitation at near-UV wavelengths,

the studied warm white luminescence might be considered and evaluated for phosphor-based lighting and light-harvesting in photovoltaics applications.

Finally, a strong focus must be put on the RL results. Also the RL measurements have revealed the presence of a composite broad band ranging from the visible to the ultraviolet. The blue component is undoubtedly related to the Ti impurity and its intensity increases during the thermal treatment in such a way to be comparable to that of standard commercial materials, evidencing the potential of Ti-doped HfO_2 NPs as scintillators.

6.2 SrF_2, Nd doped NPs emitting in the II biological window as efficient probes for bioimaging

Nanoscale dimensions are also necessary in biotech applications where the material is required to travel in blood vessels and penetrate into cells. In this thesis we have also investigated the luminescence properties of SrF_2: Nd emitting NPs. It has been revealed that their IR luminescence can be used for biological applications such as high contrast, deep tissue, in vivo fluorescence biomedical imaging. In particular the SrF_2 NPs have been efficiently excited at 800 nm and among the well - known Nd related emissions, the one at 1300 nm has shown a stronger intensity with respect to the one obtained for the Nd^{3+} ion in other host matrices. Working in this wavelengths range assures a good human tissue transparency, scattering and autofluorescence reduction, thus an increase of the spatial resolution and improvement in the beam penetration depth.

In addition, we have shown that the infrared excitation can induce an auto-fluorescence signal generated specimen's diet. Only the use of the strong 1300 nm emission band of Nd^{3+} ions embedded in SrF_2 nanoparticles has led to the production of auto-fluorescence free images. The strong brightness, the chemical and physical stability as well as high biocompatibility make SrF_2:Nd nanocrystals very promising infrared nanoprobes for imaging and bio-distribution studies in the second biological window. The investigation of the IR fluorescence emission of NPs in *in-vivo* experiments has revealed the possibility to understand how the NPs can be tolerated by the animal body, which organs are imputed to their elimination and the time required for the NPs to reach the different animal organs. The future studies can be performed by analyzing the way in which the NPs parameters, such as structure, morphology, and dopant concentration may influence the biodistribution results and the applicability of SrF_2: Nd for in vivo bioimaging purpose.

APPENDIX A. MORPHOLOGICAL AND STRUCTURAL CHARACTERIZATION OF NANOPARTICLES

In this appendix, we report the main experimental techniques to characterize the morphology and structure of synthesized hafnium oxide NP (HfO_2 or hafnia) at the Department of Materials -Multifunctional Materials Laboratory of EHT (Zurich, Switzerland) and at the Department of Materials Science of the Università degli Studi di Milano-Bicocca (Milano, Italy).

A.1 INTRODUCTION

Much progress in nanoscience and nanotechnology has been made in the past few years thanks to the development of sophisticated physical methods to characterize nanomaterials (Rao C.N.R. and Biswas K., *Characterization of Nanomaterials by Physical Methods*. Annual Review of Analytical Chemistry , 2009, 2, pp.435‑462). Characterization of nanomaterials can be performed at different levels. Vibrational spectroscopies, such as Raman and Fourier transform Infrared spectroscopy (FTIR), can be used for the analysis of the material composition. Thermal analysis such as thermogravimetric analysis (TGA) and differential thermal analysis (DTA) are useful to quantitatively determine the phase stability of pure and composite organic materials. Scanning and tunnelling electron microscopies (SEM, TEM) are suitable to study the size, shape, and morphology of nanostructures down to the atomic scale; electron diffraction (ED) can give detailed crystal structure information. Energy dispersive X-ray spectroscopy (EDS) and induced coupled plasma mass

spectroscopy (ICP-MS) can provide elemental analysis. X-ray scattering (XRD) leads to fine information about the crystal geometry, while nanoscale sizes of crystals can be estimated through the Scherrer analysis of broadened peaks. Furthermore, optical spectroscopic techniques such as photoluminescence excitation and emission, and radioluminescence (PLE, PL, and RL) are commonly employed to investigate the electronic configuration of the emitted species in nanoparticles, as well as size confinement related phenomena. Here we provide a brief introduction to the most relevant techniques used in the structural characterization of undoped and doped HfO_2 nanocrystals presented in this thesis.

A.2. X-RAY DIFFRACTION (XRD)

XRD has been widely used for the determination of the crystalline character, structure, and size of nanoparticles. A beam of X-rays is diffracted by the crystalline specimen according to Bragg's law. The intensity of the diffracted beam is measured as a function of the diffraction angle (2ϑ) and the specimen's orientation. The diffraction pattern can be used to identify the crystalline phases and their structural characteristics, while the determination of the average size of the particles can be calculated *via* the Scherrer formula

$$a = 0.9\lambda/B \cos\vartheta \qquad \text{(Eq. A.1)}$$

where a is the domain size, λ is the X-ray wavelength, B is the full width at the half maximum (in radians) of the X-ray peak, and ϑ is the Bragg angle.

XRD measurements were conducted on a X'Pert Pro powder diffractometer (PANalytical B.V., The Netherlands) equipped with a high-temperature oven-chamber HTK 1200 (Anton Paar GmbH, Austria) containing the analysed powder supported on an alumina sample holder. The diffractometer was operated in

reflection mode under constant irradiated volume conditions with Cu Kα radiation (45 kV, 40 mA). For in-situ analysis, the sample was heated from room temperature (RT) to 1000 °C; meanwhile every 100 °C a XRD scan was recorded. The subsequent XRD scan took 20 min. For ex-situ analysis, after annealing the samples in a muffle oven to the corresponding temperatures, they were allowed to cool down under ambient conditions and subsequently introduced into the high-temperature oven-chamber. All XRD scans were recorded at RT.

The crystallite sizes of monoclinic hafnia were calculated by Scherrer formula using the FWHM values extracted from the Hafnia (-111) peaks at 2θ = 28°. In turn, the average crystallite size of cubic crystals was calculated by applying the Scherrer formula on the (111) plane diffraction located at 2θ = 30°.

A.3. GAS ADSORPTION METHOD (BET)

The determination of the specific surface of the nanoparticles (powders) was performed by means of the Brunauer-Emmett-Teller (BET) technique. This technique is based on the physical adsorption of gases on the external and internal surfaces of porous materials and particles. Such materials establish an adsorption equilibrium with a gas at a temperature T and relative vapour pressure p/p_o. The amount of adsorbed gas is dependent on its relative vapour pressure and is proportional to the total external and internal surface of the material. The isotherm adsorption, obtained by determining the relation between the equilibrium pressure and the amount of gas adsorption, gives the surface area of the sample. In our work, prior to determining the surface area, the samples were outgassed at 120 °C for at least 12 h and krypton gas adsorption measurements were carried out at 77 K on a Quantachrome Autosorb iQ. For selected samples with sufficient surface area, the surface area

measurements were confirmed by nitrogen gas sorption. The surface area was calculated via a multipoint BET method. Krypton (99.999%) and nitrogen (99.999%) were provided by PanGas AG, Switzerland.

A.4.TRANSMISSION ELECTRON MICROSCOPY (TEM)

Electron microscopy allows the observation of matter with atomic resolution. TEM measurements were made on a Philips FEI Tecnai F30 microscope operated at 300 kV on samples prepared by depositing onto carbon coated Cu grids 10 µL of ethanol (Aldrich) suspension of washed NPs. Alternatively, the products (colloidally stabilized HfO_2 nanoparticles or fine-grained calcined particles redispersed in iso-propanol) were deposited on a copper-grid-supported perforated transparent carbon foil. A field emission electron-source transmission electron microscope (JEOL 2010F) was operated at 200 kV.

A.5. ANALYSIS OF SAMPLE COMPOSITION

Induced Coupled Plasma (ICP) elemental studies were achieved through a Perkin-Elmer ICP-OES Optima 7000 DV. Energy Dispersive X-ray Spectroscopy (EDS) measurements were measured on a Zeiss Leo Gemini 1530.

A.6.THERMAL ANALYSIS METHODS

With the aim of characterizing nanomaterials during synthesis, preparation and control of final product properties, thermal analysis techniques are considered as the most relevant tools. Thermoanalytical methods are successfully applied for the determination of phase transitions, thermally induced chemical reactions and decompositions, gas adsorption and desorption studies, and thermal transport properties. Frequently, inorganic materials, such as metal oxide nanopowders, are analysed by simultaneous thermogravimetry and

differential scanning calorimetry (TG-DSC) to show the reactivity and thermal stability, together with the amount and decomposition ranges of the surface coatings.

TG-DSC measurements were performed on a Netsch STA 449C; samples were prepared by placing nanopowders in Pt crucibles with a lid, and measured in Ar/O_2 flux against empty Pt crucibles as a reference. A subsequent cycle was performed on the annealed sample as correction measurement.

A.7.RAMAN SPECTROSCOPY

In this work, micro-Raman spectra were collected in backscattering configuration using the 633 nm line of a He-Ne laser on a Labram Dilor spectrometer. Raman spectra of pure hafnia were performed through the confocal Raman microscope Renishaw.

A.8.REFLECTIVITY

In order to calculate the absorption spectrum of scattering NP powders, attenuated total reflectance (ATR) measurements were performed on a Bruker Alpha FT-IR Spectrometer equipped with diamond ATR optics.

APPENDIX B. LUMINESCENCE STUDY OF Lu_2O_3 NANOPARTICLES - ROLE OF LUTETIUM PRECURSORS

In this appendix, the study of nanocrystalline Lu_2O_3 obtained by the reaction of two different precursors $Lu(ac)_3$ and $LuCl_3$, is proposed. This preliminary investigation concerns the dependence of radioluminescence (RL) features on the structural properties, such as the morphology, the size, and the crystal phase in order to explore the possible use of Lu_2O_3 nanoparticles (NPs) as scintillators.

B.1 INTRODUCTION

A wide range of materials, including inorganic crystals, organic molecules and polymers, glasses and gases have been proposed as scintillators i.e. materials that are able to absorb particles or photons of high energy and convert them into light in the visible or UV region. They have been widely studied in technological fields like radiation detection and biotech applications. Today inorganic scintillators are either single crystals or polycrystalline transparent ceramics. Lu_2O_3:Eu is a well-studied inorganic scintillator of cubic structure which is interesting due to its high density of 9.4 g/cm3 and high atomic mass (Z=71) which are related to its stopping power, its radiation hardness and environmental stability (L. Li et al., 2010 and Y. Shi, 2009). It is well known that the production of single crystals is very expensive and also difficult for high melting oxides as Lu_2O_3 with a melting point of 2490 °C. Cheaper production is in principle offered by the sintering of nanoparticles into a bulk ceramic (E. Zych et al., 2002). Moreover, nonaqueous sol-gel synthesis allows the control of the reaction parameters and tailoring of morphology and size of crystalline

particles. Therefore, Lu_2O_3 have been synthetized through this route and doped with 1 mol% Eu. Two different precursors $Lu(ac)_3$ and $LuCl_3$ in benzyl alcohol have been used. The reaction has been performed by a solvothermal synthesis in an autoclave. In addition, NPs from $Lu(ac)_3$ reaction have been synthetized and heated under microwave irradiation.

B.2. MATERIALS

All the chemical reactions performed at ETH (Zürich, CH) used anhydrous benzyl alcohol ($C_6H_5CH_2OH$, 99.8%, Sigma-Aldrich) as solvent. As precursors containing the rare earth metal, lutetium chloride ($LuCl_3$, 99.99%, Sigma-Aldrich) and hydrated lutetium acetate ($(CH_3CO_2)_3Lu\ xH_2O$, $Lu(ac)_3$, Multivalent Laboratory, Eriswell, UK) were used. Europium Acetate ($(CH_3CO_2)_3Eu \cdot xH_2O$, ABCR-Chemicals) was used for doping.

The reactions were performed in autoclaves for 48 h @ 220 °C and by microwave heating for 1, 2, 10, 60 min @ 200°C. The obtained powders were analysed by XRD (at ETH), which allows determining the crystalline phases and their size (Scherrer equation). The heat treatment was performed directly *in situ* and the evolution of the XRD pattern was monitored up to either 500 or 1200 °C. TEM analyses were also performed on a few samples.

The RL characterization was performed at the University of Milano Bicocca. UV-visible emission of the samples was recorded in steady state, while irradiating them with X-rays at room temperature (tungsten anode, operated at 20 kV).

B.3. MORPHOLOGY AND STRUCTURE

AUTOCLAVE SYNTHESIS:

The products obtained by the reaction of Lu acetate precursor consisted of squared platelets with a side length widely distributed from 100 nm up to several microns (Fig. B.1).

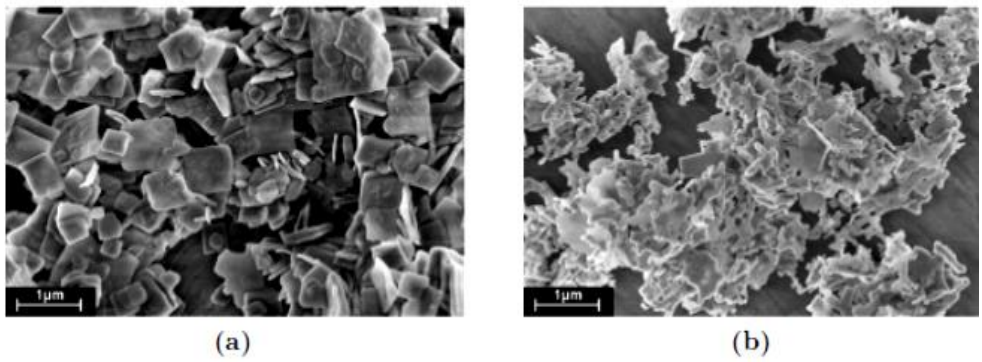

Figure B.1 | Squared platelets from autoclave acetate reaction (a) before and (b) after annealing where they sinter together and form clusters.

The XRD in Fig. B.2 shows patterns with two super imposed spectra. One is a complex pattern with a rich collection of peaks, none of which could be clearly ascribed either to Lu_2O_3 or to unreacted precursors and the second, being comparably weak, belongs to a cubic structure with very small crystallites.

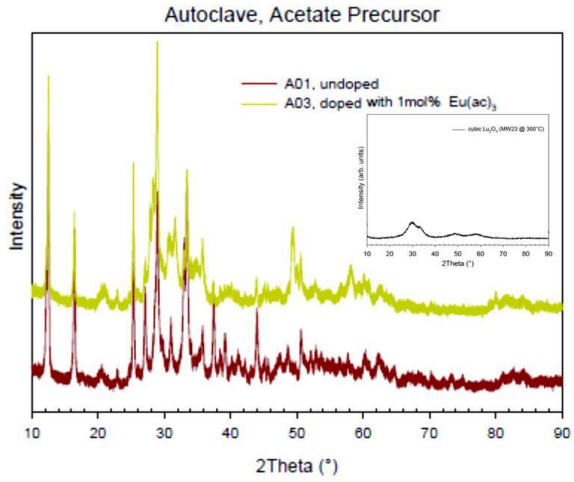

Figure B.2 | XRD of undoped and Eu doped NPs. In the inset, the XRD spectrum of a cubic Lu_2O_3 nanopowder is reported.

The evolution of the XRD pattern of NPs obtained by acetate reaction in Fig. B.3 shows that the unknown phase disappeared at 300 °C and that cubic Lu_2O_3 is formed below 400 °C. Further heating leads to crystallite growth. At 500 °C they are roughly 8nm in diameter and grow up to 46nm after the whole annealing procedure.

From these XRD results and the TEM image in Fig. B.1, it is clear that, by the Lu acetate precursor reaction in autoclave, it was not possible to obtain a powder with a pure Lu_2O_3 phase. Only after a heat treatment at 1200 °C in air, involving the decomposition of the organic fraction of the compound, pure lutetia was formed.

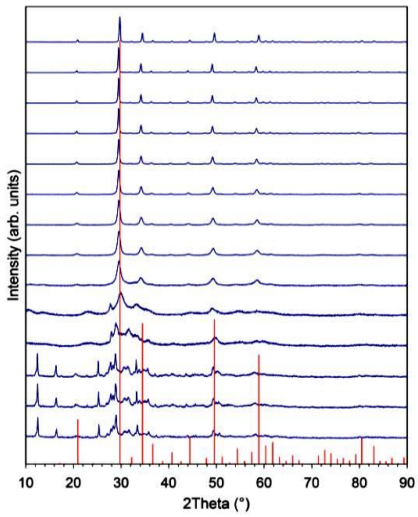

Figure B.3 | Evolution of the XRD pattern depending on the annealing temperature of Eu doped NPs obtained from Lu acetate precursor.

With the chloride precursor, extremely elongated platelets were formed with width and length ranges between 1 μm and up to 20 to 25 μm (Fig. B.4).

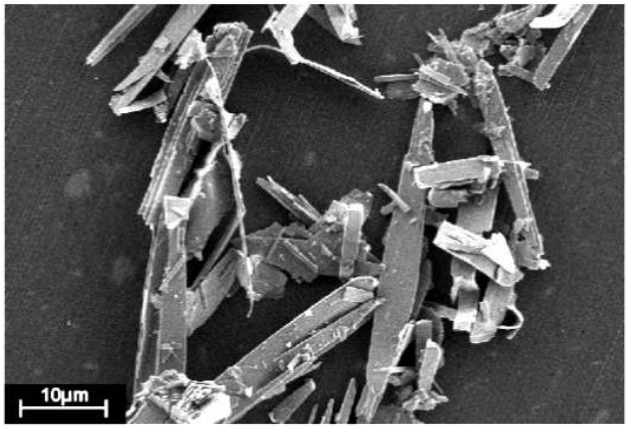

Figure B.4 | Blade-like shaped particles as a product of the solvothermal reaction of $LuCl_3$.

The XRD of the powder obtained directly after the reaction (Fig. B.5a) shows complex patterns which cannot be assigned to the precursor or doping with $Eu(ac)_3$. In the attempt to observe phase transformations of this unknown structure, thermal annealing in air has been performed (Fig. B.5b). The cubic Lu_2O_3 phase appears below 500 °C and grew upon further heating.

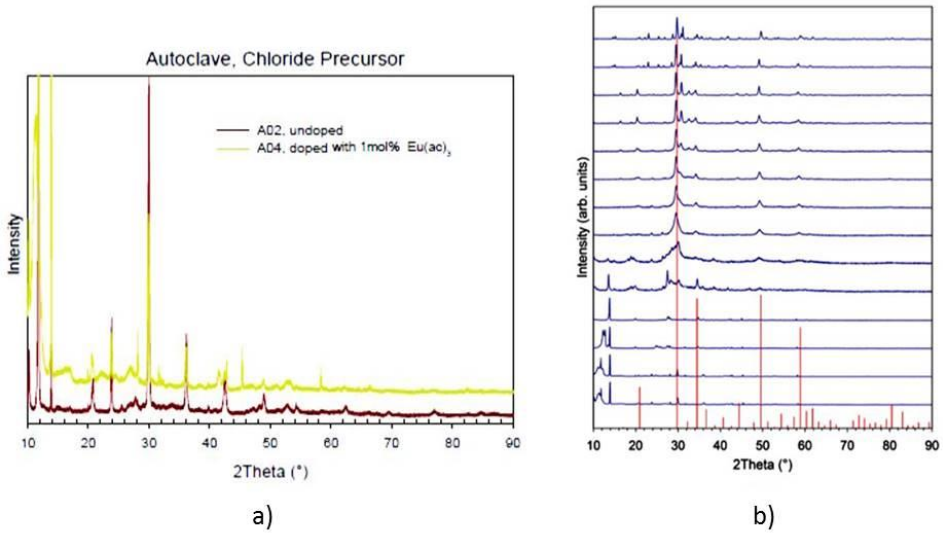

Figure B.5 |(a) XRD of undoped and Eu doped Lu_2O_3 NPs. (b) Evolution of the XRD pattern (normalized to the highest peak) depending on the annealing temperature of Eu doped lutetia NPs after reaction of Lu chloride in autoclave.

MICROWAVE SYNTHESIS

Using the $Lu(ac)_3$ precursor and a holding time of up to 10 min in the microwave synthesis, no particles were obtained. The XRD measurements (not shown), anyway, reveal the presence of an unidentified new compound, maybe resulting from a change of the precursor.

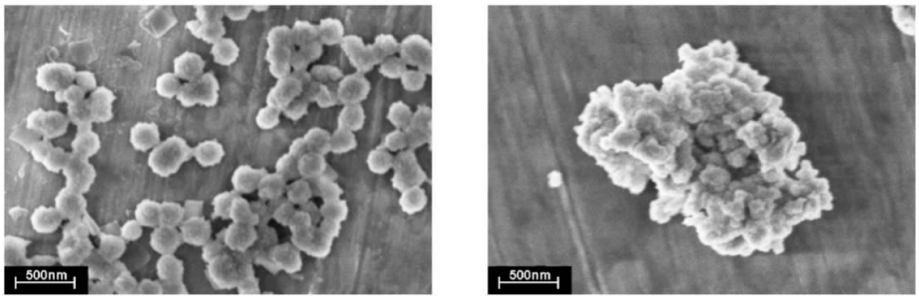

Figure B.6 | Reactions of 1 h (a) spherical particles of roughly 200 nm size. (b) Annealing at 1200 °C yields in highly crystalline cubic Lu_2O_3 clumps with an approximate crystallite diameter of 75 nm

By increasing the holding time of the microwave reactions up to 10 h, roughly 200 nm sized spherical particles together with a small fraction of squared platelets of comparable size were formed (Fig. B.6a). Interestingly, the XRD showed the presence of about 4 nm sized crystalline domains, most probably related to the spheres and of cubic nature. (Fig. B.7).

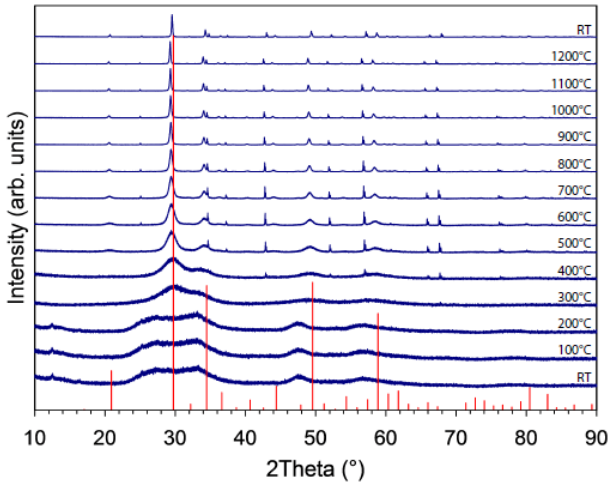

Figure B.7 | Long reaction times in the microwave for the $Lu(ac)_3$ precursor yield in a cubic phase which turns into Lu_2O_3 upon annealing.

By heating up the powder, the phases present after the reaction disappear above 200 °C and the cubic Lu_2O_3 phase is formed. Further heating leads to larger crystallites of about 75 nm at 1200 °C (Fig. B.7).

B.4. RADIOLUMINESCENCE

The radioluminescence spectra were recorded on pure and Eu doped powders. Additionally the heat treated powders at 500 °C and 1200 °C were also measured.

The RL emission band in the blue region (around 420 nm) in the doped and undoped samples is attributed to intrinsic emissions related to lattice defects. Together with intrinsic emission bands of minor intensity, the radioluminescence spectra of powders doped by Eu ions manifest its typical red emission (Fig. B.8). Actually, the occurrence of several emission lines in the red (570-720 nm) region of the spectrum, with a maximum located at *circa* 615 nm, corresponds to the radiative recombination on the $^5D_0$-^7F_J (J=0, 1, 2, 4) Eu transitions.

The material obtained from Lu chloride shows an additional and intense band at about 515 nm. This feature dominates the spectrum and could be possibly related to Eu recombination centers where the rare earth element is present in a different oxidation state, namely Eu^{2+}. The effect of heat treatment is displayed in Fig. B.9. The annealing in air at 500 °C leads to the disappearance of the green band at 515 nm in the chloride product. In addition, the intrinsic blue band decreases, as it may be related to intrinsic defects lying on the crystal surface, which increases with the annealing temperature.

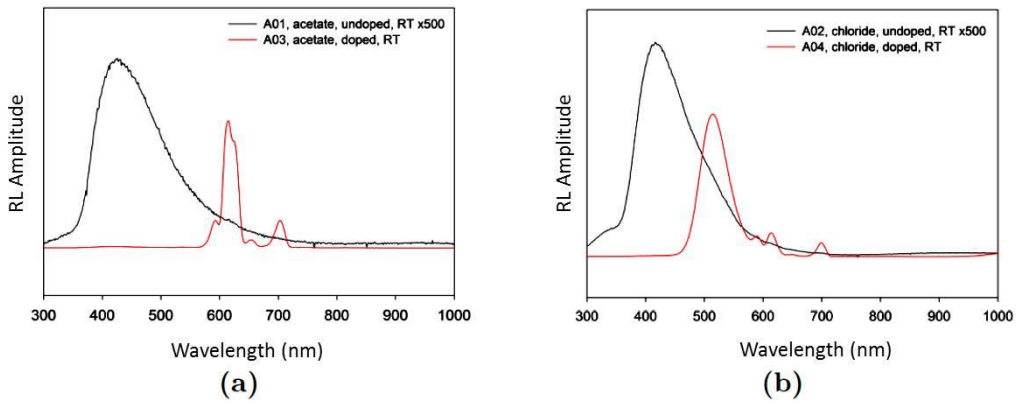

Figure B.8 | RL spectra of Eu-doped powders obtained using (a) acetate and (b) chloride precursors. The undoped sample is reported in black (magnified by factor of 500); the 1 mol% Eu-doped sample is plotted in red.

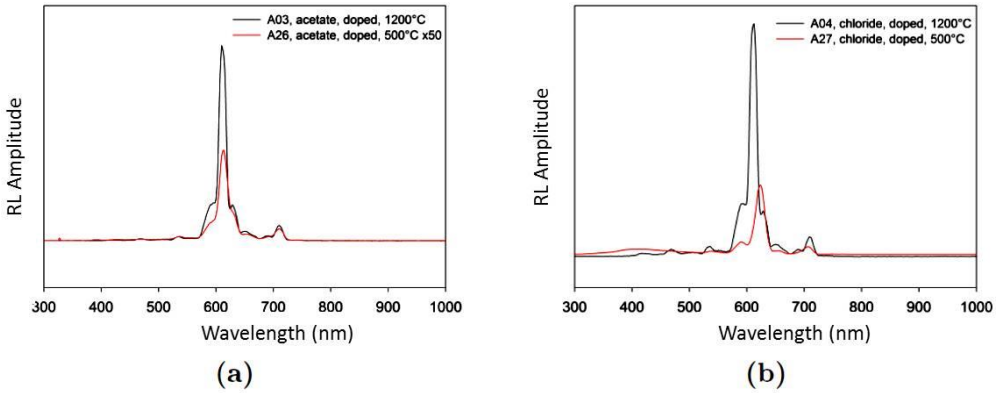

Figure B.9 | RL spectra for heat treated powders; (a) doped acetate and (b) doped chloride precursors. Red curve: powder heat treated at 500 °C; black curve: powder heat treated at 1200 °C.

Annealing at 1200 °C leads to complete removal of the organic phase, the increase of the crystal domains, as well as the formation of the cubic lutetia nanocrystals. Irrespective of the Lutetium precursor employed, the RL is dominated by the typical emission at 615 nm ascribed to the $^5D_0$ -$^7F_2$transition of Eu^{3+}sites.

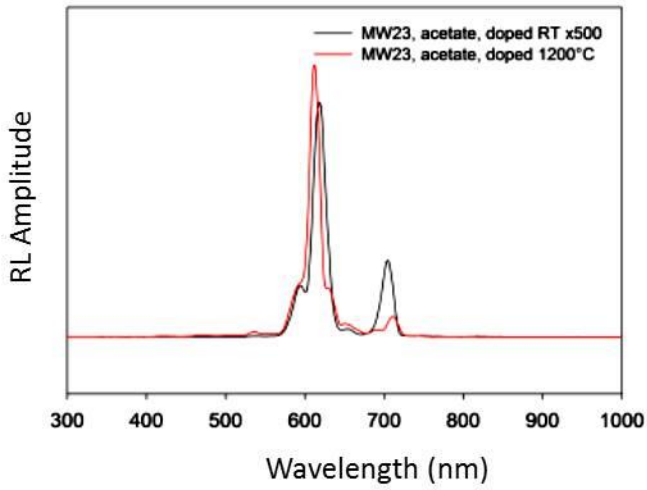

Figure B.10 | RL spectra for the microwave product as synthesized (black, magnified by a factor of 500) and heat treated at 1200 °C (red).

The microwave reaction of $Lu(ac)_3$ with benzyl alcohol leads to similar optical properties. Since f-f transitions of Eu^{3+} are very sensitive to crystal field, its emission features are a powerful tool for probing structural changes in the immediate surroundings of the rare earth site. Actually, the spectra are again dominated by the Eu hypersensitive transition at 615 nm, but a temperature induced change in the intensity ratio among the emission bands is evident in the longer wavelengths region.

Fig. B.11 shows the relative radioluminescence efficiency compared to that of bismuth germanate reference powder (BGO). Calcination increases the Eu light output roughly by a factor of 100. This could be ascribed to the reduction, during annealing, of non radiative decay channels, like point defects and intrinsic disorder associated with higher surface in smaller domains. In the case of the acetate precursor of lutetium, the total efficiency is 6 times higher

than that of BGO, a value that makes lutetia doped NPs very attractive as inorganic scintillator.

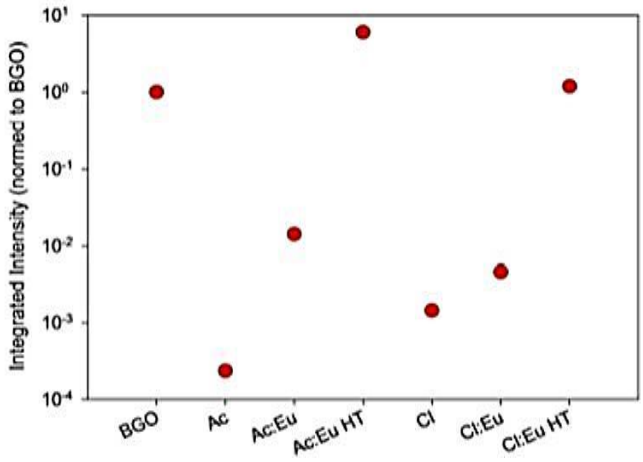

Figure B.11 | Comparison between the RL integrated intensities of Lu_2O_3 NPs and that of a BGO crystal considered as a standard.

B.5. REFERENCES

Li L. et al. (2010), *Photoluminescent properties of $Ln_2O_3:Eu^{3+}$ (Ln=Y, Lu and Gd) prepared by hydrothermal process and sol-gel method*. Materials Chemistry and Physics, 119, 3, pp. 471 – 477.

Shi Y. et al. (2009), *Processing and scintillation properties of Eu^{3+} doped Lu_2O_3 transparent ceramics.* Optical Materials, 31, 5, pp. 729–733).

Zych E. et al. (2002), *Spectroscopic properties of Lu_2O_3/Eu^{3+} nanocrystalline powders and sintered ceramics.* J. Phys. Chem. B, *106*, 15, pp 3805–3812).

APPENDIX C. CONFERENCES AND PUBLICATIONS

PUBLICATIONS

I. Villa, A. Vedda, M. Fasoli, R. Lorenzi, N. Kränzlin, F. Rechberger, G. Ilari, D. Primc, F. J. Heiligtag, M. Niederberger, A. Lauria, "Size-dependent Luminescence in HfO2 Nanocrystals for Rare-Earth-free White Light Emitting Phosphors", Submitted to Adv. Mat. DOI: 10.1002/

I. Villa, A. Vedda, I. X. Cantarelli, M. Pedroni, F. Piccinelli, M. Bettinelli, A. Speghini, M. Quintanilla, F. Vetrone, U. Rocha, C. Jacinto, E. Carrasco, F. Sanz-Rodríguez, Á. Juarranz, B. del Rosal, D. H. Ortgies, P. H. Gonzalez, José G. Solé, and D. Jaque, " 1.3 μm emitting $SrF2:Nd3^{+}$ nanoparticles for high contrast in vivo imaging in the second biological window", Nano-Research, DOI 10.1007/s12274-014-0549-1, 2014.

U. Rocha, K. Upendra Kumar, C. Jacinto, I. Villa, F. Sanz-Rodríguez, M. del Carmen Iglesias de la Cruz, A. Juarranz , E. Carrasco , F. C. J. M. van Veggel, E. Bovero, J.G. Solé , and D. Jaque, "Neodymium-Doped LaF3 Nanoparticles for Fluorescence Bioimaging in the Second Biological Window", Small 10, 6, 1141–1154, 2014.

A. Lauria, I. Villa, M. Fasoli, M. Niederberger and A. Vedda, "Multifunctional Role of Rare Earth Doping in Optical Materials: Nonaqueous Sol-Gel Synthesis of Stabilized cubic HfO2 Luminescent Nanoparticles", ACS Nano 7, 8, 7041, 2013.

ORAL CONTRIBUTIONS

I. Villa, A. Lauria, M. Fasoli, M. Niederberger and A. Vedda "Investigation of HfO2 nanoparticles intrinsic luminescence", EURODIM 2014, 12th Europhysical Conference on Defects in Insulating Materials (13th-19th July 2014, Canterbury, UK)

I. Villa, A. Lauria, M. Fasoli, F. Moretti, M. Niederberger and A. Vedda "Rare earth doped Hafnium-based nanocrystalline phosphors, achieved through a nonaqueous sol–gel process", LUMDETR 2012, 8th International Conference on Luminescent Detectors and Transformers of Ionizing Radiation (Halle (Saale), Germany, 10th/14th September 2012).

POSTER CONTRIBUTIONS

I. Villa ,P. Haro Gonzalez, U. Rocha, E. Carrasco, F. Sanz- Rodriguez, A. Juarranz de la Fuente, A. Speghini, M. Pedroni, I. X. Cantarelli, F. Piccinelli, M. Bettinelli, A. Vedda, D. Jaque García and J. García Solé "Novel Nd: SrF2 Nanoparticles for Autofluorescence Free Images in the II Biological Window", 17th International Conference on Luminescence and Optical Spectroscopy of Condensed Matter (13th-18th July, 2014 Wroclaw, Poland).

I. Villa ,P. Haro Gonzalez, U.Rocha, E. Carrasco, F. Sanz- Rodriguez, A. Juarranz de la Fuente, A. Speghini, M. Pedroni, I. X. Cantarelli, F. Piccinelli, M. Bettinelli, A. Vedda, D. Jaque García and J. García Solé "Novel SrF2:Nd3+ nanoparticles for fluorescence cancer imaging" Summer School on emerging renewable energy conversion and storage – PCAM 2013, (Como Lake, Italia, 9-13 September 2013).

A. Lauria, I. Villa, M. Fasoli, A. Vedda, and M. Niederberger "Non aqueous synthesis of cubic HfO2 nano-phopshors: structural modification thorough RE3+ incorporation". Fall Meeting of the Swiss Chemical Society 2013, Ecole Polytechnique Fédérale de Lausanne, (Lausanne, Switzerland, 6 September 2013).

A. Lauria, M. Imhof, I. Villa, M. Fasoli, A. Vedda, and M. Niederberger "Role of lutetium precursors in non-hydrolitic sol-gel synthesis of oxide nanoscintillators: Structure and optical response". XVII International Sol-Gel Conference, (Madrid, Spain, 25-30 August 2013).

I. Villa, A. Lauria, M. Fasoli, F. Moretti, M. Niederberger and A. Vedda "Rare earth doped Hafnium-based nanocrystalline phosphors, achieved through a nonaqueous sol–gel process" XIth International Krutyn Summer School: Cutting-Edge Luminescent Materials: Shifting the Frontiers, (Krutyn, Poland, 23- 29 September 2012).